UNIVERSITY OF CALIFORNIA

Los Angeles

Automated Quantitative Analysis of Cardiac Medical Images

A dissertation submitted in partial satisfaction

of the requirements for the degree

Doctor of Philosophy in Computer Science

by

Xiaowei Ding

2015

ABSTRACT OF THE DISSERTATION

Automated Quantitative Analysis of Cardiac Medical Images

by

Xiaowei Ding

Doctor of Philosophy in Computer Science

University of California, Los Angeles, 2015

Professor Demetri Terzopoulos, Chair

Clinical medicine often demands the quantitative analysis of medical images. This has traditionally been accomplished through the careful manual tracing and labeling of imaged anatomical structures, a methodology that is usually arduous, time-consuming, expensive, and fraught with low reproducibility. In the context of cardiac image analysis, this thesis develops novel methods for quantifying clinically important parameters from cardiac Computed Tomography (CT) and Magnetic Resonance (MR) imagery in a fully-automated manner; in particular, for automated Epicardial Fat Volume (EFV) quantification from non-contrast cardiac CT, automated Pericardial Fat Volume (PFV) quantification from waterfat-resolved whole-heart non-contrast coronary Magnetic Resonance Angiography (MRA), and automated Coronary Calcium Scoring (CCS) from non-contrast cardiac CT images. The key algorithmic components of our computational framework are atlas-based segmentation, graph-based segmentation, and active contours models. We validate our techniques using test scans with ground truth data quantified by expert radiologists, concluding that they may potentially be applied in a clinical setting to enable the accurate quantification of EFV, PFV, and CCS without tedious manual tracing.

The dissertation of Xiaowei Ding is approved.

Damini Dey

D. Stott Parker

Alan L. Yuille

Demetri Terzopoulos, Committee Chair

University of California, Los Angeles

2015

To my parents and grandparents.

TABLE OF CONTENTS

List of Figures

List of Tables

ACKNOWLEDGMENTS

First, I would like to thank my advisor, Professor Demetri Terzopoulos, deeply for his unconditional support and encouragement throughout my PhD life and this research. His generous assistance started before I joined his group and his mentorship will continue after I graduate. He has established a great example as a dedicated researcher with incomparable talent and insight in both the computer vision and computer graphics fields. I could never have achieved the work reported in this thesis without his inspiration and positive influence, or outside of the free research environment created by him.

I am very grateful to my external committee member, Professor Damini Dey of the UCLA David Geffen School of Medicine and Cedars-Sinai Medical Center. Professor Dey and Professor Piotr Slomka supervised my medical image analysis research projects and played a key role in helping with financial, equipment, data, and collaborative support. They both have a perfect blend of skills and experience in the clinical and technical fields, which makes them ideal supervisors for this work.

To Professors Alan Yuille and Stott Parker, I am very appreciative of their membership in my doctoral committee, and for their guidance on my research and thesis writing.

My special thanks go to my labmates Chenfanfu Jiang, Sharath Gopal, Jingyi Fang, Wenjia Huang, Weiguang Si, Lap-Fai Yu, Gautam Prasad, Kresimir Petrinec, Garett Ridge, Matthew Wang, Masaki Nakada, Diana Ford, Luis Angel Larios Cardenas, Noah Duncan, Gergely Klar, Eduardo Poyart, Tomer Weiss, Yuting Wang, Andre Pradhana, Alexey Stomakhin, and Daniel Ram in the UCLA Computer Graphics and Vision Laboratory, collaborators Yixin Zhu, Yibiao Zhao, Hang Qi, and Dan Xie from the UCLA Center for Vision, Cognition, Learning, and Autonomy, collaborator Zhou Ren from the UCLA Center for Cognition, Vision, and Learning, collaborator Qian Li from the UCLA Department of Biostatistics, and collaborator Ying Chen from the Department

of Aerospace and Mechanical Engineering at the University of Southern California (USC). I thank them for their help, which was always available, day and night.

The Biomedical Imaging Research Institute and Artificial Intelligence in Medicine (AIM) group at the Cedars-Sinai Medical Center have provided an amazing and inspiring environment for research and I have benefited substantially from working and collaborating with its many outstanding faculty and researchers. I thank Professor Debiao Li and Professor Daniel Berman for their encouragement and support. I have worked with several amazing researchers there and have co-authored multiple papers with Dr. Jianing Pang, Prof. Zhaoyang Fan, Dr. Mariana Diaz-Zamudio, Dr. Michaela Hell, and Dr. Mathieu Rubeaux.

Words cannot express my gratefulness to my mother, Xinyan Liu, and father, Zheng Ding, grandparents, Aiyun Hu and Yunpeng Ding, grandparents-in-law, Weizhen Luo and Qingzhong Liu, and other members of my family. My education and future career are always the first priority of our family. They have made every effort to provide strong support for me to pursue opportunities for better education. Without their unceasing love and sacrifice, I would not have gotten the chance to study at UCLA, let alone complete this thesis.

VITA

2012	B.S. in Electrical Engineering, Shanghai Jiao Tong University, Shanghai, China
2012-2013	Teaching Assistant, Computer Science Department, UCLA
2013-2015	Research Assistant, Biomedical Imaging Research Institute, Cedars-Sinai Medical Center, Los Angeles

PUBLICATIONS

Ding, X., Terzopoulos, D., Diaz-Zamudio, M., Berman, D. S., Slomka, P. J., Dey, D., (2015) "Automated pericardium delineation and epicardial fat volume quantification from noncontrast CT," *Medical Physics*, **42**(9), September, 5015–5026.

Ding, X., Pang, J., Ren, Z., Diaz-Zamudio, M., Berman, D., Li, D., Terzopoulos, D., Slomka, P., Dey, D., (2015) "Automated Pericardial Fat Quantification from Coronary Magnetic Resonance Angiography," in *Medical Image Understanding and Analysis*, pp. 80–85.

Ding, X., Slomka, P. J., Diaz-Zamudio, M., Germano, G., Berman, D. S., Terzopoulos, D., Dey, D., (2015) "Automated coronary artery calcium scoring from non-contrast CT using a patient-specific algorithm,"*SPIE Medical Imaging*, March, pp. 94132U–94132U.

Ding, X., Terzopoulos, D., Diaz-Zamudio, M., Berman, D. S., Slomka, P. J., Dey, D.,

(2014) “Automated Epicardial Fat Volume Quantification from Non-contrast CT,” *SPIE Medical Imaging*, 90340I–90340I.

Ding, X., Xu, Y., Deng, L., and Yang, X., (2012) “Colorization Using Quaternion Algebra with Automatic Scribble Generation,” *Proceedings of 18th International Conference on Multimedia Modeling*, Springer, Berlin, 103–114.

Dey, D., Alexanderson-Rosas, E., Schuhback A., Otaki, Y., Ding, X., Orozco, L., Meave-Gonzalez, A., Berman, D., Achenbach, S., Li, D., Slomka, P., (2013) “Quantitative Adverse Plaque Features from Coronary CT Angiography Predict Impaired Myocardial Flow Reserve by 13N-Ammonia-PET,” *Radiological Society of North America Scientific Assembly and Annual Meeting*, December, Chicago IL.

Ding, X., Terzopoulos, D., Diaz-Zamudio, M., Berman, D. S., Slomka, P. J., Dey, D., (2014) “Automated Pericardium Delineation and Epicardial Fat Volume Quantification from Non-contrast CT,” *Society of Cardiovascular CT Annual Scientific sessions*, July, San Diego, CA.

Hell, M., Ding, X., Slomka, P., Terzopoulos, D., Hayes, S., Achenbach, S., Berman, D., Dey, D., (2015) “Epicardial Adipose Tissue Volume but Not Density is an Independent Predictor for Myocardial Ischemia,” *European Society of Cardiology Congress*, August, London, UK.

CHAPTER 1

Introduction

The reliable quantitative analysis of medical images typically requires the delineation of anatomical structures. This is a difficult task, often performed by a human observer. Since manual image segmentation is time consuming, it is tedious to perform in very large number of scans; for example, scans obtained as part of preventive health care screening programs. Additionally, manual delineation may not be sufficiently reproducible. Algorithms supporting automated segmentation by computer are therefore needed.

Cardiovascular disease is the leading cause of death in developed countries and it is rapidly becoming the number one killer in the world. Epicardial fat volume, pericardial fat volume, and coronary calcium scores are found to be associated with cardiovascular disease. Epicardial fat is a particular depot of visceral fat around the heart, which is enclosed by the visceral pericardial sac [Dey et al., 2012]. Recent studies have shown a correlation between epicardial fat volume and various manifestations of coronary artery disease, including adverse cardiovascular events [Cheng et al., 2010; Mahabadi et al., 2009, 2013], myocardial ischemia [Tamarappoo et al., 2010; Janik et al., 2010], coronary artery stenosis [Hirata et al., 2011; Gorter et al., 2008], adverse plaque characteristics [Konishi et al., 2010; Alexopoulos et al., 2010; Rajani et al., 2013], metabolic syndrome [Dey et al., 2010c], and atrial fibrillation [Al Chekakie et al., 2010; Wong et al., 2011]. Recent studies also show that pericardial fat is strongly associated with Coronary Artery Disease (CAD), Coronary Calcium Scores (CCS), severity of detected

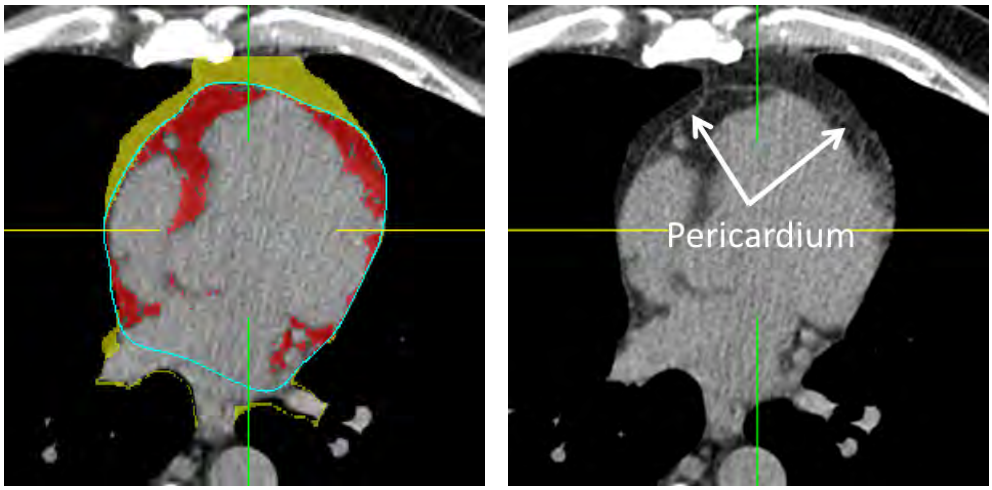

(a) (b)

Figure 1.1: *Epicardial fat (red), thoracic fat (red and yellow), and pericardium (blue line) in a non-contrast CT transverse slice (a). Arrows (b) indicate the pericardium in the original image.*

CAD, biochemical markers of systemic inflammation, risk of future adverse cardiovascular events, and myocardial ischemia [Dey et al., 2010a,c; Taguchi et al., 2001; Fox et al., 2007; Ding et al., 2008; Mahabadi et al., 2009; Sarin et al., 2008; Ding et al., 2014; Greif et al., 2009; Cheng et al., 2010].

Pericardial fat refers to the adipose tissue surrounding the heart enclosed by the rib-cage and above the diaphragm. As is illustrated in Figure 1.1(a), epicardial fat (red) is the part of the pericardial fat (red and yellow) enclosed by the pericardium, which is a tough double-layered membrane that covers the heart. Epicardial fat exists inside the pericardium and surrounds the coronary arteries directly. It is better correlated with coronary artery disease and thus has higher predictive value for cardiovascular risk stratification than the pericardial fat tissue outside the pericardium. The pericardial sac has two layers, the outermost fibrous pericardium and the inner serous pericardium. On non-contrast CT scans, the fibrous pericardium is identified as a thin curvilinear line of soft tissue density, well seen anterior to the right ventricle and in front of the right atrioventricular groove, where it is bordered by mediastinal and subepicardial fat of

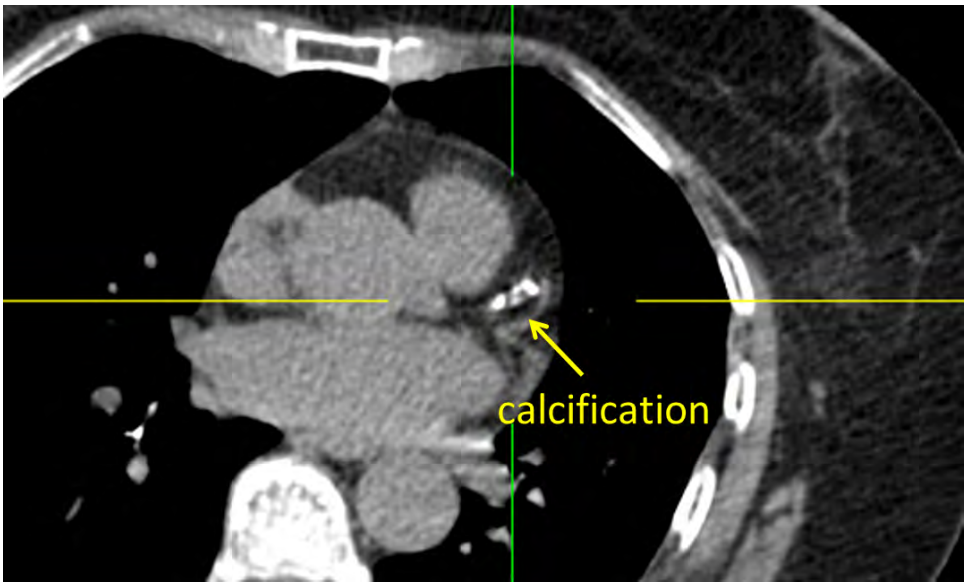

Figure 1.2: *Example image of coronary calcification in non-contrast CT*

negative densities (Figure 1.1(b)). It is less often visible lateral to the left ventricle and in front of the interventricular groove. The pericardium is often not fully visible in CT images, which makes the detection of the boundaries of epicardial fat difficult. Thus, the automated quantification of epicardial fat volume is particularly challenging since it requires identification of the pericardium in addition to the thoracic cavity and the heart.

Epicardial fat and pericardial fat are emerging as important factors for cardiovascular risk stratification. It would therefore be desirable to be able to accurately and non-invasively quantify them for a given patient in clinical practice. Epicardial fat and pericardial fat can be visualized in non-contrast cardiac CT performed for assessment of coronary calcium, which is a low-cost, non-invasive scan with a low radiation burden [Morin et al., 2003]. However, epicardial fat is not assessed in routine clinical practice from CT, primarily due to the absence of a robust, automated quantification algorithm. It is also desirable to be able to automatically quantify pericardial fat from MR imaging, which imposes no ionizing radiation on patients.

Coronary Artery Calcium (CAC) (Figure 1.2), a subclinical marker of coronary atheroscle-

Table 1.1: *Contributions of this thesis: This thesis reports the first work to fully automate epicardial fat quantification and regional calcium scoring from non-contrast cardiac CT and thoracic fat quantification from MR imaging.*

		Semi-Automated	Fully-Automated
CT	Thoracic Fat Volume	$\surd$	$\surd$
	Epicardial Fat Volume	$\surd$	$\times \rightarrow \surd$
	Total Calcium Score	$\surd$	$\surd \rightarrow \surd^{+}$
	Regional Calcium Score	$\surd$	$\times \rightarrow \surd$
MR	Thoracic Fat Volume	$\times$	$\times \rightarrow \surd$
	Epicardial Fat Volume	$\times$	$\times$

($^{+}$ We use anatomic definition instead of training a classifier)

rosis, can be visualized and quantified with non-contrast cardiac CT, and the amount of CAC is typically expressed in terms of a calcium score (Agatston score [Budoff et al., 2006], volume score [Callister et al., 1998]). Identifying individuals with obstructive disease could be improved by vessel-based rather than global quantification of calcium [Thilo et al., 2010].

1.1 Contributions

In this dissertation, we aim to develop and validate fully-automated algorithms for epicardial fat volume quantification from non-contrast CT, pericardial fat volume quantification from Magnetic Resonance Angiography (MRA), and both overall and regional measurement of coronary artery calcium scores from non-contrast CT.

In the manual quantification of epicardial and pericardial fat, image data is traced as follows: First, the upper slice limit, marked by bifurcation of the pulmonary trunk, and lower slice limit, identified as the last slice containing any portion of the heart, is manually chosen (Figure 1.3). Next, an experienced reader scrolls through the image slices between the upper and lower heart limit and if the pericardium is visualized, places 5 to 7 control points on the pericardium in transverse view (Figure 1.4). From

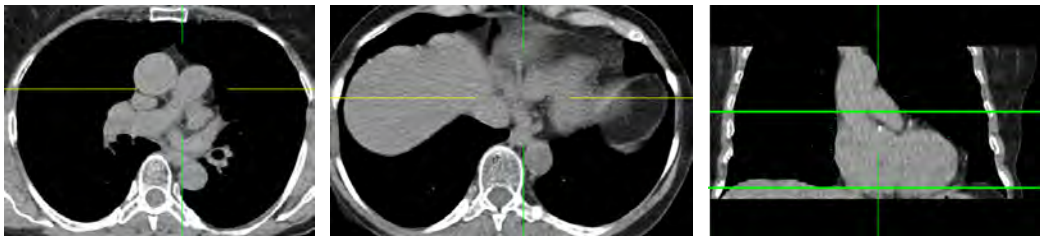

(a) (b) (c)

Figure 1.3: *Manual selection of superior and inferior heart limits (a) Superior slice: pulmonary artery split, (b) Inferior slice: posterior descending artery, (c) superior and inferior heart limits (green lines) from coronal view.*

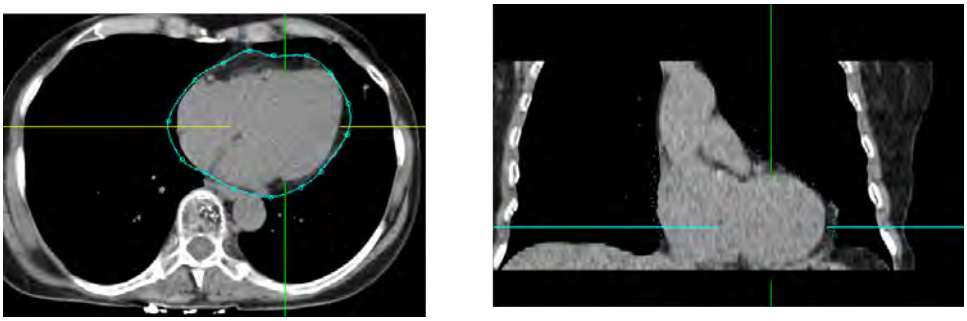

Figure 1.4: *Tracing the pericardium or heart boundary with 7 to 10 control point on each transverse image slice.*

the control points, piecewise spline functions are generated to obtain a smooth closed pericardial contour or heart region contour. Following the selection of cardiac limits and the placing of control points, contiguous 3D voxels between the Hounsfield Unit (HU) limits of (-190, -30) are defined as fat voxels in non-contrast CT images. Contiguous 3D voxels in the separated fat signals from MR imaging are defined as fat voxels. This procedure will take an experienced observer 10 to 60 minutes to trace on one patient, depending on the number of slices available for the patient.

The manual quantification of global and regional coronary artery calcium scores also includes tedious and time-consuming image labeling. For example, on commercial PACS (Picture Archiving and Communication System) software, the operator must go over all the slices of the patient and click on every calcified lesion to obtain the total coronary calcium score (Figure 1.5). To obtain the regional scores, the operator must label each

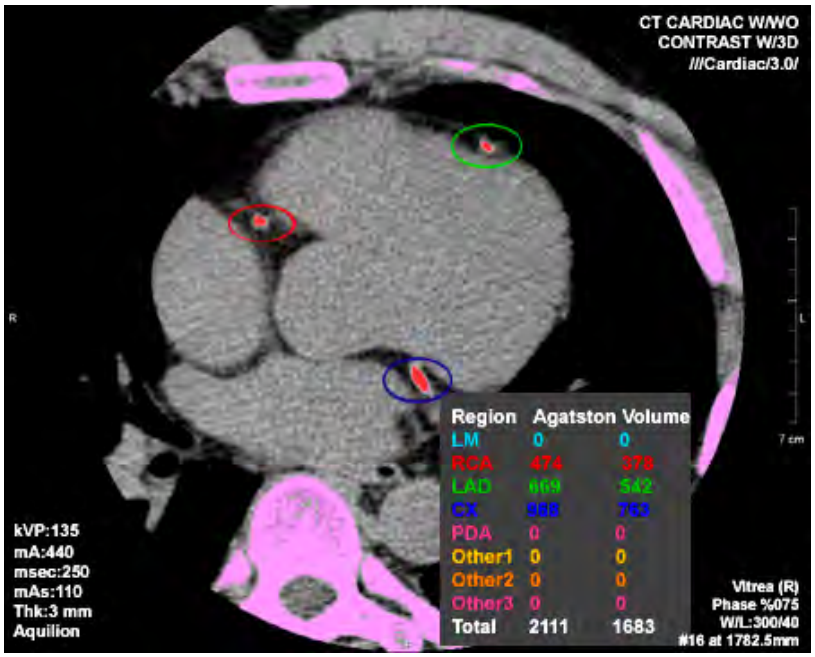

Figure 1.5: *Manual quantification of coronary calcification*

lesion with a proper category that represents one of the three coronary arteries.

The above manual process not only requires time and expensive human labor, but it also suffers from inter-observer and intra-observer variability. Thus, our fully-automated algorithms could save operating time and labor cost while increasing reproducibility, which is important in clinical practice and research.

Semi-automated quantification algorithms for these tasks are well developed nowadays. Although these methods can save radiologists much time, the still require human supervision and interaction, which hinders the overnight processing of large datasets. With the solutions reported in this thesis, fat and calcium quantification from both CT and MR images is now fully-automated for the first time. Table 1.1 shows the contributions of this thesis to the research field as well as to clinical application settings.

1.2 Dissertation Overview

The remainder of this dissertation is organized as follows:

Chapter 2 briefly reviews the image segmentation algorithms that are relevant to our research work: atlas-based segmentation algorithms, active contours algorithms, and graph-based segmentation algorithms. Previous works on related applications, such as cardiac fat volume quantification and coronary calcium scoring, are also introduced in this chapter.

Chapter 3 develops a new algorithm for epicardial fat volume quantification from non-contrast CT. This algorithm can detect and segment the fine details of anatomical structure; for example, a very thin membrane—the pericardium in the CT image—and accurately quantify the volume of epicardial fat in a fully-automated manner.

Chapter 4 describes the first algorithm for automated pericardial fat volume quantification from Magnetic Resonance (MR) imaging. Using a new type of high-resolution water/fat-separated MR imagery acquired at the Cedars-Sinai Medical Center, robust pericardial fat volume quantification can be achieved without exposing the patient to radiation.

Chapter 5 introduces an automated algorithm for a frequently performed task in daily clinical practice, coronary artery calcium scoring from non-contrast cardiac CT.

In Chapters 3, 4, and 5, the image data and algorithms described in the previous sections are experimentally evaluated and the results are compared to experts' manual annotations. We also discuss the differences between our algorithm and prior work.

Chapter 6 concludes the dissertation and proposes avenues for future work.

CHAPTER 2

Related Work

With the increased use of medical imaging, the medical image analysis research field has become preoccupied with the challenging problem of quantitative analysis, which is the extraction of clinically useful information about anatomic structures imaged through CT, MR, Ultrasound, PET, and other imaging modalities. Although modern imaging devices provide views of internal anatomy, the use of computers to quantify and analyze the biomarkers and embedded structures with accuracy and efficiency remains limited. Accurate, repeatable quantitative data must be efficiently extracted in order to support the spectrum of biomedical investigations and clinical activities from diagnosis, to radiotherapy, to surgery.

Segmenting anatomical structures in medical images and reconstructing a compact geometric representation of these structures is difficult due to the limited physical resolution of the datasets and the complexity and variability of the anatomic shapes of interest. Furthermore, the shortcomings of the reconstructed image data, such as sampling artifacts, spatial aliasing, and noise, may cause the boundaries of structures to be indistinct and disconnected. The challenge is to extract boundary elements belonging to the same structure and to integrate these elements into a coherent and consistent model of the structure. Traditional low-level image-processing techniques that consider only local features can make incorrect assumptions during this integration process and generate inaccurate object boundaries.

These model-free techniques must usually be augmented by model-based techniques

that introduce certain assumptions and restrictions in order to interpret the low-level detection results in terms of plausible physical objects. However, model-based techniques usually need a good initialization and, normally, high-level guidance.

The remainder of this chapter will review three types of segmentation techniques: atlas-based segmentation, active contours, and graph-based segmentation.

2.1 Atlas-Based Segmentation

The automated segmentation of cardiac images is a challenging task due to variations of the shape of the heart, body size among patients, and image artifacts. Due to the fact that different anatomical structures may share the same tissue contrast, prior anatomical information is essential in tackling the problem; for instance, as a set of predefined rules based on known tissue properties, or as a set of manual expert annotations. In this section, we focus on anatomical priors from an atlas that is matched to the target volume to segment. The atlas is composed of two image volumes—an intensity image and a segmented image.

The atlas-based segmentation problem can be solved by image registration. Volumetric registration is often done in two steps. Firstly, a global registration (affine or rigid transformation) is performed to obtain an initial alignment at a low computational cost. Secondly, a local non-rigid registration is applied to adapt general models to a specific anatomy. Note that this local registration provides a better match between different hearts at the expense of a high computational cost. Multi-resolution strategies may be used to reduce this computational cost [Rueckert et al., 1999].

Basic medical image registration methods have been reviewed in the literature [Maintz and Viergever, 1998; Lester and Arridge, 1999; Hill et al., 2001; Pluim et al., 2003]. These studies include reviews of registration techniques that can be used to align an

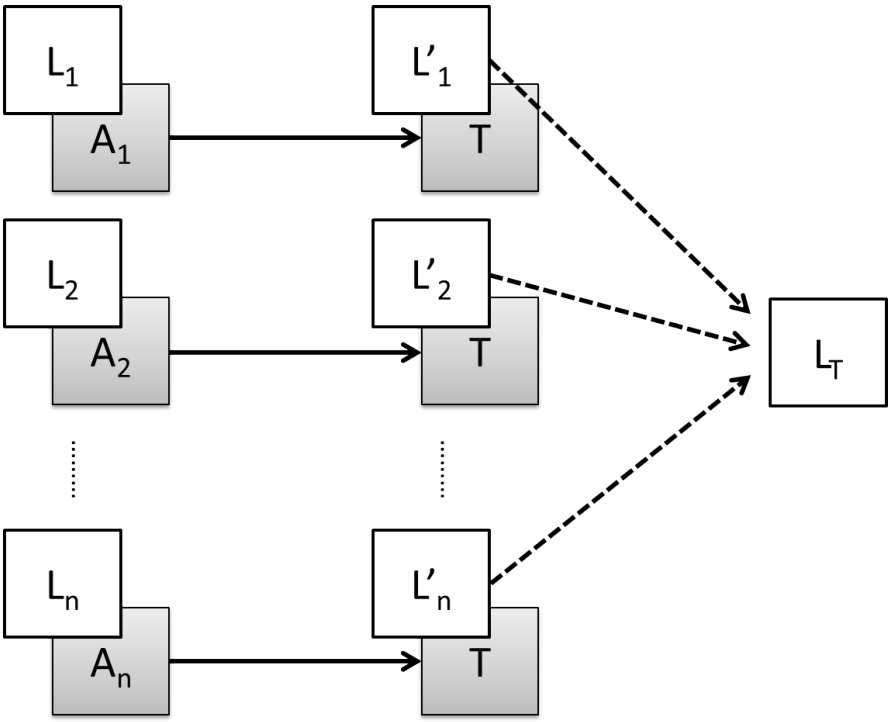

Figure 2.1: *Schematic illustration of multi-atlas segmentation. A set of atlas anatomical images A_i are registered to the target image T. The resulting transformation is used to transfer the corresponding atlas segmentations L_i to the target. The transformed segmentations L_i' are then combined to create an estimate of the target segmentation L_T.*

atlas to an unseen image. There are three different ways of integrating the atlas information into the whole segmentation process after the images are aligned—label propagation, multi-atlas propagation, and probabilistic atlas-based segmentation.

The fastest and most straightforward way to assign a label to each test image voxel is to propagate the atlas labels to the test image space. With this strategy, the segmentation process relies on an accurate registration process whose goal is to estimate the anatomical differences between the atlas and the input image volumes. Registration errors exist in all real-world applications, but the errors are larger if the differences between two images are large. We assume that the atlas is close to the subject's anatomy. Otherwise, in cases where large anatomical differences exist, large registration errors may cause significant segmentation errors.

Global rigid and affine transformations are usually enough when dealing with intra-subject medical applications, such as longitudinal studies of illness progression or multi-modality registration for radiotherapy planning. However, when dealing with inter-subject applications such as atlas matching, the anatomical variation between different subjects can only be captured using non-rigid registration algorithms.

Volume partitioning can be performed to account for local deformations. In general, either the moving image (usually the atlas), or the target image, or both image volumes are decomposed on smaller sub-volumes and these sub-volumes are then registered in a hierarchical manner using rigid and affine transformations [Hellier and Barillot, 2004; Andronache et al., 2008].

Other partitioning approaches define a uniform grid, usually called the free-form deformation grid, and then apply a non-linear transform to each of the grid vertices. Depending on accuracy and time efficiency requirements, grid vertices can be defined as the voxels for the whole volume. Common non-linear transforms based on mathematical transformations are, for instance, cosine-based functions [Ashburner et al., 1999], B-

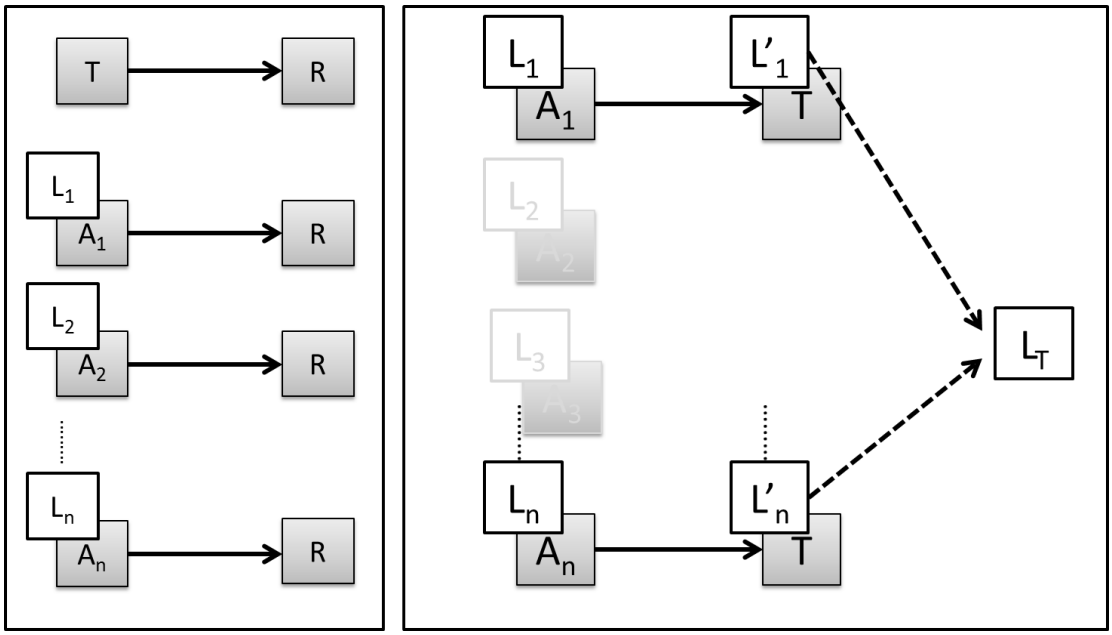

Figure 2.2: *Multi-atlas segmentation with image similarity selection. Left: All the atlas anatomies A_i and the target image T are registered to the reference image R. Similarities between the spatially normalized target and each of the atlases are used to generate ranks. Right: top-ranked atlases are selected and registered directly to the target image. The selected atlas segmentations L_i are propagated to the query, giving the segmentations L_i' which are fused to generate the native space segmentation estimate L_T for the target image.*

spline curves [Rueckert et al., 1999; Noblet et al., 2005], or level set partial differential equations [Vemuri et al., 2000]. Other functions that have been used to define displacement fields are based on the thermodynamics concept of demons [Thirion, 1998; Vercauteren et al., 2009], optical flow models [Vemuri et al., 1998; Postelnicu et al., 2009], or elasticity properties [Bajcsy et al., 1983; Gee et al., 1993].

Label propagation has been extended to multiple atlases to better deal with the registration errors obtained when using a single atlas and also to better account for anatomical variability (Figure 2.1).

With an atlas database, which usually includes images from patients with different organ shapes, BMI (Body-Mass Index), and gender, those voxels with low agreement between different label propagations can be discarded in order to minimize outliers. Due

to its strengths over simple label propagation, this technique presents an improvement in accuracy when dealing with the segmentation of objects with well-defined shape that may present slight deformations between images (Figure 2.2).

There are two important considerations to take into account when dealing with a set of atlases. The first is related to the number of atlases to be used to segment a new patient and how to select them. We refer to this issue as the selection criteria problem. Different studies [Klein et al., 2005; Wu et al., 2007; Aljabar et al., 2009; Lötjönen et al., 2010] conclude that using more than one topological atlas improves accuracy, but that it is not necessary to use all the cases in a database.

Two principal methods exist for choosing the best matching cases—either using meta-information (which may not always be available), or using similarity metrics to compare the images. The first method uses text information recorded by the physicians, such as patient age, gender, weight, height, shape characteristics of the organ, and description of the disease, to match similar patients in the atlas in order to achieve atlas selection. However, this is not an image-level comparison of the patient and cannot guarantee a best subset of atlas images to be selected. In order to use this second method, the new image must be aligned to all the manually-segmented cases. One possible technique is to warp all atlases into a common space, and the subject to be segmented will then be matched in this space. This considerably reduces the number of registrations. However, with this strategy, there exists a strong dependency on the initially selected reference space. Therefore, new groupwise registration techniques [Guimond et al., 2000; Joshi et al., 2004; Bhatia et al., 2004; Lorenzen et al., 2005; Park et al., 2005; Zöllei et al., 2005; Commowick and Malandain, 2006] may prove a better way of solving this issue. These techniques try to register all the subjects together constructing an average reference template at each step. It is also advisable to use a combination of similarity metrics to avoid bias from using the same metric as in the registration step. The question of how atlases should be combined remains. Voting

rules are commonly applied [Klein et al., 2005; Wu et al., 2007; Aljabar et al., 2009; Lötjönen et al., 2010; Heckemann et al., 2006; Artaechevarria et al., 2009].

When probabilistic atlases are used, voxel probabilities can be integrated as part of a statistical Bayesian framework; either parametric (for instance using Gaussian mixture models) or non-parametric approaches (for instance using Parzen windows) can be used to estimate the conditional probability of the intensities and the data energy term. Initial estimates of such models often use propagation of the atlas probabilities [Awate et al., 2006; Bricq et al., 2008a,b; Marroquín et al., 2002]. Class priors and smoothness term may also be encoded using atlas probabilities [Souplet et al., 2008], sometimes in combination with other spatial priors [Shiee et al., 2010; Bazin and Pham, 2008; Han and Fischl, 2007; Van Leemput et al., 1999, 2001; Fischl et al., 2002; Van der Lijn et al., 2008; Shiee et al., 2008b,a] often modeled by Markov Random Models.

Some other methods [Ciofolo and Barillot, 2009; Kamber et al., 1995; Zijdenbos et al., 2002; Kroon et al., 2008; Akselrod-Ballin et al., 2009] directly combine atlas probabilities with other image features such as voxel intensities or spatial coordinates to train a classifier. These classifiers allow several features to be combined without the need to estimate a probability distribution in a high dimensional space.

The above-mentioned strategies use all the atlas probability values after registering the atlas with the patient. In order to reduce the effect of registration errors, some approaches select only a subset of voxel samples with high probability per class. These atlas samples can then be used to train a classifier [Cocosco et al., 2003; Vrooman et al., 2007; de Boer et al., 2009; Tomas and Warfield, 2009], to estimate class distributions [Prastawa et al., 2004; Prastawa and Gerig, 2008], or as initialization points for a contour-based segmentation [Grau et al., 2004].

2.2 Active Contours

A major breakthrough to the curve propagation approaches, the Active Contour or "Snakes" model, was made in 1987 by Kass, Witkin, and Terzopoulos [Kass et al., 1988]. In the active contour model an elastic contour, representing internal smoothness (regularization) constraints, is propagated by image forces towards a minimal energy state. Inspired by the original model, variations included the balloon model [Terzopoulos et al., 1988; Cohen, 1991; McInerney and Terzopoulos, 1995], Deformable Template Models [Yuille et al., 1992; Lipson et al., 1990; Cipolla and Blake, 1990; Curwen and Blake, 1993; Pentland, 1990; Staib and Duncan, 1989], and the Geodesic Active Contour model [Caselles et al., 1997; Kichenassamy et al., 1995; Malladi et al., 1995] that successfully incoprorated level set theory, resulting in a very useful tool. This model is employed in our approach.

2.2.1 Energy-Based Active Contours

The classical energy-based active contour model was initially proposed in [Kass et al., 1988] and it was successfully applied to a wide variety of computer vision applications.

The deformable model is matched to an image by means of energy minimization, and it therefore exhibits dynamic behavior. Let $[C : [0,1] \rightarrow \mathcal{R}^2, p \rightarrow C(p)]$ be a parametrized close planar contour and let $I : Z^+ * Z^+ \rightarrow \mathcal{R}^+$ be a given image, where we would like to detect object boundaries. The active contour model minimizes the following energy:

$$E[(C)(p)] = \alpha \int_0^1 E_{int}(C(p))\,\mathrm{d}p + \beta \int_0^1 E_{img}(C(p))\,\mathrm{d}p + \gamma \int_0^1 E_{con}(C(p))\,\mathrm{d}p, \tag{2.1}$$

where the internal contour term $[E_{int}]$ constrains the contour to be regular and smooth, the image term $[E_{img}]$ attracts the contour to the desired features, and the term $[E_{con}]$

constrains the solution space. The general form the energy terms is as follows:

- The *internal* energy term

$$[E_{int}(C(p))] = w_{ten}(C(p))\left|\frac{\partial C}{\partial p}\right|^2 + w_{stif}(C(p))\left|\frac{\partial^2 C}{\partial p^2}\right|^2 \tag{2.2}$$

  imposes contour regularity, where the first order term makes the contour act like an elastic band (*i.e.* resist stretching), while the second term makes it act like a thin beam (*i.e.* resist bending).

- The *image* energy term

$$[E_{img}(C(p))] = w_l E_l(C(p)) + w_e E_e(C(p)) + w_t E_t(C(p)), \tag{2.3}$$

  is derived from the observed data, where the active contour may be attracted to *lines*, *edges* or *terminations*, with w_l, w_e, and w_t being the respective weights. In most cases, the *line* and *edge* terms are given by

$$E_l(C(p)) = I(C(p)); \quad E_e(C(p)) = |\nabla I(C(p))|^2 \tag{2.4}$$

  so that if w_l is positive, then the active contour is attracted to dark lines and if negative then it is attracted to bright lines. The *edge* term attracts the active contour to large image gradients (usually w_e is negative). Finally, the *termination* term allows terminations (*i.e.* free ends of lines) or corners to attract the active contour.

- Finally, the *external* energy term is derived by some user-defined constraints.

Once an appropriate initialization of the contour is specified, the active contour can quickly converge to the nearest local energy minimum using a variational approach.

Numerous variants have been proposed in the literature to improve the robustness and

stability of the original active contour model. In [Cohen, 1991], a "ballon force" was incorporated. The new term is an anisotropic pressure potential that controls the evolution of the area enclosed by the model and can either inflate or deflate the contour. A significant advancement was the use of finite elements-based Deformable Template Models to incorporate prior model information, which can either be very general, such as regularity constraints, or very specific, such as an exact template [Cipolla and Blake, 1990; Curwen and Blake, 1993; Pentland, 1990; Staib and Duncan, 1989].

The active contour model provides a powerful interactive tool to deal with computer vision problems. However, this approach is "myopic" because of the use of strictly local information and is very sensitive to the initialization step; if a model is initialized too far away from the target it may fail to locate the appropriate energy minimum. Additionally, this model is dependent on the parametrization of the contour. Moreover, due to the fact that is usually implemented using the Lagrangian approach, it cannot deal naturally with changes of topology. Finally the last problem of the active contour energy relies on the selection of the parameters that determines the contributions of the different energy terms.

2.2.2 Geodesic Active Contours

The geodesic active contour model [Caselles et al., 1997; Kichenassamy et al., 1995] was introduced as a geometric alternative for active contours. It can be viewed as an "extension" of classic active contours since it overcomes some of their limitations, especially by introducing topological flexibility. A similar geometry-based model was proposed in [Malladi et al., 1995].

This model does not impose any rigidity constraints $[w_{stif} = 0]$ and is given by

$$E[(C)(p)] = \underbrace{\int_0^L g(|\nabla I(C(s))|)\,\mathrm{d}s}_{\text{Geodesic Active Contour}} \tag{2.5}$$

$$= \int_0^1 \underbrace{g(|\nabla I(C(p))|)}_{\text{attraction term}} \underbrace{\left|\frac{\partial C}{\partial p}(p)\right|}_{\text{regularity term}} \mathrm{d}p, \tag{2.6}$$

where

$$g\ :\ [0,+\infty] \to \mathcal{R}^+; \quad g(0) = 1; \quad g(x) \to 0 \ \text{ as } x \to \infty \tag{2.7}$$

is a monotonically decreasing function. Here, $\mathrm{d}s$ is the Euclidean arc-length element and L the Euclidean length of $C(p)$. In other words, to detect an object we find the minimal-length geodesic contour that best takes into account the desired image characteristics.

Velocity applied to the points on the contour in the normal direction can cause deformation of the contour, however any velocity in the tangential direction will not change the shape of the contour. A contour evolves under mean curvature flow if the normal component of the velocity with which a point on the contour moves is proportional to the curvature of the contour:

$$C_t = \mathcal{K}\mathcal{N} \tag{2.8}$$

A contour of any shape evolving under mean curvature flow will first become convex, increasing in smoothness until it becomes a circle and finally shrinks down to a point (Figure 2.3).

The objective function is minimized using a gradient descent method. Therefore, the initial contour $C_0(.)$ is deformed towards a (local/global) minimum of $E[(C)(p)]$ (Fig-

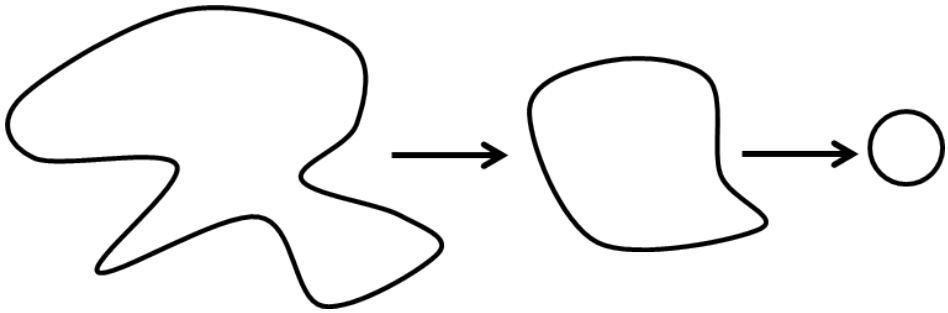

Figure 2.3: *Contour evolution under curvature flow*

ure 2.4) according to

$$C_t = \underbrace{g(|\nabla I|)\mathcal{K}\mathcal{N}}_{\text{boundary force}} - \underbrace{\nabla g(|\nabla I|) \cdot \mathcal{N})\mathcal{N}}_{\text{refinement force}}, \tag{2.9}$$

where t denotes time as the contour evolves, $\mathcal{N}$ is the inward Euclidean normal, and $\mathcal{K}$ is the Euclidean curvature. The above motion equation has a simple interpretation—each point of the contour should move along the normal direction in order to decrease the weighted length of C. There are two forces acting on the contour, both in the direction of the inward normal:

1. The first force moves the contour towards the object boundaries constrained by the curvature effect that ensures regularity during the propagation.

2. The second force is applicable only around the object boundaries $[\nabla g(|\nabla I|) \neq 0]$ and has a twofold role: (i) it is used to attract the contour to the boundaries and to overcome along them the propagation constraints imposed by the curvature effect, and (ii) it is used as a refinement term that centralizes the contour to the object boundaries.

The geodesic active contour model compares favorably with the classical active contour due to the fact that it does not depend on the contour parametrization and is relatively unconstrained by its initial conditions. However, this model evolves the contour according to the boundary attraction term in one direction (inwards or outwards). Thus,

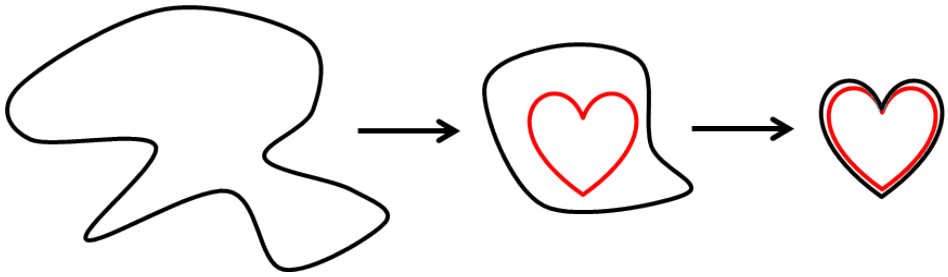

Figure 2.4: *Contour deforms towards a (local/global) minimum*

its proper usage demands a *specific* initialization step, where the initial contour should be completely outside or inside the object boundaries.

Many efforts have been made to overcome these shortcomings by introducing some region-based features that free the model from the initial conditions and increase its robustness [Chan and Vese, 1999; Paragios and Deriche, 1999; Yezzi Jr et al., 1999; Zhu and Yuille, 1996], although these approaches still suffer from the one-directional flow imposed by the boundary term.

2.2.3 Gradient Vector Flow Active Contours

The Gradient Vector Flow (GVF) framework [Xu and Prince, 1998a] refers to the definition of a bi-directional external force field that captures the object boundaries from either sides and can deal with concave regions. This flow can be considered as an alternative that compares favorably to the distance transform. Instead of using a binary edge for this transformation, the GVF is estimated directly from the continuous gradient space. Furthermore, the diffusion process that computes the GVF leads to a measurement that is contextual and not equivalent with the distance from the closest point. This is due to the fact that more that one "boundary" pixels (with different/opposite flows) contribute to the estimation of the GVF.

The first step within this framework is to determine a continuous edge-based information space, which in our case is provided by a Gaussian edge detector (zero mean, with

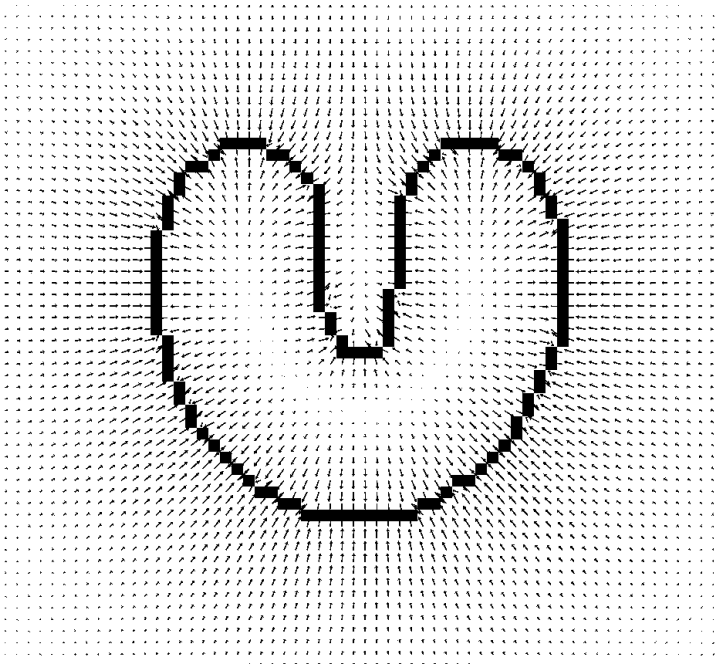

Figure 2.5: *Gradient Vector Flow (GVF) field for a U-shaped object [Xu and Prince, 1998b]. These vectors will pull an active contour towards the object boundary.*

σ_E variance)

$$g(p) = \frac{1}{2\pi\sqrt{\sigma_E}} e^{-\frac{|\nabla(G_\sigma * I)(p)|^2}{2\sigma_E^2}}, \quad f(x,y) = 1 - g(p), \tag{2.10}$$

where $G_\sigma * I$ denotes the convolution of the input image with a Gaussian (smoothing) kernel.

The gradient vector flow [Xu and Prince, 1998a] consists of a two-dimensional vector field $[v(p) = (u(p), v(p)), p = (x, y)]$ that minimizes the energy

$$E(v) = \iint \mu(u_x^2 + u_y^2 + v_x^2 + v_y^2) + |\nabla f|^2 |v - \nabla f|^2 \, \mathrm{d}x \, \mathrm{d}y, \tag{2.11}$$

where μ is a blending parameter. According to this objective function, areas where the image is near constant ($|\nabla f| \approx 0$) are dominated by the partial derivatives of the vector field, resulting on a smooth flow map. On the other hand, where there are significant variations ($|\nabla f| \gg 0$), the term that dominates the energy is the second one, leading

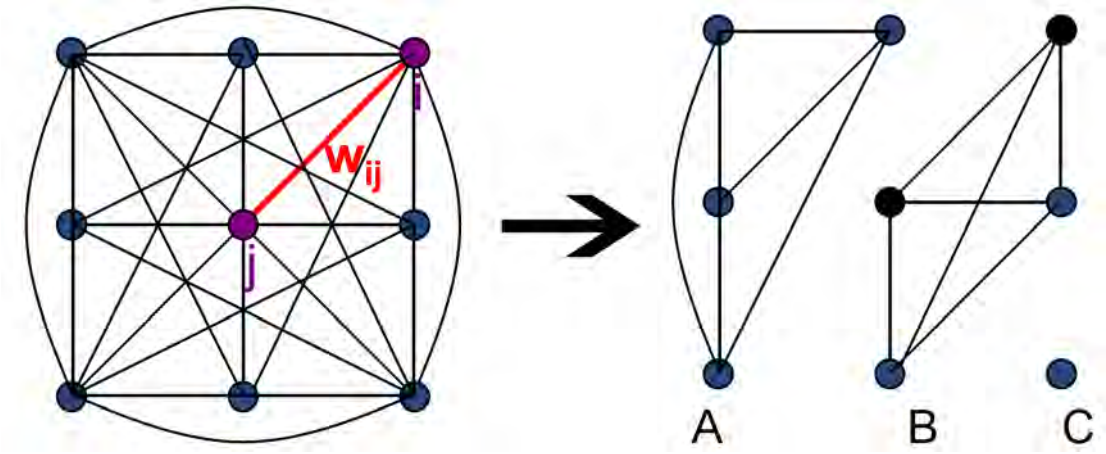

Figure 2.6: *Graph construction on an image and the graph cut into sub-graphs.*

to $v = \nabla f$. A more detailed interpretation of this energy can be found in [Xu and Prince, 1998a], which is similar with the one proposed by *Horn and Schunk* [Horn and Schunck, 1981] for the estimation of optical flow.

2.3 Graph-Based Segmentation

In this section, we review a segmentation approach based on finding minimum cuts in a graph, where the cut criterion is designed in order to minimize the similarity between pixels that are being split. The basic idea of graph-based image segmentation is to convert the image into a graph with vertices for the pixels/voxels, edges between the pixels/voxels, and additional vertices and edges to encode other constraints. A graph can be constructed on 2D, 3D, and ND images with a similar approach, which provides a uniform framework for processing 2D images, videos, static volumetric images, or dynamic volumetric images. The graph is then manipulated to segment the image according to a certain graph cut criterion (Figure 2.6).

Work by [Wu and Leahy, 1993] introduced such a cut criterion, but it was biased toward finding small components. This bias was addressed with the *normalized cut* criterion developed by [Shi and Malik, 2000], which takes into account the self-similarity of

regions. These cut-based approaches to segmentation capture non-local properties of the image, in contrast with the early graph-based methods. However, they provide only a characterization of each cut rather than of the final segmentation.

The normalized cut criterion provides a significant advance over the previous work in [Wu and Leahy, 1993], both from a theoretical and practical point of view (the resulting segmentations capture intuitively salient parts of an image). However, the normalized cut criterion also yields an NP-hard computational problem. While Shi and Malik developed approximation methods for computing the minimum normalized cut, the error in these approximations is not well understood. In practice these approximations are still fairly hard to compute, limiting the method to relatively small images or requiring computation times of several minutes. Subsequently, [Weiss, 1999] showed how the eigenvector-based approximations developed by Shi and Malik relate to more standard spectral partitioning methods on graphs. Such methods have a generic framework which can be used with many different features and affinity formulations and can provide regular segments. However, a user must specify the number of segments, which is costly in storage and computation and biases the partitioning towards equal segments. In many cases these methods are used for over-segmentation before regular segmentation.

[Boykov and Jolly, 2001] proposed an interactive graph cuts algorithm for optimal boundary and region segmentation of objects in images in any number of dimensions. The algorithm segments the foreground and background of the image by separating source and sink nodes using min cut (Figure 2.7). As a special case, application of this algorithm on 3-D volumetric medical image was introduced and validated in [Boykov and Jolly, 2000].

An alternative to the graph cut approach is to look for cycles in a graph embedded in the image plane. For example in [Jermyn and Ishikawa, 2001] the quality of each cycle is normalized in a way that is closely related to the normalized cuts approach.

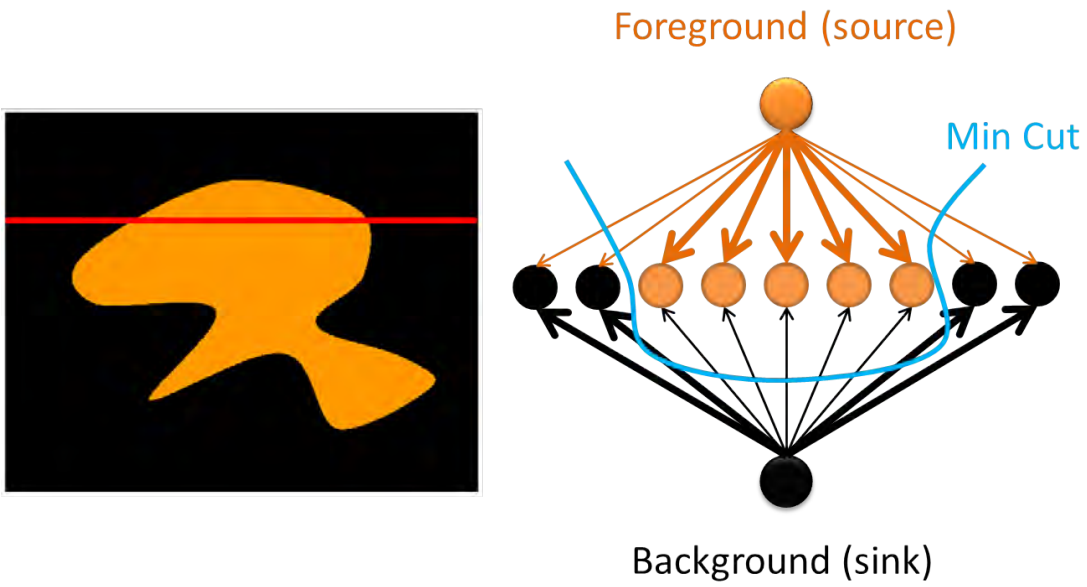

Figure 2.7: *Graph cut by separating source and sink*

2.4 Cardiac Fat Volume Quantification

Several investigators have reported methods for the quantification of only thoracic fat, but not for the epicardial fat. Dey et al. [2008] investigated semi-automated thoracic fat quantification from non-contrast CT. In this work, the lungs were first segmented by anterior sampling and adaptive threshold region-growing, followed by delineation of the inner contours of the thoracic cavity and determination of the cardiac bounding box. Yalamanchili et al. [2010] described a thoracic fat quantification algorithm that used a classification-based method to discriminate fat from other tissues. The classifier was constructed from three binary support vector machines classifiers trained separately for multiple tissues (fat, muscle/blood, and calcium), which achieved an average overlap of 78% with expert annotations. Isgum et al. [2009] have recently presented a multi-atlas-based automated method for segmenting the heart, but not the pericardium for the purposes of coronary calcium quantification.

In several recent studies of epicardial fat, the pericardium has been traced manually by

expert readers, which is time-consuming, requiring 7-10 minutes per patient [Dey et al., 2012; Cheng et al., 2010; Mahabadi et al., 2009, 2013; Tamarappoo et al., 2010; Janik et al., 2010].

2.5 Coronary Calcium Scoring

Some previously published studies on semi automated or fully automated calcium scoring algorithms are introduced in this section. Saur et al. [2008] and Shahzad et al. [2010] detected calcium in non-contrast CT in coronary arteries whose location was obtained by performing segmentation on contrast-enhanced scans. Isgum et al. [2007] detected coronary calcifications from non-contrast CT. The position of a potential coronary calcification was determined relative to the aortic and cardiac locations. Isgum et al. [2012] also published another classification approach for coronary calcium scoring in low-dose chest CT. Kurkure et al. [2010] detected coronary calcifications with a classification system employing a heart-centered coordinate system, which was used to extract spatial features. Brunner et al. [2010] detected zones of the coronary arteries using the coordinate system described in [Kurkure et al., 2010]. Regional calcium scores were calculated using an equidistant division of the coronary artery zones.

CHAPTER 3

Automated Epicardial Fat Volume Quantification From Non-Contrast CT

In this chapter, we develop and validate an automated algorithm for Epicardial Fat Volume (EFV) quantification from non-contrast CT. We develop a hybrid algorithm based on initial segmentation with a multiple-patient CT atlas, followed by automated pericardium delineation using geodesic active contours. A co-registered segmented CT atlas is created from manually segmented CT data and stored offline. The heart and pericardium in test CT data are first initialized by image registration to the CT atlas. The pericardium is then detected by a knowledge-based algorithm, which extracts only the membrane representing the pericardium. From its initial atlas position, the pericardium is modeled by geodesic active contours, which iteratively deform and lock onto the detected pericardium. The EFV is automatically computed using the standard fat attenuation range.

3.1 Methods

In this section, we present a detailed description of the individual steps of our approach, including multi-atlas segmentation method for the initial segmentation of the heart region and pericardium, pericardium detection, followed by geodesic active contours deformation.

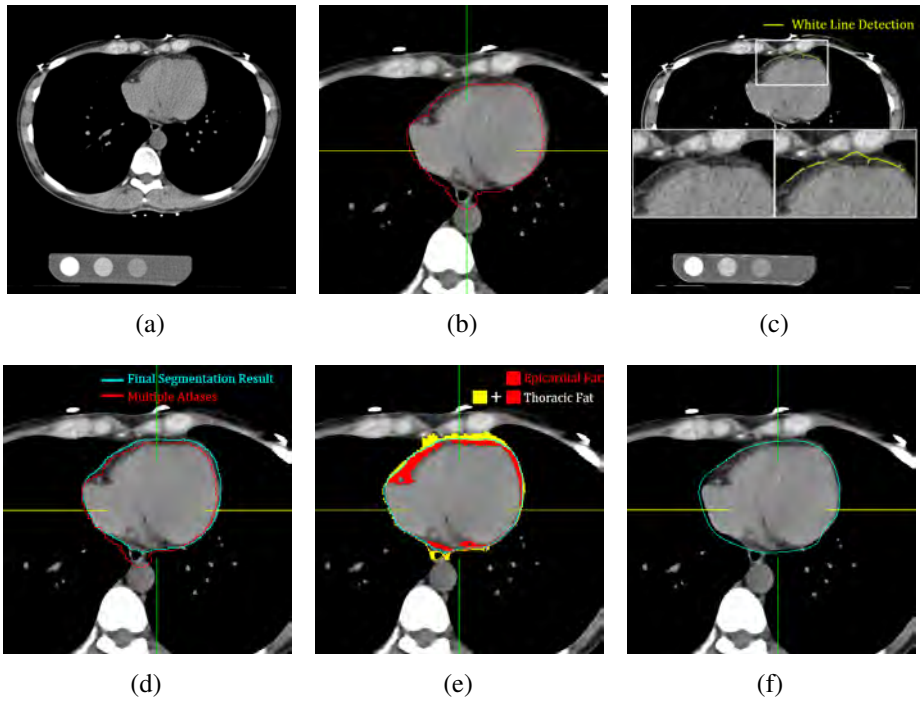

(a) (b) (c)

(d) (e) (f)

Figure 3.1: *Main steps of the algorithm (a) input image (3D volume), (b) rough location of pericardium obtained from multiple co-registered atlases (red contour), (c) pericardium detection, (d) the multi-atlas initialization (red) and refined pericardium segmentation (blue), (e) epicardial fat quantification, (f) expert manual tracing is shown for comparison.*

Figure 3.1 shows the main steps of the algorithm. A non-contrast CT atlas (multi-atlas) is first created from multiple co-registered non-contrast CT datasets in which the cardiac region and pericardium are manually segmented. Then, the global location and shape of the pericardium are initialized by a combination of multiple registrations and label propagation from the multi-atlas to the test non-contrast CT data (Figure 3.1(b)). Subsequently, the pericardium detection process (Figure 3.1(c)) identifies the candidates for pericardial voxels, In the next step, the initial multi-atlas boundaries are deformed by the geodesic active contours [Caselles et al., 1997], which are driven by the pericardium detection results (Figure 3.1(d)). Finally, the volume of the epicardial fat is computed (Figure 3.1(e)) within the pericardial sac boundaries using preset fat attenuation thresholds [Dey et al., 2008].

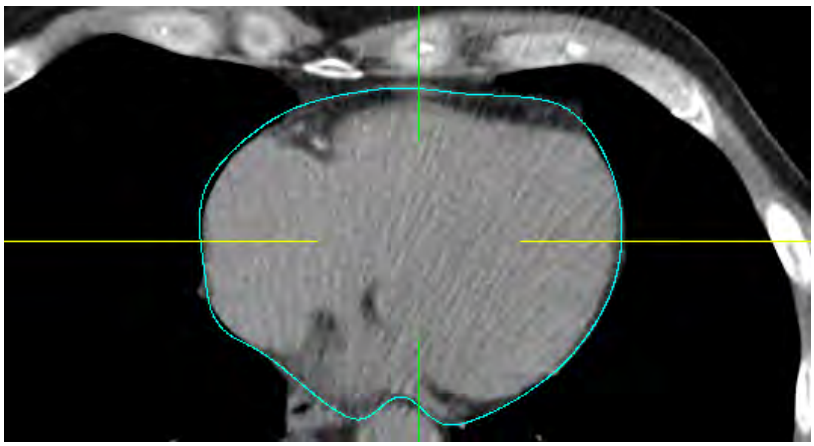

Figure 3.2: *An example of a manually-segmented contour on an atlas image*

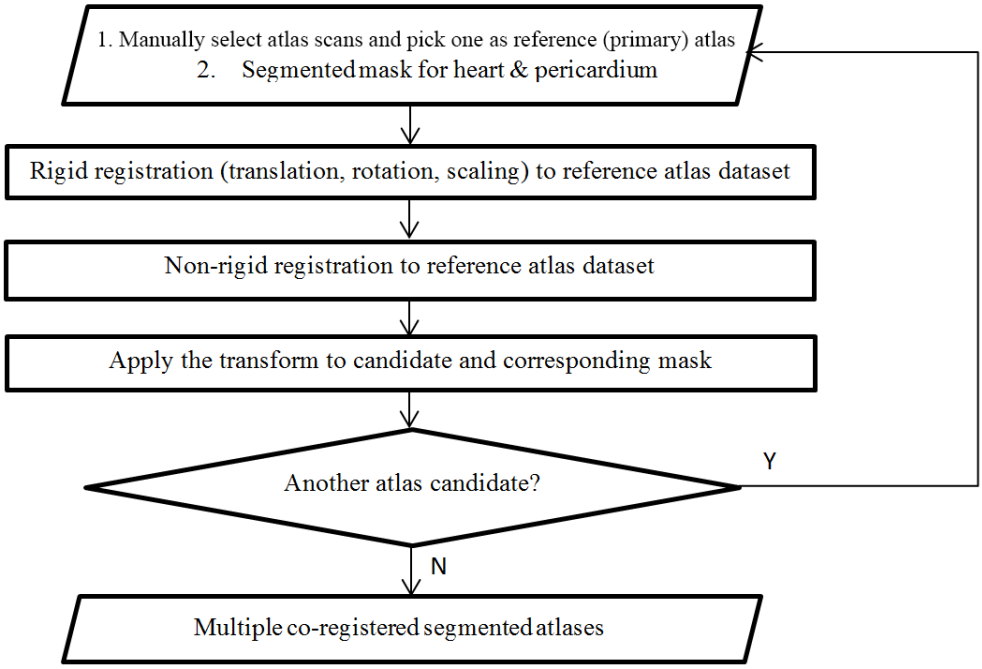

Figure 3.3: *Flowchart of the atlas creation procedure*

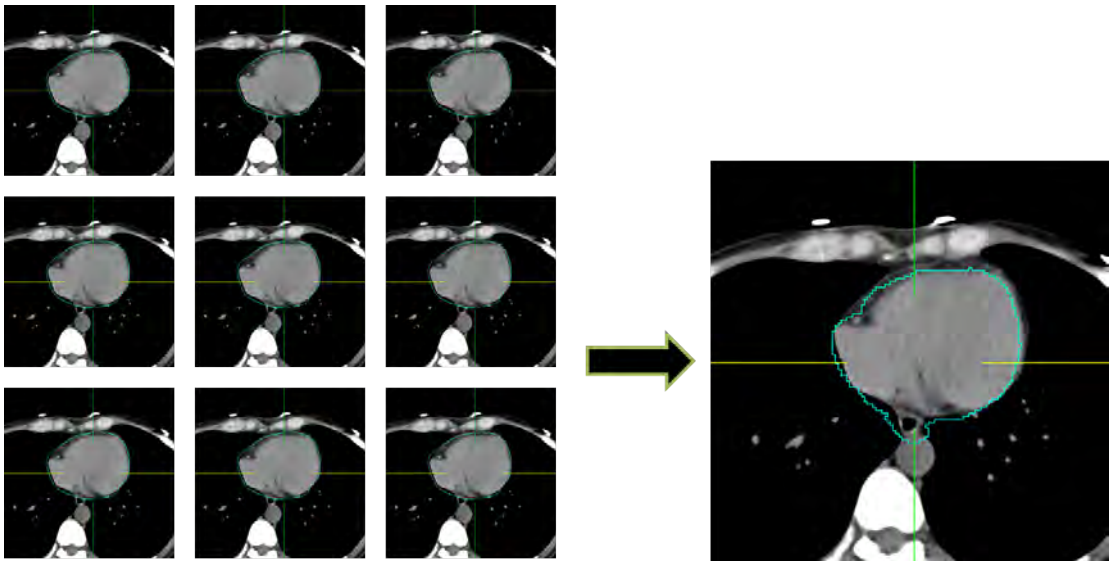

Figure 3.4: *Heart region initialization from multi-atlas registration*

3.1.1 Multi-Atlas Segmentation

The multi-atlas segmentation determines the initial location and shape of the heart and pericardium. The atlas was created from multiple patients scans (N = 10; 5 men and 5 women). For the atlas creation, on all transverse slices, 2D pericardial contours were manually traced by an expert cardiologist physician within the superior and inferior limits of the heart (Figure 3.2). A 3D binary volume mask was generated from the 2D contours. Both atlas creation (Figure 3.3) and target image segmentation are achieved by image registration. The non-linear registration required for the atlas creation is computationally expensive. For the purpose of initial rough heart region segmentation, we accelerated the registration process by co-registering all the atlas images to a randomly selected primary atlas image with high image quality (low noise and no motion artifacts), as chosen by an expert radiologist. During segmentation of test patient data, only one transformation is computed between the primary atlas image and the patient image. This transformation is then applied to all the images in the atlas (Figure 3.4). This approach requires only one registration, with possibly lower segmentation accuracy.

The rigid and nonrigid registration problem is formulated as an optimization problem with respect to combined affine and B-spline transformations μ minimizing the difference between the target images and the reference image:

$$\widehat{\mu} = \arg\min_{\mu} C[\mu; U(\mathbf{p}), A(\mathbf{p})], \tag{3.1}$$

where $\widehat{\mu}$ is the transformation aligning atlas $A(\mu(\mathbf{p}))$ to target image $U(\mathbf{p})$, $\mathbf{p}$ denotes a voxel, and C is the negative mutual information [Thévenaz and Unser, 2000].

To obtain the rough binary segmentation of the pericardium $S(\mathbf{p})$, the labels S_i are propagated to the test image according to spatially varying decision fusion weights [Isgum et al., 2009] that define the contribution of each atlas by measuring the similarity between the transformed moving atlas after registration and the target image. The similarity is measured by the absolute difference D_i between the transformed moving atlas and the target image:

$$D_i(\mathbf{p}) = |A_i(\mu(\mathbf{p})) - U(\mathbf{p})|, \forall i. \tag{3.2}$$

To determine how much a propagated label in each atlas image should contribute to the segmentation, weights λ_i were calculated as follows:

$$\lambda_i(\mathbf{p}) = \frac{1}{D_i(\mathbf{p}) \times g_{\sigma_1}(\mathbf{p}) + \epsilon}, \tag{3.3}$$

where $g_{\sigma_1}(\mathbf{p})$ is a Gaussian kernel of scale sigma that smooths the local estimate of the registration, and ϵ is a small value to avoid division by zero. The resulting propagation label is determined by a weighted average of the transformed binary segmentation $S_i(\mu)$:

$$S(\mathbf{p}) = \frac{1}{\sum_{i=1}^{N} \lambda_i(\mathbf{p})} \sum_{i=1}^{N} \lambda_i(\mathbf{p}) S_i(\mu_i(\mathbf{p})). \tag{3.4}$$

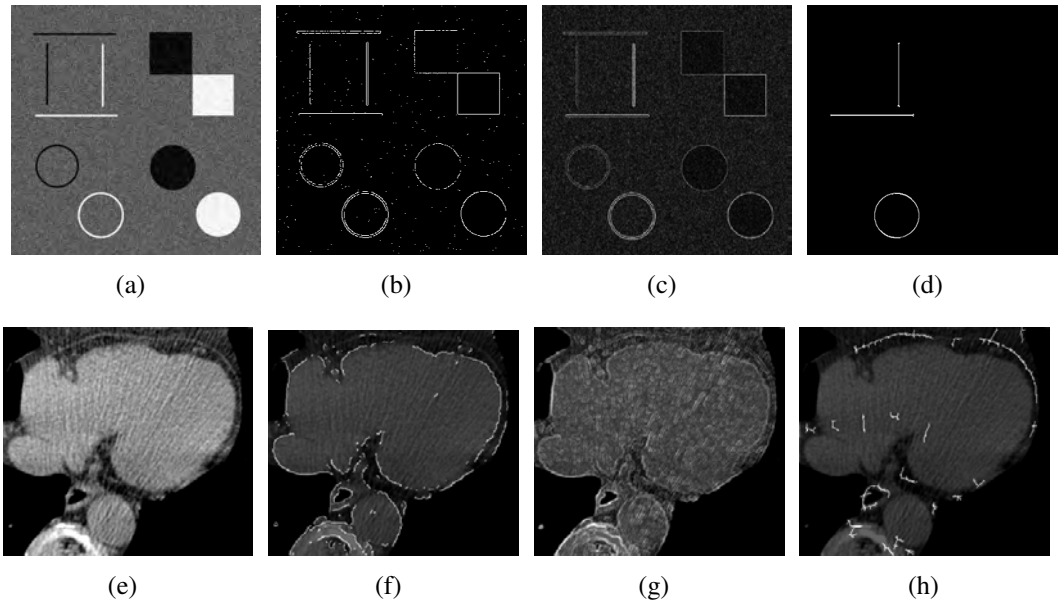

Figure 3.5: *Comparison of edge/line detection methods: (a,e) input synthetic and cardiac CT images, (b,f) Canny edge detection results: response to edges between any objects with different intensities. (c,g) gradient vector values: response to intensity change in any directions, especially the boundary of the heart. (d,h) our pericardium detection result: response mostly to the pericardial sac.*

3.1.2 Pericardium Detection

$$EP(x,y) = \begin{cases} r(x-d,y) + |r(x+d,y)|, & r(x-d,y) > 0 \text{ and } r(x+d,y) < 0, \\ 0, & \text{otherwise.} \end{cases} \tag{3.5}$$

To accurately localize the pericardium in the test image, $S(\mathbf{p})$ is transformed to a geodesic active contour model [Caselles et al., 1997] driven by image features that indicate where the active contours should stop evolving. However, a traditional line detection responds to all edge structures [Zhang et al., 2008] such as boundaries of the myocardium, edges between the heart and lungs and outlines of the spine, but it does not respond sufficiently to the poorly visualized pericardium (Figure 3.5). In a study of 260 patients by Delille et al. [1999], the maximal thickness of the normal pericardium was 2 mm for 95% of cases. Therefore, the width of the pericardium on the image in

unit of pixel can be calculated by the physical thickness of the pericardium divided by the physical size of the pixel. For instance, for our image data, which has a physical pixel size of 0.68 $\times$ 0.68 mm^2 on each transverse slices, we can calculate the maximal width of pericardium in pixel by $2\ mm/(0.68\ mm/pixel) \approx 3\ pixels$. As a result, we can set constant values to the width parameter in the pericardium detector described below. We have designed a feature detector that responds only to the pericardium, based on recent work in this area [Zhang et al., 2008]. By examining the convolution response of a first-order Derivative Of Gaussian (DOG) to the signal with the cross section of a bright line, a dark line, and edge, respectively, we found that the DOG response can distinguish these three patterns (Figure 3.6). As a result, we can extract only the center of the bright lines by filtering out other patterns in the convolution response using (3.5).

In (3.5), d is the half width of the line to be detected, $r(x,y) = \frac{-x}{\sqrt{2\pi\sigma^3}} e^{-\frac{x^2}{2\sigma^2}} \times I(x,y)$ for $|x| \leq 3\sigma, |y| \leq L/2$, σ is the standard deviation of the Gaussian function, and L is the length of the filter in the y direction. A fixed value of d can be used for pericardium detection because the width of the pericardium does not vary much across different subjects [Delille et al., 1999]. The response is then double thresholded [Russ, 2010] to obtain the centerline of the pericardium $T(EP(x,y))$, as shown in Figure 3.5(h). The pericardium detection result is then used as the external image-dependent force in the stopping function of the level-set geodesic flow. The stopping function $g(I)$ is defined as

$$g(I) = \frac{1}{1 + |T(EP(x,y)) + \bigtriangledown I|}, \tag{3.6}$$

which is responsible for stopping the contour at the pericardium without interference from other anatomical structures. In the above stopping function, $T(EP(x,y))$ is the detected pericardium centerline and $\bigtriangledown I$ is the gradient of the test image. The active contours can then lock onto the pericardium under the guidance of our stopping function after several iterations of evolution (< 200 in our experiments).

We also implemented the Gradient Vector Flow (GVF) active contour [Xu and Prince,

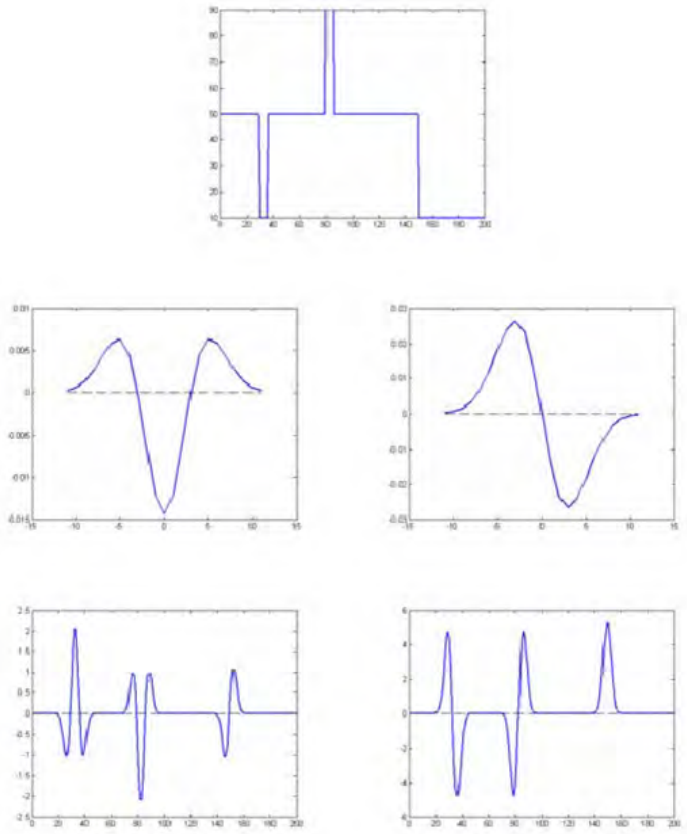

Figure 3.6: *Feature detector that responds only to the pericardium—1D signal response*

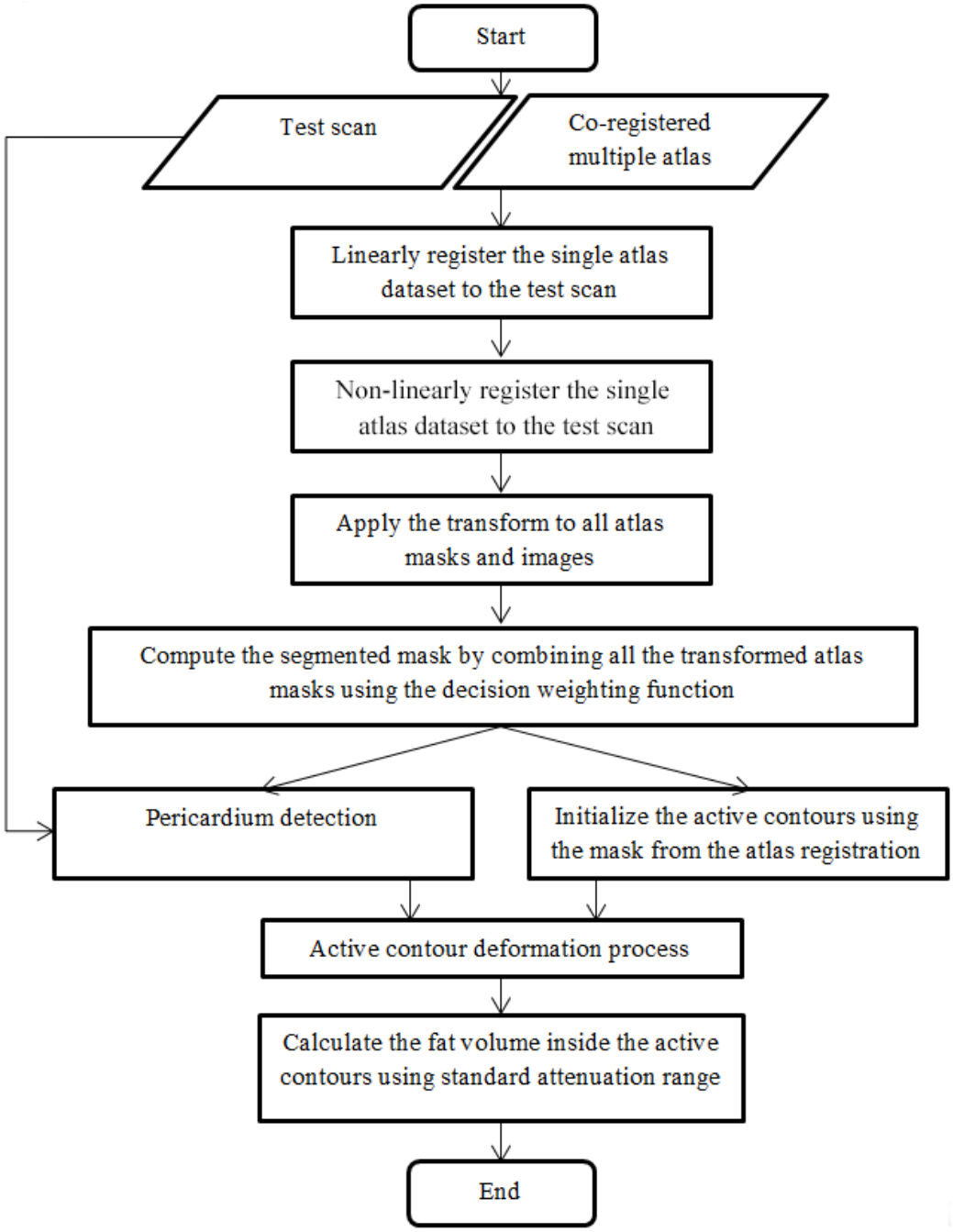

Figure 3.7: *The overall flowchart of the algorithm*

1998b], after initial atlas-based segmentation, to compare against our geodesic active contour method. We used gradient vector flow generated from the gradient image and pericardium detection on each transverse slice to direct the deformation of the active contour. After the segmentation of the pericardium, a previously established threshold of -190 to -30 CT units (i.e., Hounsfield units) [Dey et al., 2010c] is applied to fat-containing voxels within pericardial sac. This is the standard attenuation range for adipose tissue in non-contrast CT and has been validated by previous investigators [Dey et al., 2010c,b; Wheeler et al., 2005; Yoshizumi et al., 1999; Kvist et al., 1988; Sjostrom et al., 1986]. Using the same threshold range, very good inter-scanner reproducibility for quantification of epicardial fat volume has been shown by Nakazato et al. [2011] in 23 patients. The fat tissue voxels are then summed to provide epicardial fat volume in milliliters. Figure 3.7 summarizes the whole automatic quantification process.

3.1.3 Analysis of Algorithm Performance

Pearson's correlation, Bland-Altman comparison, and the paired t-test were used to compare the volume enclosed by the pericardium obtained by our algorithm to the ground truth determined by expert manual quantification. The overall Dice coefficient was used to measure the voxel overlap rate between them. We also calculated ten individual local Dice coefficients that describe the performance of our algorithm on different parts of the heart. To show the pericardium detection and active contours deformation process play an important role in EFV quantification, we gave results by only applying the multi-atlas segmentation on the same dataset.

3.2 Results

3.2.1 Image Data

We analyzed consecutive non-contrast CT data collected for the routine assessment of coronary calcium, at the Cedars-Sinai Medical Center. Institutional Review Board (IRB) authorization for retrospective analysis and patient consent for such retrospective analysis were obtained in all cases. The CT images were acquired on a 4-slice Multi-slice CT scanner (Siemens Volumezoom) or an Electron Beam CT scanner (GE Imatron e-Speed) using a standard prospectively ECG-triggered imaging protocol for coronary calcium scoring [Polonsky et al., 2010]. Each CT dataset comprised 50 to 60 image slices with a space resolution of 512 $\times$ 512 pixels of size 0.68 $\times$ 0.68 mm^2 and a slice thickness of 2.5-3.0 mm. The datasets were selected from consecutive, asymptomatic patients undergoing standard coronary calcium scoring, and they were free of motion artifacts.

3.2.2 Parameter Settings

By analyzing the properties of the image and searching in the parameter space, the best results were obtained with the following parameter setting. In multiple co-registered atlases segmentation, two resolutions were used for both affine and nonrigid B-spline registration in each of which 512 iterations of the stochastic gradient descent optimizer were performed. To estimate the derivative of the mutual information 4096 image samples were used, randomly chosen every iteration. For both affine and nonrigid registration 32 histogram bins were used. Gaussian smoothness with $\sigma_1 = 2$ voxels were performed on the difference image D_i before determining the weights for a decision fusion. In pericardium detection, the DOG filter has $d = 3$ voxels which is the half width of the line to be detected, $L = 12$ voxels which is the length of the filter in the y

Table 3.1: *Performance comparison among the pure multi-atlas-based method, WDFS method, multi-atlas with GVF active contours and proposed method.*

	Multi-atlas only	WDFS	Multi-atlas & GVF Snakes	Proposed method
EFV	63.55 ± 29.17 cm^3 *#	69.08 ± 36.11 cm^3 *#	69.89 ± 37.48 cm^3 *#	83.60 ± 32.89 cm^3 +
Mean Diff.	26.5 ± 15.9% #	12.7 ± 10.3% #	11.6 ± 9.6%	9.7 ± 7.4%
Bias	-19.61 cm^3	-11.16 cm^3	-11.96cm^3	1.75 cm^3
95% LoA	-49.49 cm^3 - 12.89 cm^3	-41.28 cm^3 - 15.73 cm^3	-37.19cm^3 - 13.27cm^3	-18.43 cm^3 - 14.91 cm^3
Correlation(R)	0.89 #	0.91 #	0.94	0.97
Dice coef.	0.88 (range 0.74 - 0.91)	0.89 (range 0.76 - 0.92)	0.88 (range 0.72 - 0.95)	0.92 (range 0.88 - 0.95)
Mean surface distance	1.0 ± 1.1 mm #	1.0 ± 0.9 mm #	1.0 ± 0.8 mm#	0.6 ± 0.9 mm
Hausdorff distance	5.5 ± 2.7 mm #	5.1 ± 2.9 mm #	5.6 ± 2.7 mm#	3.9 ± 1.7 mm

(* indicates significantly different from expert results, $p < 0.0001$)
(+ indicates not significantly different from expert results, $p = 0.15$)
(# indicates significantly different from the current proposed method, $p < 0.0001$)

direction and $\sigma = 2$ voxels which is the standard deviation of the Gaussian function. In geodesic active contour segmentation, the propagation scaling is 0.6, curvature scaling is 3.0, advection scaling is 1.0, maximum RMS error is 0.02 and number of iterations on each slice is 500. The Gradient Vector Flow Snake requires two parameters, they are used to generate the gradient vector flow external force field to drive the active contour: the number of iterations is 200 and the noise level of the input image is 2000.0.

3.2.3 Experiments

Our algorithm was applied to 50 CT datasets described above. To compare the automatic quantification results with expert manual delineation, two experienced cardiac imaging readers, using consensus reading, manually traced the pericardium for all patient datasets. The time required for each expert to perform these tracings was about 10 minutes per case.

Epicardial fat volume for the 50 test datasets was 83.60 ± 32.89 cm^3 as measured by our automated algorithm and 81.85 ± 34.28 cm^3 according to the expert manual quantification, with no significant difference by comparison of individual data points (p = 0.15). The Bland-Altman plot (Figure 3.8(a)) showed a positive bias of 1.75 cm^3 and the 95% limits of agreement ranged from -18.43 cm^3 to 14.91 cm^3 with 49 out of the 50

test cases within the limits of 2 standard deviations. The algorithm quantification results were in excellent correlation ($R = 0.97$, $p < 0.0001$) with the ground truth measurements (Figure 3.9). The mean Dice coefficient was 0.92 (range 0.88 - 0.95). The mean surface distance and Hausdorff distance in millimeter between manually drawn contours and the automatically obtained contours were 0.6 ± 0.9 mm and 3.9 ± 1.7 mm respectively. Mean percentage difference between the algorithm and experts was $9.7 \pm 7.4\%$, similar to the inter-observer variability between 2 readers ($8.0 \pm 5.3\%$, p = 0.3).

In another experiment performed on the same dataset, we disabled the pericardium detection and geodesic active contours deformation process in our algorithm to show that these two steps improved the performance of our previous atlas-based method [Dey et al., 2010a] significantly. Without pericardium detection and geodesic active contours deformation process, epicardial fat volume was underestimated as 63.55 ± 29.17 cm^3 which was significantly different from the expert manual quantification results ($p < 0.0001$). The Bland-Altman (Figure 3.8(b)) showed a large negative bias of -19.61 cm^3 and 95% limits of agreement ranged from -49.49 cm^3 to 12.89 cm^3 which was wider than that of the proposed method. The quantified volume by atlas had a lower correlation ($R = 0.89$, $p < 0.0001$) with the expert results. The average Dice coefficient was 0.88 (range 0.74 - 0.91). The mean surface distance and Hausdorff distance in millimeter were 1.0 ± 1.1 mm and 5.5 ± 2.7 mm respectively, which were both significantly different from the results from our hybrid algorithm ($p < 0.0001$). Mean percentage difference between the atlas-only algorithm and experts was $26.5 \pm 15.9\%$ which was significantly larger than our proposed method ($p < 0.0001$) and the inter-observer difference ($p < 0.0001$). A more advanced multi-atlas method, WDFS (Weighted Decision Fusion with atlas Selection), was implemented from [Isgum et al., 2009]. The performance on our 50 test cases using the current 10 patient atlas images was slightly better than our multi-atlas method alone but very similar. The computation time is increased and proportional to the number of registration performed.

In the experiment testing whether GVF active contours [Xu and Prince, 1998b] can better handle complex anatomic structure in the superior and inferior sections of the heart, we replaced geodesic active contours with GVF active contours in our algorithm. With GVF active contours, epicardial fat volume was estimated as 69.89 $\pm$ 37.48 cm^3 which was significantly lower compared to the expert manual quantification results ($p < 0.0001$). While the correlation was high ($R = 0.94$, $p < 0.0001$) for this method, the bias was -11.96 cm^3 and 95% limits of agreement ranged from -37.19 cm^3 to 13.27 cm^3 which was wider than that of the proposed method. The average Dice coefficient was 0.88 (range 0.72 - 0.95). The mean surface distance and Hausdorff distance in millimeter were 1.0 $\pm$ 0.8 mm and 5.6 $\pm$ 2.7 mm respectively, which are both significantly different from the results from our hybrid method ($p < 0.01$, $p < 0.0001$). Percentage difference from the experts was slightly higher than that of our hybrid method. Therefore, the overall performance of GVF active contour is slightly worse than that of the currently-utilized method. The detailed numbers were shown in TABLE 3.1.

To illustrate the performance of the proposed algorithm in individual cases, we show three examples of our fat quantification results. Two of them (Figure 3.10 and 3.11) were obtained from the 49 cases within the gray zone in the Bland-Altman plot (Figure 3.8(a)) and the third one is the largest outlier (Figure 3.12) on which the algorithm had the worst performance. The Dice coefficient of the three cases were 0.9168 in Figure3.10, 0.9453 in Figure 3.11 and 0.8806 in Figure 3.12. In each figure, automatic epicardial fat segmentation results are in the first row and expert tracing of the pericardium are shown in the second row. As we can see from Figure 3.10 and 3.11, the algorithm correctly detected the pericardium and segmented out the epicardial fat bounded by it. Figure 3.12 demonstrates the worst performance among the 50 test CT datasets. The contour which should overlap with the pericardium went beyond the imaged pericardium, which led to overestimation of the epicardial fat volume. In the superior section (Figure 3.12(a) and 3.12(d)), the contour was over-deformed due to unsuccessful registration. Note also that some of the epicardial fat voxels are incor-

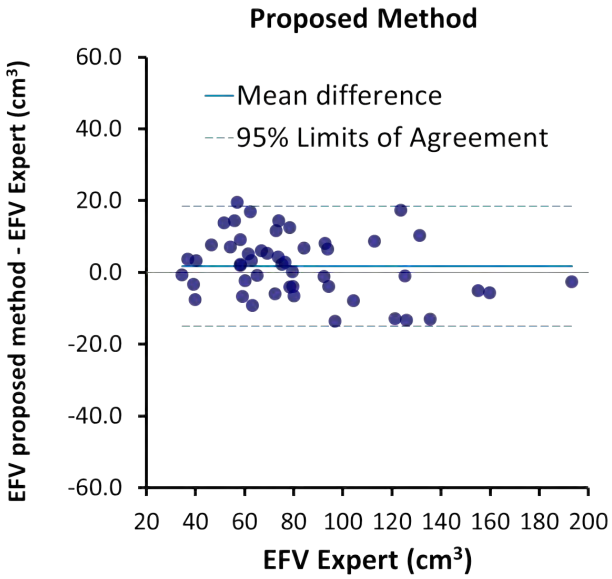

(a)

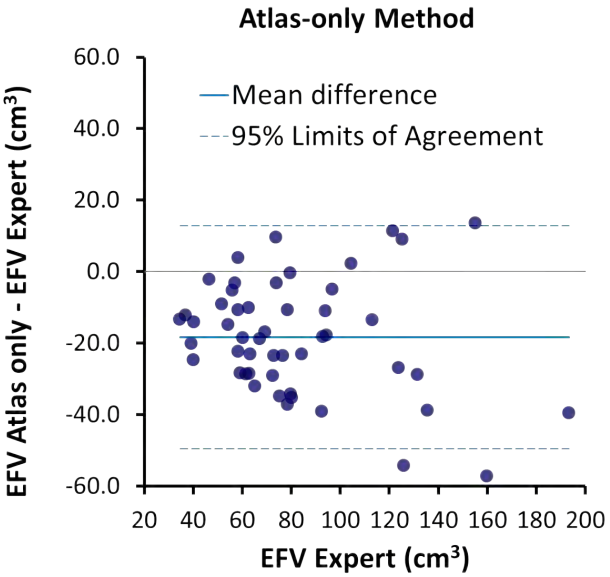

(b)

Figure 3.8: *Bland-Altman plot for epicardial fat quantification (comparison between the performances with/without pericardium detection and geodesic active contours deformation). (a) The proposed algorithm: the bias was +1.75 cm³ and the 95% limits of agreement ranged from -18.43 cm³ to 14.91 cm³. (b) Use multi-atlas initial segmentation only: the bias was -19.61 cm³ and 95% limits of agreement ranged from -49.49 cm³ to 12.89 cm³.*

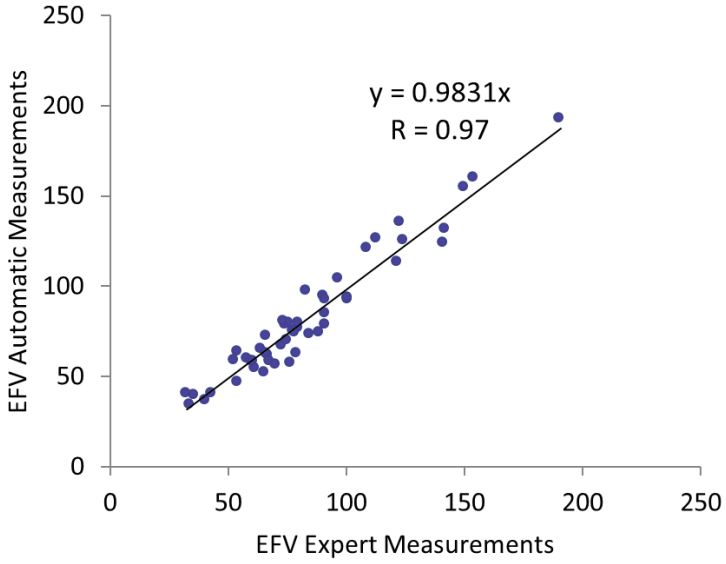

Figure 3.9: *Correlation between EFV quantification algorithm and expert measurements*

rectly identified in the middle of the heart due to the noisy data. We found that this CT data had minor reconstruction truncation artifacts compared with other normal coronary calcium score scans including those in our atlas. This was also a severely obese patient (BMI = 38 kg/m^2), which contributed to the big difference in the image appearance compared with the cases included in the atlas as well as noisy data due to severe photon attenuation in this patient. Significant difference between atlas images and target images, artifacts and high image noise may cause unsuccessful rigid and non-rigid registration which can introduce incorrect initialization for the active contours. Even if the pericardium detector successfully identified the pericardium, the active contours will not evolve to lock onto it starting from a location far away from the pericardium. This restriction is needed to avoid the contours evolving to other objects when there is no visible pericardium. Most cases with obesity in our experiment had EFV accurately quantified. There were 9 cases out of 50 with BMI over 30 kg/m2 (obese category). The mean difference of fat volume quantified for obesity group was 10.0 $\pm$ 12.3% which was not significantly larger than the overall mean difference 9.7 $\pm$ 7.4%.

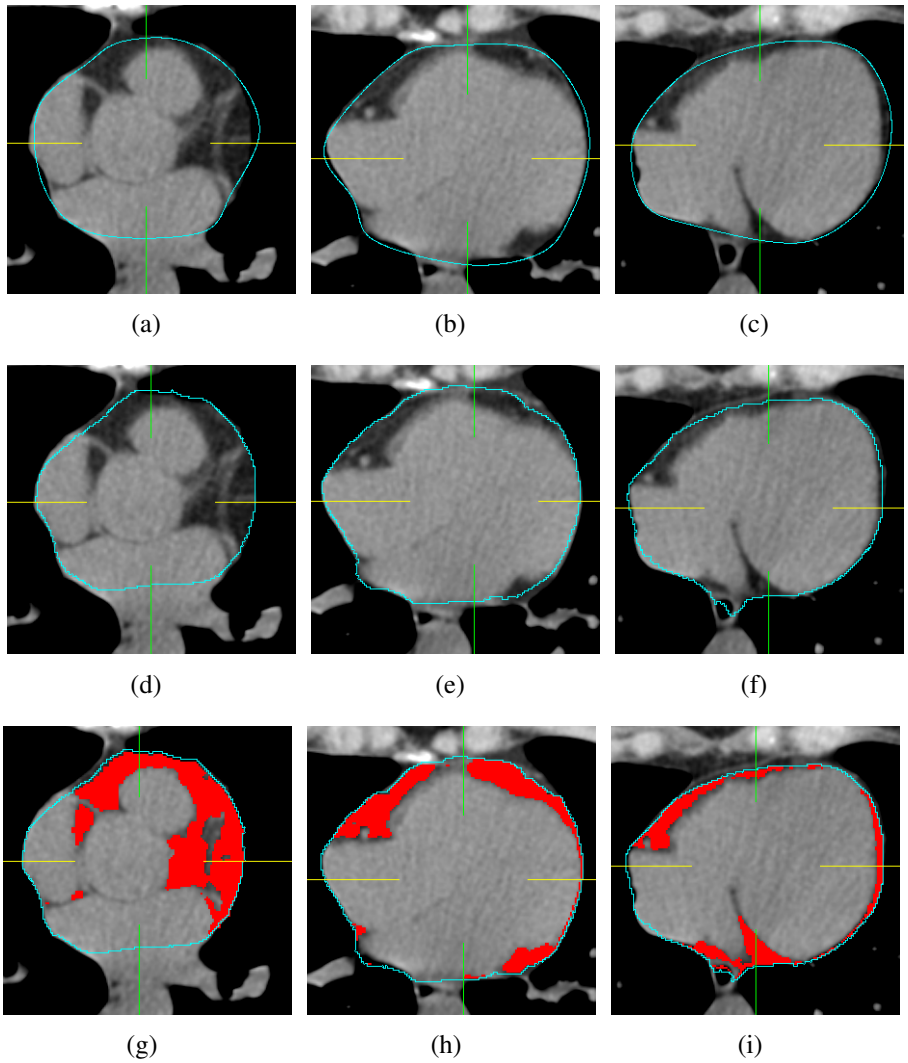

Figure 3.10: *Epicardial fat segmentation example with Dice coefficient 0.9168 and quantification results 60.2 cm^3 by the algorithm and 58.4 cm^3 by experts. (a), (b) and (c) are expert pericardium tracing results on sample slices in superior section, middle section and inferior section of the heart respectively. (d), (e) and (f) are the corresponding pericardium tracing results by our automated algorithm. (g), (h), (i) are automated epicardial fat segmentation results, in which epicardial fat was labeled in red.*

In Figure 3.13, we measured the local Dice coefficient by grouping the transverse slices from superior to inferior into 10 regions and calculating Dice coefficient for each region separately. It can be seen that the algorithm works very well on the middle regions but loses some accuracy in the outside regions especially in the superior section. The complex anatomy in the superior section of the heart, where the pericardium is attached

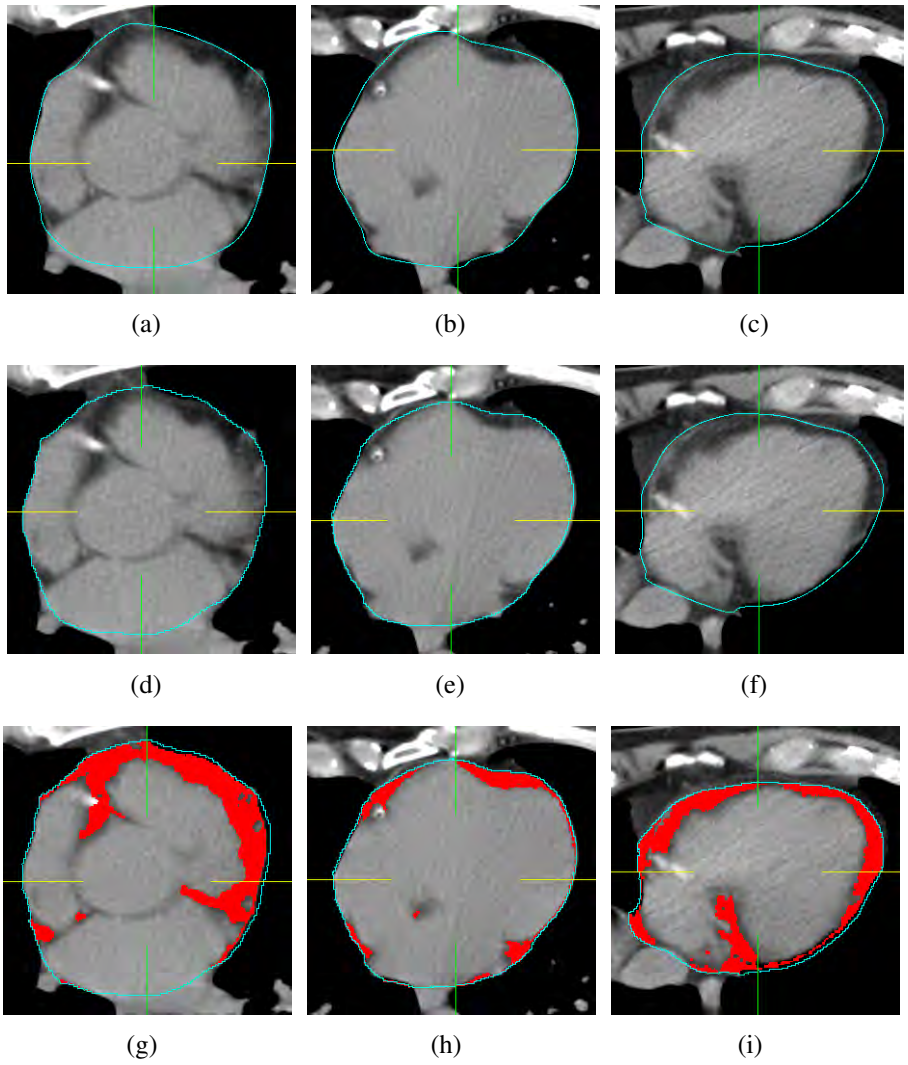

Figure 3.11: *Epicardial fat segmentation example with Dice coefficient 0.9453 and quantification results 91.4 cm^3 by the algorithm and 92.6 cm^3 by experts. (a), (b) and (c) are expert pericardium tracing results on sample slices in superior section, middle section and inferior section of the heart respectively. (d), (e) and (f) are the corresponding pericardium tracing results by our automated algorithm. (g), (h), (i) are automated epicardial fat segmentation results, in which epicardial fat was labeled in red.*

to aorta pulmonary veins and arteries is a major contributor to this problem. There was also less agreement in the inferior sections. It should be also noted that in both superior and inferior sections there is increased operator variability in placement of the reference boundaries, which is likely contributing to the apparent lower segmentation accuracy. Additionally, the contours bounding the pericardium in the superior and inferior sec-

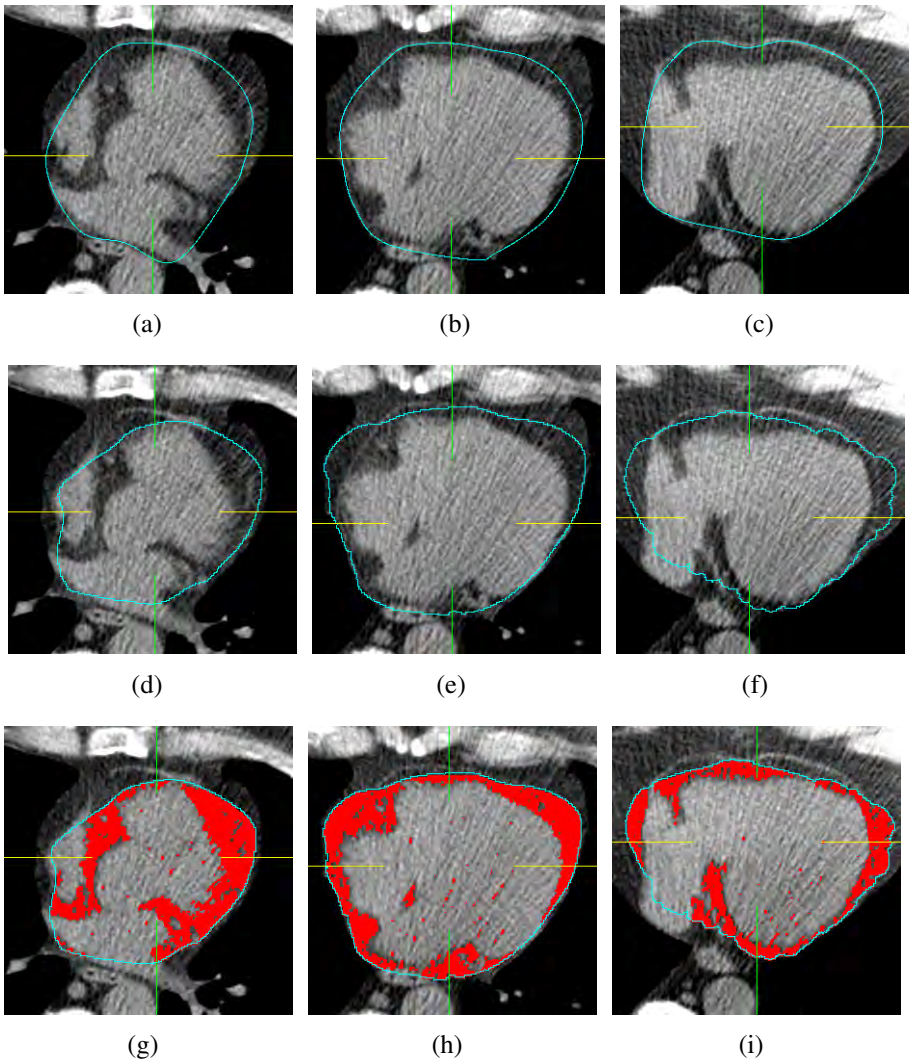

Figure 3.12: *Example of the worst performance on a patient with severe obesity (BMI = 38kg/m^2) with Dice coefficient 0.8806 and quantification results 180.7 cm^3 by the algorithm and 193.4 cm^3 by experts (a), (b) and (c) are expert pericardium tracing results on sample slices in superior section, middle section and inferior section of the heart respectively. (d), (e) and (f) are the corresponding pericardium tracing results by our automated algorithm. (g), (h), (i) are automated epicardial fat segmentation results, in which epicardial fat was labeled in red.*

tions have much less area than those in the middle part. Thus, they do not contribute significantly to the overall Dice coefficient.

This performance was achieved in 60 sec on a standard Windows PC (2.8 GHz CPU, 2GB RAM). On average, 11 seconds were used for rigid image registration, 24 seconds

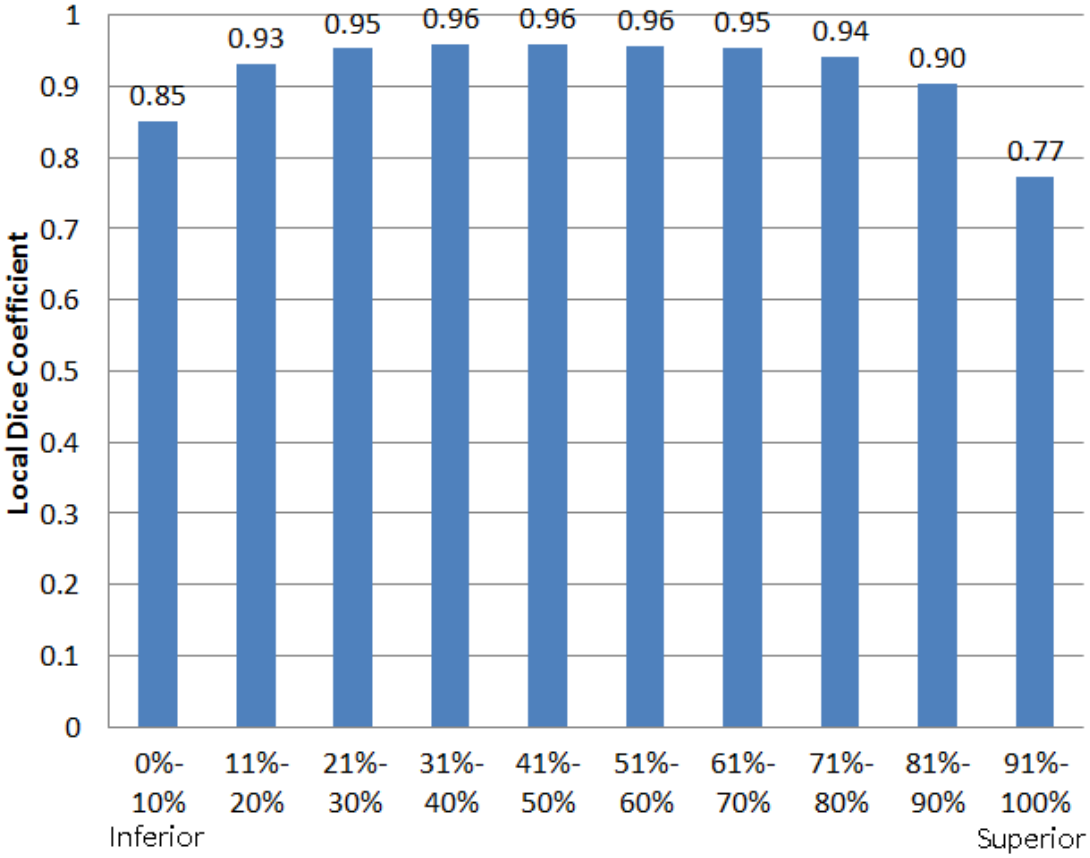

Figure 3.13: *Local Dice coefficient of pericardium on non-contrast CT from inferior section to superior section.*

for non-rigid registration and 25 seconds for the evolution of active contours.

3.3 Discussion

Automated robust segmentation of subtle anatomical features in images is one of the biggest challenges in accurate epicardial fat quantification. Some work has been previously reported in this area. Figueiredo et al. [2009] proposed a semi-automatic method for epicardial fat quantification. Their segmentation algorithm sweeps the anterior region from 0 to 180 degrees registering the higher intensity point along each direction to find control points belonging to the pericardium that appears in the image as a very thin line. In their method, users must manually set control points for spline interpolation in order to localize the pericardium line. Following this step, epicardial fat is quantified by considering only the pixels in the fat window of the CT image. Another semi-automatic method was proposed by Coppini et al. [2010], in which the task is separated into 2 steps. In the first step, an analysis of the epicardial fat intensity distribution is carried out in order to define suitable thresholds for a first rough segmentation. In the second step, a variational formulation of level set methods including a specially designed region homogeneity energy based on Gaussian mixture models is used to recover the spatial coherence and smoothness of fat deposits. This method also requires an expert observer to scroll the slices between the atrioventricular sulcus and the apex and to place control points on the pericardium. Shahzad et al. [2013] proposed an automated epicardial fat quantification method using a multi-atlas segmentation approach [Kirişli et al., 2010], similar to the atlas-based initialization part in our method. The authors registered an atlas created with CTA data to the non-contrast test CT scans to segment the pericardium. In our study on a different population, we have shown (Section 3.2.3) by comparing to the multi-atlas segmentation part of our algorithm that global registration of the heart region may not guarantee alignment of the pericardium and the later two steps (pericardium detection and active contours) significantly im-

prove the performance. While we compared to consensus reading by two experts in our study, rather than to independent experts, we achieved slightly higher Dice coefficient (0.92 v.s. 0.89), higher correlation (0.97 v.s. 0.91) and lower bias (1.75 cm^3 v.s. 16.6 cm^3), which could be the result of post-atlas refinement of our algorithm. In their approach, volume registration is performed on each of the atlas cases to achieve EFV quantification in one subject, which may be computationally demanding.

In contrast to these previous methods, we have applied a knowledge-based thin membrane detection method to detect the visible part of the pericardium. In order to accurately lock the segmentation contours onto the pericardium, we used active contour model driven by the pericardium detection result supported by the robust localization of the inner thoracic cavity and pericardium with a fast multi-atlas registration method. To lock the contour precisely to the pericardium, we initialize active contours from the atlas labels and drive it using a pericardium detector that extracts only the pericardium in the images. In addition, in our approach when the multi-atlas is created, individual atlas scans are co-registered to a primary image in order to avoid a costly one-to-all registration for the test image. As a result, when segmenting a single test image, the time-consuming registration process is performed only once. Although the atlas-based segmentation result is sensitive to the registration error between the primary atlas and the patient data, we used co-registered atlas to restrict the computation time. In our study, the initial atlas-based alignment was visually assessed for each case in our study and was found to be correctly aligned. It is also useful to note that the co-registered atlas-based segmentation is only the rough initialization of the heart position and shape, not the final contour which is expected to be accurate. We have validated the effect of pericardium detection and active contours deformation process in increasing the accuracy of the algorithm by comparing the performance to our atlas-based method [Dey et al., 2010a] and gradient vector flow active contours on the same datasets (Section 3.2.3). With only the multi-atlas segmentation, EFV was significantly underestimated, which caused lower correlation, dice overlap and higher bias. The two

Bland-Altman plots (Figure 3.8) drawn under the same scale and Table 3.1 illustrate the improvements in performance. To our knowledge, ours is the first method to use such atlas-initialized active contours to segment subtle anatomical features such as the pericardium. The atlas incorporate prior information may be changed by users, which may allow our framework to be applicable to contrast-enhanced cardiac CT, particularly coronary CT angiography.

There are some limitations in our approach. The selection of cases used to create the atlas may affect the performance of the initial segmentation of the heart and pericardium, which is a common limitation among atlas-based methods. We randomly selected the primary atlas instead of performing leave-one-out or cross-validation analysis on the atlas sets which might result in better performance. Sufficient number and diversity in atlas cases may enable the algorithm to have better performance on a wider range of test data. Nevertheless, the use of the geodesic active contours as a second step in our algorithm should minimize this problem.

CHAPTER 4

Automated Pericardial Fat Quantification From Coronary MRA

Pericardial Fat Volume (PFV) is emerging as an important parameter for cardiovascular risk stratification. In this chapter, we introduce a hybrid approach for automated PFV quantification from water/fat-resolved whole-heart non-contrast coronary Magnetic Resonance Angiography (MRA). Ten coronary MRA datasets were acquired on a 1.5T clinical scanner using a free-breathing, ECG-gated, balanced steady-state free-precession sequence with 3D radial trajectory and respiratory motion correction. Image reconstruction and phase-based water-fat separation were conducted off-line. Our proposed algorithm first roughly segments the heart region on the fat-water fused image using a simplified atlas-based segmentation with 4 cases in the atlas. To get exact boundaries of pericardial fat, a 3D graph-based segmentation is used to generate fat and non-fat components on the fat-only image. The algorithm then selects the components that represent pericardial fat using intensity features and their positions relative to the heart region. We validate the quantification results on the remaining six subjects and compare them with manual quantifications by an expert reader.

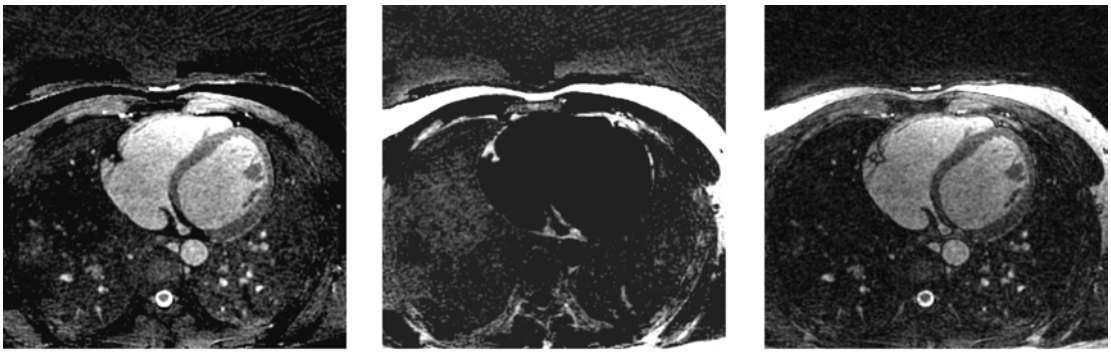

(a) water-only image (b) fat-only image (c) water-fat fused image

Figure 4.1: *Example of transverse slices of MRA data*

4.1 Methods

4.1.1 MR Acquisition

MR data were collected on a clinical 1.5 Tesla scanner (MAGNETOM Avanto, Siemens AG Healthcare, Erlangen, Germany) using a free-breathing, electrocardiograph-gated, balanced steady-state free-precession pulse sequence with 3D radial k-space trajectory and retrospective, image-based respiratory motion correction.

In this work, the motion-corrected CG-SENSE reconstruction is composed of two steps. In the first step, with the cardiac motion suppressed by ElectroCardioGraph (ECG) gating, the free-breathing dataset is segmented into different respiratory bins using self-navigation. With one bin being the reference, the respiratory motion of all other bins is estimated using image-based 3D affine registration, which has been shown to be a good approximation of the respiratory motion. Finally, the motion correction is accomplished by using the estimated translation vectors and affine transform matrices to modify the k-space data and trajectory. In the second step, the motion-corrected k-space data and trajectory is incorporated into the CG-SENSE reconstruction framework. For sensitivity self-calibration, we first reconstruct the motion-corrected individual coil images by gridding. We then calculate the coil sensitivity maps using Walsh's method

[Walsh et al., 2000], which uses the eigenvector of the local signal covariance matrices as the estimate of the respective sensitivity values at the specific spatial location. A stopping criterion need to be determined for the CG iterations. The SENSE encoding matrix is generally ill-conditioned. However, the CG method is intrinsically regularized with the iteration number effectively acting as a regularization parameter. So, the CG-SENSE reconstruction demonstrates a weak convergence behavior: the iterations initially converge toward a solution with a certain image quality, but with subsequent iterations the aSNR deteriorates due to noise amplification. In our experiments, we empirically found that a normalized residual of $\delta = 0.01$ yields the overall best trade-off between regularization and noise amplification. In there constructed datasets, this residual level corresponded to 20-25 CG iterations, depending on the degree of k-space undersampling. We perform retrospective undersampling to avoid the potential inter-scan variability associated with prospectively acquiring multiple undersampled datasets.The k-space trajectory is a slightly modified version of the "spiral on the sphere" [Wong and Roos, 1994] trajectory. Specifically, the k-space is divided into M interleaves, each one acquired over a certain number of heartbeats and containing N projections, whose origins form a spiral path on a sphere from one pole to the equator. The respective gradients are given by:

$$Gz(n) = \frac{(N-n)+0.5}{N}, \tag{4.1}$$

$$Gx(n) = cos(\frac{\sqrt{2N\pi}}{M} sin^{-1}(Gz(n) + m\theta_{GA}))\sqrt{1 - Gz(n)^2}, \tag{4.2}$$

$$Gy(n) = sin(\frac{\sqrt{2N\pi}}{M} sin^{-1}(Gz(n) + m\theta_{GA}))\sqrt{1 - Gz(n)^2}, \tag{4.3}$$

where $m = 1, 2, 3...M, n = 1, 2, 3...N$ and θ_{GA} is the $111.25°$ golden-angle, by which each of the M interleaves is rotated azimuthally with respect to the preceding one. We additionally set the azimuthal coverage of each interleaf to be $180°$ to traverse k-space frequently, therefore ensuring each respiratory bin to have uniform k-space coverage, at the same time minimizing the gradient jump to reduce eddy-current artifacts. With

the golden-angle azimuthal increments between interleaves, the retrospective undersampling is achieved by simply throwing away all heartbeats after the first N_i projections. The undersampling factor are determined by many aspects. The 3DPR trajectory typically contains significantly fewer projections than what is required for alias-free imaging set by the Nyquist criterion [Barger et al., 2002]. Effectively, a uniform angular undersampling reduces the size of the alias-free field of view (FOV) in the image domain according to the following square-root relationship with respect to the number of acquired projections:

$$FOV_{alias-free} \propto \sqrt{N_{proj}}. \tag{4.4}$$

To accommodate the wide spatial coverage from the nonselective excitation, we used a matrix size of 384^3 and an isotropic FOV of $400mm$ to minimize aliasing along the readout direction from peripheral signal sources such as the arms, the neck and the abdomen. Based on this matrix size, the number of projections to fulfill the Nyquist criterion is approximately 232,000, which is far from achievable in practice. However, assuming adequate magnetization-preparation across the excitation volume, the fat and muscle tissue will appear much darker than the brightest pixels from the ventricular blood pool. Therefore, streaks originating from the peripheral signal sources have lower intensity and consequently have minimal impact on the image quality within the central Region Of Interest (ROI). Because the heart spans less than one-third of the full FOV in all three dimensions, a relatively alias-free ROI can still be obtained if the alias-free FOV (4.4) is larger than the size of the heart. Based on this observation, we use 20,000 projections in the experiments as the maximally sampled reference, corresponding to an alias-free FOV size of 120 mm and approximately 10 min of scan time. As an initial test, retrospective undersampling was performed on one maximally sampled dataset in 2000 projection decrements. Each dataset were then reconstructed using the proposed CG-SENSE method, which were visually evaluated by an experienced reader to determine the required number of projections to achieve various image qualities relative to

the reference (N0): comparable to reference (N1), lower but acceptable (N2), and non-diagnostic (N3). Gridding reconstruction was also performed for comparison. Another potential source of image quality degradation is the accuracy of respiratory motion estimation. Around 40 heartbeats or 1000 projections are required in each respiratory bin for accurate image based motion estimation. Considering the distribution of data among the current six-bin setup is usually nonuniform, going below 10,000 projections will potentially lead to residual motion blurring due to inadequate motion correction for one or more respiratory bins.

The sequence parameters were as follows: repetition/echo time = $3.2/1.6ms$, field of view = $400mm^3$, matrix size = 384^3, voxel size = $1mm \times 1mm \times 1mm$, flip angle = 90°, and readout bandwidth = 900 Hz/pixel. No magnetization preparation pulses, such as fat-saturation and T2-preparation, were played out. Image reconstruction was completed off-line using self-calibrating non-Cartesian sensitivity encoding. More details of the MR acquisition and reconstruction framework can be found in Pang et al. [2015]. Water-only $I_w(\mathbf{p})$ (Figure 4.2) and fat-only $I_f(\mathbf{p})$ (Figure 4.3) images were calculated based on the pixel-by-pixel complex phase of the raw image [Hargreaves et al., 2003]. A sample dataset is shown in Figure 4.1.

With IRB approval and written consents obtained before the study, we scanned 10 healthy subjects, of which four were used to create the atlas, and the remaining six used for testing. To compare the automatic quantification results with expert manual delineation, an experienced cardiologist reader manually segmented the pericardial fat for all the subjects. The time required to perform these manual tracings was about 20-30 minutes per case. The absolute and percent difference, correlation, and Dice coefficient between the two segmentation results were calculated.

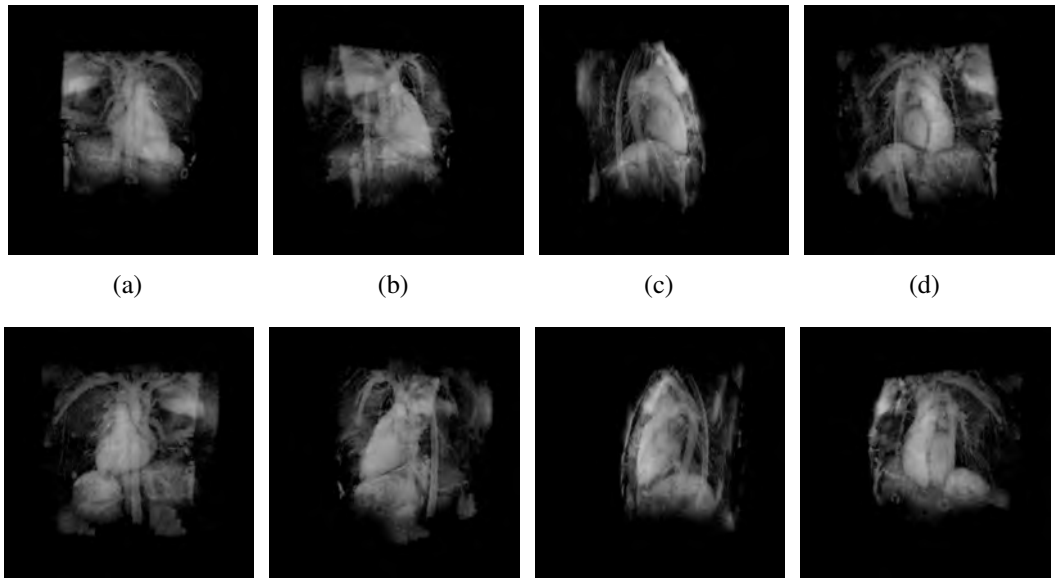

(a) (b) (c) (d)

(e) (f) (g) (h)

Figure 4.2: *3D rendering of the water-only MRA signal*

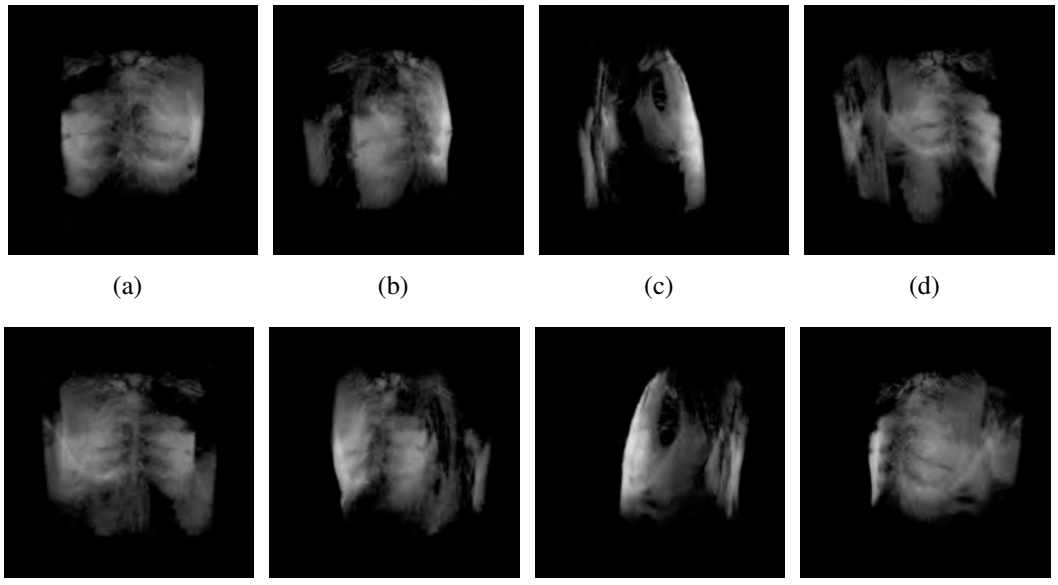

(a) (b) (c) (d)

(e) (f) (g) (h)

Figure 4.3: *3D rendering of the fat-only MRA signal*

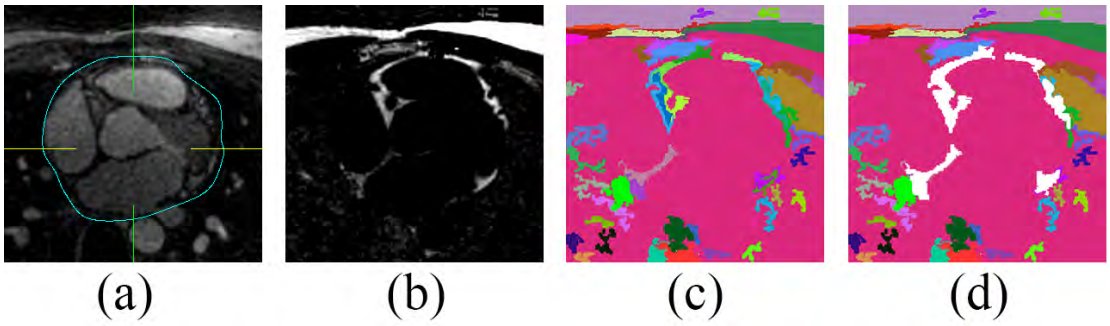

Figure 4.4: *Main steps of our algorithm. (a) Multi-atlas-based segmentation of the heart region. (b) Perform 3D graph-based segmentation on fat-only image. (c) Fat components and non-fat components. (d) Pericardial fat component selection (while components).*

4.1.2 Image Segmentation

On the basis of multi-atlas-based segmentation and efficient graph-based segmentation, we propose a quantification technique divided into two steps. First, the heart region initialization is performed using a simplified multi-atlas segmentation with local decision fusion [Isgum et al., 2009] on water-fat fused images (Figure 4.4(a)). Voxels are over-segmented into components on fat-only images using an efficient graph-based segmentation method [Felzenszwalb and Huttenlocher, 2004] (Figure 4.4(b)(c)), which we generalized from 2D space to 3D space in this work. The fat components with certain intensity features and overlap rate with the heart region masks are selected as pericardial fat (Figure 4.4(d)). A flowchart of our algorithm is presented in Figure 4.5.

4.1.2.1 Simplified Multi-Atlas-Based Heart Region Segmentation

The multi-atlas segmentation determines the initial location and shape of the heart. The atlas was created from multiple subject scans (water-fat fused images) with wide BMI range (N = 4; 2 men and 2 women, BMI 17, 22, 28, 35). For the atlas creation, on all transverse slices, 2D pericardial contours were manually traced by an expert cardiologist physician within the superior and inferior limits of the heart. A 3D binary

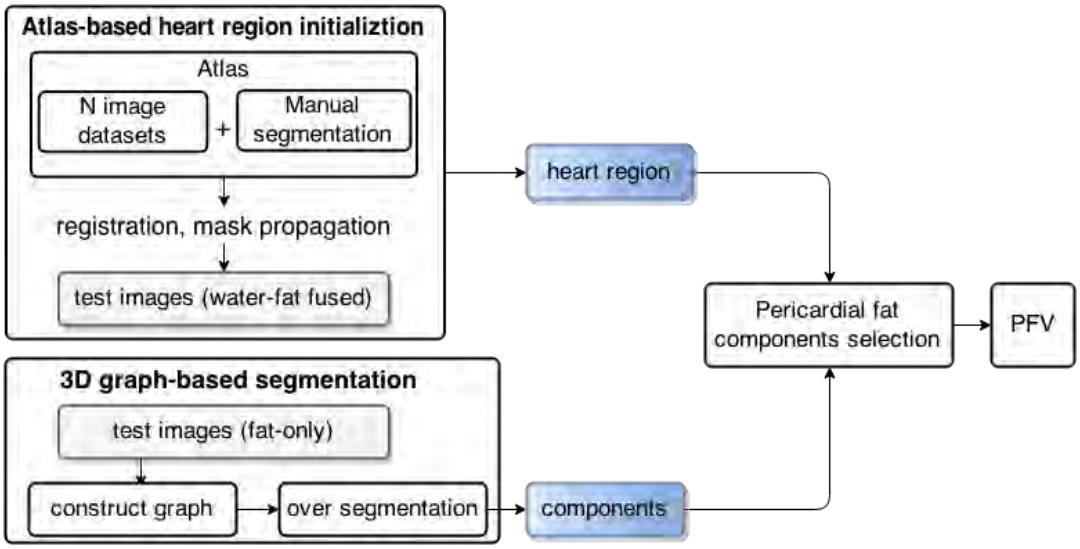

Figure 4.5: *Flowchart of the algorithm. First, the heart region initialization is performed on water-fat fused images. Voxels are over-segmented into components on fat-only images. The fat components with certain intensity features and overlap rate with the heart region masks are selected as pericardial fat.*

volume mask was generated from the 2D contours. Target image segmentation was achieved by one-to-all image registration between the target image and atlas images (Figure 4.6).

The rigid and nonrigid registration problem is formulated as an optimization problem with respect to combined affine and B-spline transformations μ minimizing the difference between the target images and the reference image:

$$\widehat{\mu} = \arg\min_{\mu} C[\mu; U_{wf}(\mathbf{p}), A_{wf}(\mathbf{p})], \tag{4.5}$$

where $\widehat{\mu}$ is the transformation aligning the water-fat fused atlas $A_{wf}(\mu(\mathbf{p}))$ to the target water-fat fused image $U_{wf}(\mathbf{p})$, where $\mathbf{p}$ denotes a voxel, and where C is the negative mutual information [Thévenaz and Unser, 2000].

To obtain the rough binary segmentation of the heart region $S(\mathbf{p})$ (Figure 4.4(a)), the labels S_i are propagated to the test image according to spatially varying decision fusion

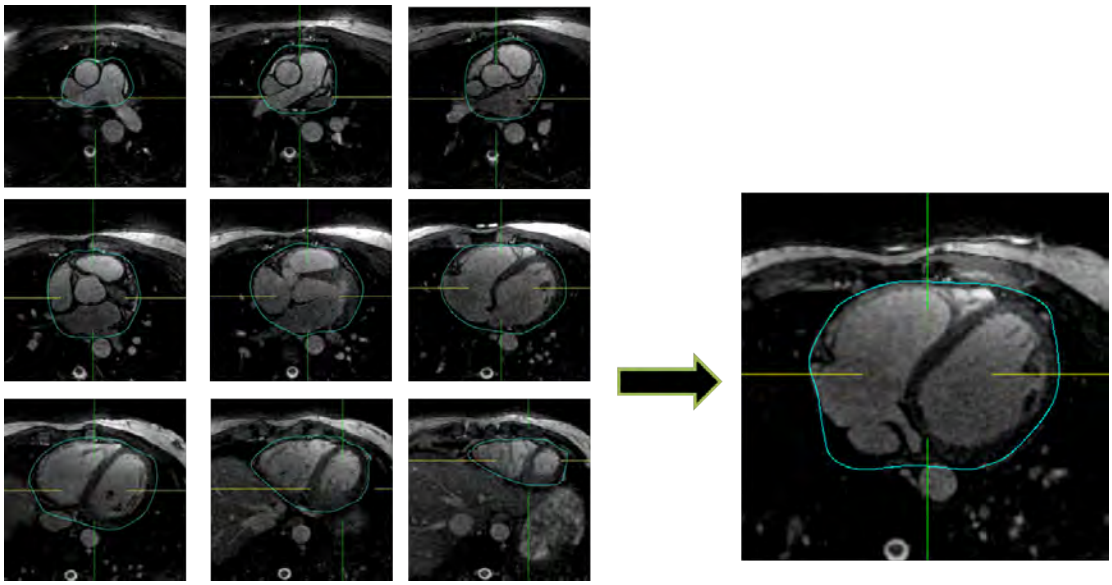

Figure 4.6: *MR atlas creation and registration*

weights [Isgum et al., 2009] that define the contribution of each atlas by measuring the similarity between the transformed moving atlas after registration and the target image. The similarity is measured by the absolute difference D_i between the transformed moving atlas and the target image:

$$D_i(\mathbf{p}) = |A_{wfi}(\mu(\mathbf{p})) - U_{wf}(\mathbf{p})|, \forall i. \tag{4.6}$$

To determine how much a propagated label in each atlas image should contribute to the segmentation, weights λ_i were calculated as follows:

$$\lambda_i(\mathbf{p}) = \frac{1}{D_i(\mathbf{p}) \times g_{\sigma_1}(\mathbf{p}) + \epsilon}, \tag{4.7}$$

where $g_{\sigma_1}(\mathbf{p})$ is a Gaussian kernel of scale sigma that smooths the local estimate of the registration and ϵ is a small value to avoid division by zero. The resulting propagation label is determined by a weighted average of the transformed binary segmentation

$S_i(\mu)$:

$$S(\mathbf{p}) = \frac{1}{\sum_{i=1}^{N} \lambda_i(\mathbf{p})} \sum_{i=1}^{N} \lambda_i(\mathbf{p}) S_i(\mu_i(\mathbf{p})). \tag{4.8}$$

The results of multi-atlas segmentation provide global localization of the heart region with limited accuracy at the boundaries of the pericardial fat due to the global registration scheme and the small atlas. The next graph-based segmentation step can generate the exact boundaries of the pericardial fat.

4.1.2.2 3D Graph-Based Fat Component Segmentation and Selection

We construct a fully-connected undirected 3D graph $G = (V, E)$ on the 3D fat-only image $I_f(\mathbf{p})$ with vertices $v_i \in V$ located on each voxel, and edges $(v_i, v_j) \in E$ corresponding to pairs of neighboring vertices. For each vertex, 13 out of all the 26 edges were constructed to connect with neighbor vertices as illustrated in Figure 4.7 to avoid overlapped edges. Each edge $(v_i, v_j) \in E$ has a corresponding weight $w((v_i, v_j))$, which is a non-negative measure of the dissimilarity between neighboring elements v_i and v_j. A segmentation S is a partition of V into components such that each component $C \in S$ corresponds to a connected component in a graph $G' = (V, E')$. The algorithm starts with initial segmentation S_{init}, where each vertex v_i is in its own component.

In this formulation, we want the voxels in a component to be similar and voxels in different components to be dissimilar; i.e., to have either fat voxels or non-fat voxels in one component. We define a predicate D based on [Felzenszwalb and Huttenlocher, 2004] for evaluating whether or not there is evidence for the boundary between two components in a segmentation. The predicate compares the inter-component differences to the within-component differences and is thereby adaptive with respect to the local characteristics of the data, hence dealing with intensity variation and noise in the MRA image.

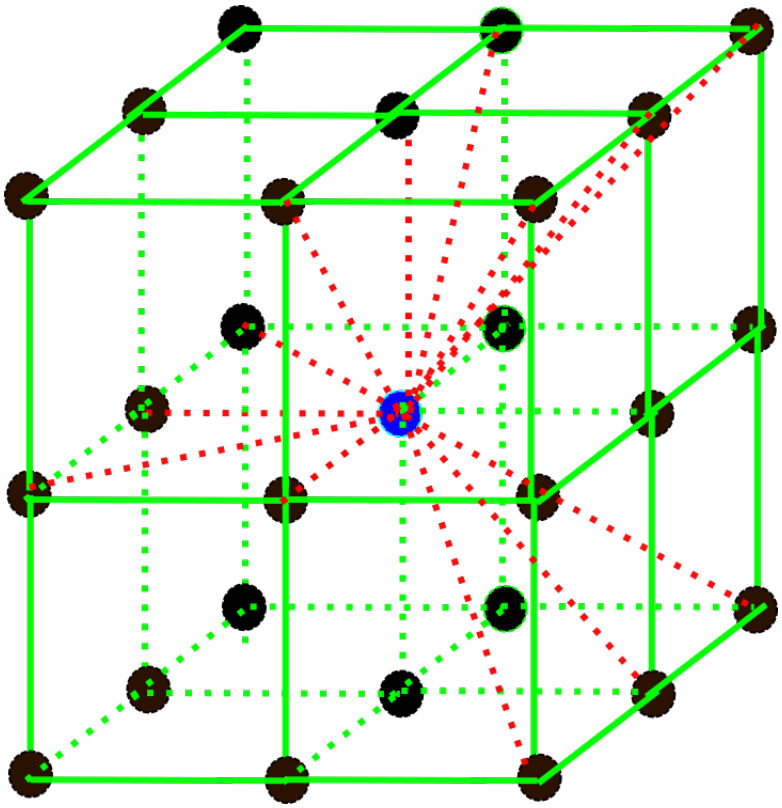

Figure 4.7: *3D graph edge construction. For every vertex, 13 out of all the 26 edges were constructed to connect with neighboring vertices. Blue vertex: current vertex; black vertices: 26 neighboring vertices; Red dashed lines: edges constructed for the current vertex*

The *internal difference* of a component $C \subseteq V$ is defined as

$$\text{Int}(C) = \max_{e \in MST(C,E)} w(e), \tag{4.9}$$

the largest weight in the minimum spanning tree $MST(C, E)$ of the component. The *difference between two components* $C_1, C_2 \subseteq V$ is defined as the minimum weight edge connecting the two components:

$$\text{Diff}(C_1, C_2) = \min_{v_i \in C_1, v_j \in C_2, (v_i, v_j) \in E} w((v_i, v_j)). \tag{4.10}$$

If there is no edge connecting C_1 and C_2, we let $\text{Diff}(C_1, C_2) = \infty$. The pairwise

comparison predicate is

$$D(C_1, C_2) = \begin{cases} true & if \quad \text{Diff}(C_1, C_2) > \text{MInt}(C_1, C_2), \\ false & otherwise, \end{cases} \tag{4.11}$$

where the minimum internal difference MInt is defined as

$$\text{MInt}(C_1, C_2) = \min\left(\text{Int}(C_1) + k/|C_1|,\ \text{Int}(C_2) + k/|C_2|\right), \tag{4.12}$$

where $|C|$ denotes the size of C and k is a constant parameter which sets a scale of observation. A larger k causes a preference for larger components, but k is not a minimum component size.

After we obtain all the 3D segment components C_i (Figure 4.4(c)) using the iterative algorithm in A, the mean intensity of each components t_i and overlap rate o_i with the heart region from last step are calculated. Components C_i with $t_i > T$ and $o_i > O$ are selected as pericardial fat components (Figure 4.4(d)), where T and O are threshold values for component mean intensity and overlap rate, respectively, with the heart region masks. The pericardial fat volume can be calculated by multiplying the total number of pericardial fat voxels by the voxel size.

4.2 Results

The pericardial fat volume for the 6 test datasets was quantified as 62.78 $\pm$ 27.85 cm^3 by our automated algorithm and 58.66 $\pm$ 27.05 cm^3 according to the expert manual quantification, with no significant difference ($p = 0.47$, mean percent difference 9.6 $\pm$ 9.5%) and excellent correlation ($R = 0.89$, $p < 0.01$). The mean Dice coefficient of pericardial fat voxels was 0.82 ± 0.06 (median 0.85). Figure 4.8 shows three views (transverse, coronal and sagittal) of the image data with pericardial fat segmentation

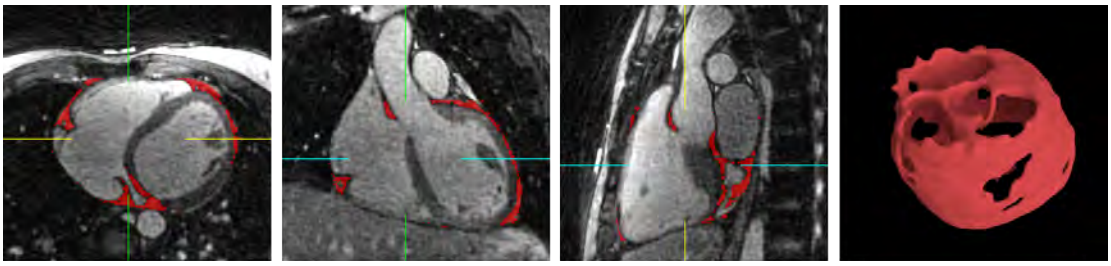

Figure 4.8: *Case example with algorithm segmentation overlay. Red overlay represents pericardial fat segmentation result by our algorithm. (a) transverse view, (b) coronal view, (c) sagittal view, (d) 3D model of pericardial fat voxels*

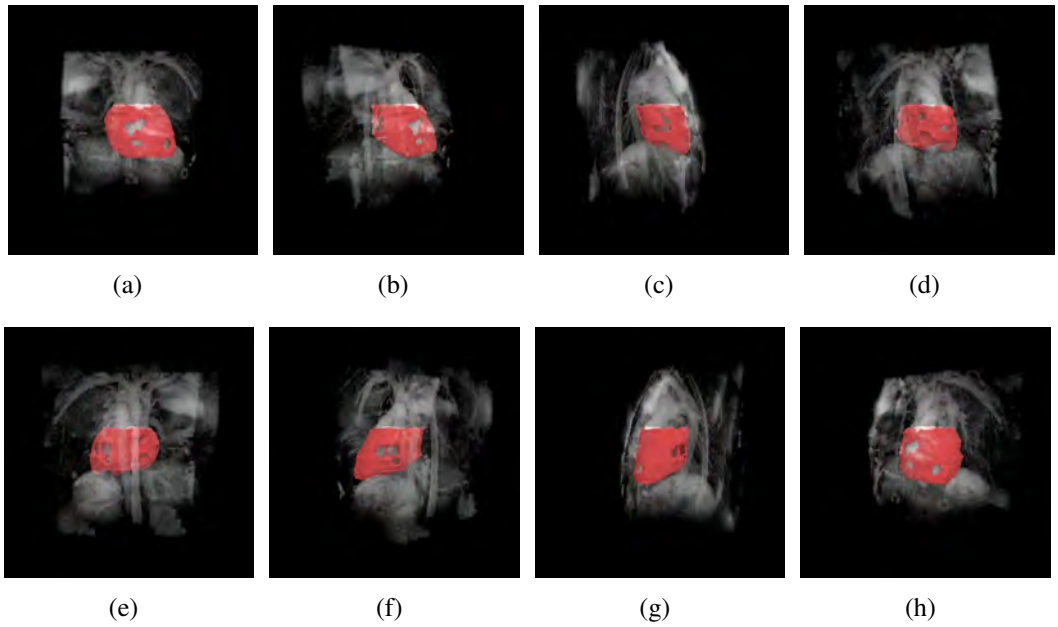

Figure 4.9: *3D rendering of the pericardial fat mask on MRA image*

result by our algorithm as red overlay, and the 3D model of pericardial fat voxels. Figure 4.9 is the 3D rendering of the segmentation result from eight directions.

Our algorithm is highly tolerant of error in the heart region masks from multi-atlas-based segmentation. Examples show that pericardial fat voxels and boundaries are correctly labeled despite the use of inaccurate heart region masks (Figure 4.10). The above performance was achieved on the multi-atlas-based heart region masks, which have a mean surface distance of 4.16mm and a Hausdorff distance of 7.5mm compared

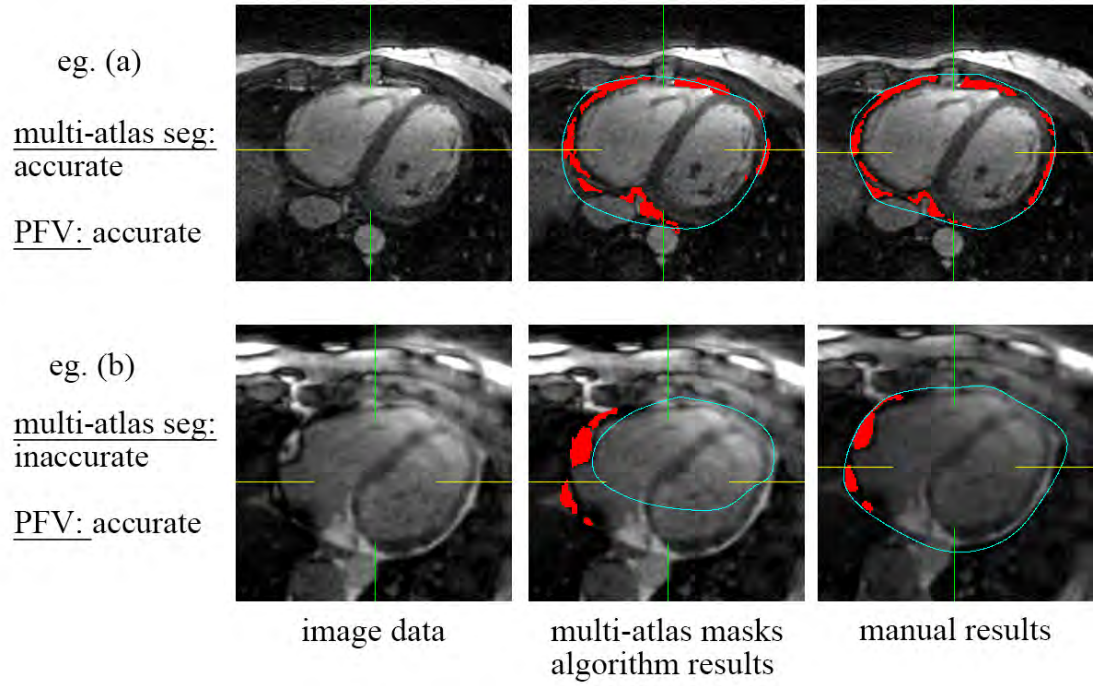

Figure 4.10: *Two examples demonstrating the robustness of our method. The red overlays represent pericardial voxels and the blue contours represent heart region boundaries. (a) Example accurate PFV quantification from accurate heart region initialization. (b) Example accurate PFV quantification from inaccurate heart region initialization.*

to the heart region masks drawn by the expert. Without using the 3D graph-based pericardial fat component selection (Section 4.2), the fat voxel mean Dice coefficient decreased from 0.82 to 0.62.

4.3 Discussion

Our imaging protocol is a needle-free non-contrast MRA imaging technique, using a standard 1.5T MR scanner [Pang et al., 2015] which allows direct visualization of the coronary artery stenosis. To our knowledge, our method is the first study showing feasibility of automated measurement of pericardial fat, a known cardiovascular risk factor, from these whole-heart images. The major advantage of our approach is that it permits automated measurement of pericardial fat as well as non-invasive assessment

of coronary artery stenosis, from same image data.

Dey [Dey et al., 2010a] and Ding [Ding et al., 2014, 2015b,c] also used multi-atlas-based algorithm for automated segmentation of the heart region and pericardial fat in CT images. With enough number of atlas images that captures major variations in different patients, multi-atlas-based methods can accurately segment the boundaries of the heart region without post-refining processing on cardiac CT, mainly due to the high resolution and high contrast characteristics of those images. However, pure multi-atlas-based algorithms could not achieve the same promising performance on finding the boundaries of the heart on our water/fat-resolved whole-heart non-contrast coronary MRA images due to lower image resolution, higher noise level and limited number of atlas cases. Our hybrid algorithm with graph-based segmentation and fat component selection after multi-atlas registration is highly tolerant of error in the heart region masks from multi-atlas-based segmentation. Pericardial fat voxels and boundaries can be correctly labeled with heart region initialization only provides rough heart position and shape without accurate boundary of the pericardial fat. The above performance was achieved on the multi-atlas-based heart region masks, which have a mean surface distance of 4.16mm and a Hausdorff distance of 7.5mm compared to the heart region masks drawn by the expert [Huttenlocher et al., 1993]. Without the 3D graph-based pericardial fat component selection (Section 4.2), the fat voxel overlap given by the mean Dice coefficient decreased from 0.82 to 0.62 when use only the multi-atlas segmentation mask.

In the literature on pericardial fat quantification from MR images, Wong et al. [2011] quantified pericardial fat by tracing the ROI manually using commercially available software (Argus, Siemens Medical Solutions). The images used were sequential steady-state free-precession short-axis cine sequences that were acquired with 6-mm slice thickness and no inter-slice gaps through the atria and 6-mm slice thickness with 4-mm gaps through the ventricles. Our approach may be more accurate by acquiring true 3D

volume images with slice thickness of 1mm and no gap between slices. The fat signal was also separated by the pixel-by-pixel complex phase of the raw image [Hargreaves et al., 2003], which is more reliable than human tracing. Though Wong et al. [2011] achieved low intra-observer and inter-observer variation (3.5% and 4.9%, respectively), our operator-less algorithm can produce no such variations and save time-consuming manual quantification by expert readers.

Having water-fat resolved images was key for the proposed method to accurately segmenting the pericardial fat. In this work, we used the bSSFP-based phase detection method due to its simplicity and being readily available from a modified coronary MRA protocol. Future works are warranted to evaluate Dixon-type multi-echo methods [Glover and Schneider, 1991; Reeder et al., 2005] to provide such images, which may offer more robust performance especially at higher field strengths.

A major limitation of this work is that we studied a small number of cases. Multi-atlas segmentation performance may increase with more atlas images that contains most possible variations among patients.

CHAPTER 5

Automated Coronary Calcium Scoring From Non-Contrast CT

Non-contrast cardiac CT is used worldwide to assess Coronary Artery Calcium (CAC), a subclinical marker of coronary atherosclerosis. Manual quantification of regional CAC scores includes identifying candidate regions, followed by thresholding and connected component labeling. In this chapter, we develop and validate a fully-automated, algorithm for both overall and regional measurement of CAC scores from non-contrast CT using a hybrid multi-atlas registration, active contours and knowledge-based region separation algorithm. A co-registered segmented CT atlas was created from manually segmented non-contrast CT data from 10 patients (5 men, 5 women) and stored offline. For each patient scan, the heart region, left ventricle, right ventricle, ascending aorta and aortic root are located by multi-atlas registration followed by active contours refinement. Regional coronary artery territories (left anterior descending artery, left circumflex artery and right coronary artery) are separated using a knowledge-based region separation algorithm. Calcifications from these coronary artery territories are detected by region growing at each lesion.

5.1 Methods

5.1.1 Image Data

We analyzed non-contrast CT data performed for routine assessment of coronary calcium, at the Cedars-Sinai Medical Center. The CT images were acquired on an Electron Beam CT scanner (e-speed, GE Imatron) or a 4-slice Multislice CT scanner (Volumezoom, Siemens) using a standard imaging protocol for coronary calcium scoring with prospective ECG-triggering. There were 50 to 60 slices in each CT dataset with resolution of 512 $\times$ 512, pixel size of 0.68 $\times$ 0.68 mm^2 and slice thickness of 2.5-3.0 mm. The datasets were selected from consecutive, asymptomatic patients undergoing standard coronary calcium scoring, and were free of motion artifacts.

5.1.2 Calcification Quantification

Multiple co-registered atlases [Ding et al., 2014, 2015a] with manual segmentation of four anatomic structures are first created from 10 (5 men, 5 women) non-contrast CT data (Figure 5.1(a)). Since the normal course of each coronary artery can be defined by its situation in one of the groves formed between the heart chambers [Jacobs, 2010], both the right and left ventricles, the whole heart region ascending aorta and aortic root were traced in axial images (Figure 5.1(b)). The algorithm then segments all the four anatomic structures on the test image by the combination of multiple registrations of multiple atlases to the test non-contrast CT data. The labels on the atlases propagate to the test data according to spatially varying decision fusion weights [Isgum et al., 2009] followed by a refinement process using active contours model [Kass et al., 1988]. We assigned the calcification to the specific coronary artery (left anterior descending artery, left circumflex artery and right coronary artery) territory using the heart chambers and aorta as landmark (Figure 5.1(c)) with a knowledge-based algorithm described below.

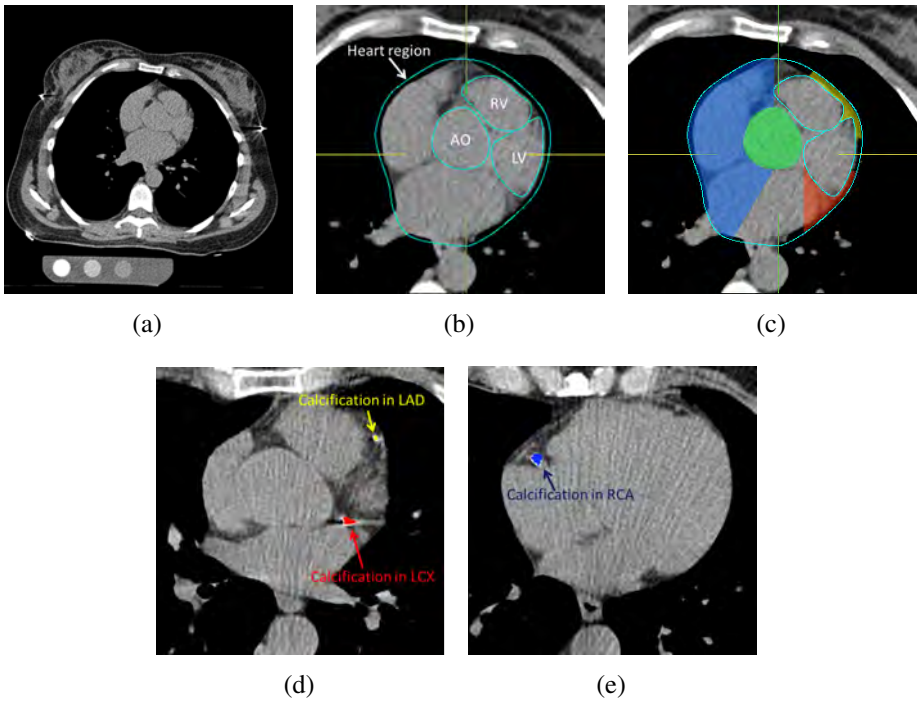

(a) (b) (c)

(d) (e)

Figure 5.1: *(a) Atlas non-contrast CT dataset, (b) segmentation of the heart region, ascending aorta / aortic root (AO), left ventricle (LV) and right ventricle (RV) in atlas data, (c) defining the expected territory for each vessel (LAD yellow, LCX red, RCA blue), (d) In patient data, calcium detection result in LAD and LCX, (e) calcium detection result in RCA.*

Finally, global and regional Agatston score [Budoff et al., 2006] and volume score [Callister et al., 1998] are calculated by applying a lower attenuation threshold of 130 Hounsfield Units (HU) and region growing at each lesion in 3 vessel regions respectively (Figure 5.1(d) and 5.1(e)).

In diagnostic cardiology, the Agatston score [Budoff et al., 2006], which was invented by Arthur Agatston, is a measure of calcium generally included in the results from a CT Test for Coronary Calcification. The Agatston score is derived from the work of Drs. Agatston and Janowitz of the University of Miami School of Medicine and dates back into the 1980s. The original work was based on electron beam computed tomography (also known as ultrafast CT or EBCT). The score is calculated using a weighted value assigned to the highest density of calcification in each calcified lesion.

The density is measured in Hounsfield units.

The density factor is defined as:

- 1 for $130 - 199$ HU
- 2 for $200 - 299$ HU
- 3 for $300 - 399$ HU
- 4 for 400 HU and greater

This weighted score is then multiplied by the area (in square millimeters) of the coronary calcification. For example, a "speck" of coronary calcification in the right coronary artery measures 5 square millimeters and has a peak density of 220 HU. The score is therefore 10 (5 square millimeters $\times$ weighted score of 2). The tomographic slices of the heart are 3 millimeters thick and average about 50-60 slices from the coronary artery ostia to the inferior wall of the heart. The calcium score of every calcification in each coronary artery for all of the tomographic slices is then summed up to give the total coronary artery calcium score (CAC score).

Due to an extensive body of research, it allows for an early risk stratification as patients with a high Agatston score (> 160) have an increased risk for a major adverse cardiac event (MACE) [Arad et al., 2000]. The following are grading of coronary artery disease (based on total Agatston score):

- no evidence of CAD: 0 calcium score
- minimal: $1 - 10$
- mild: $11 - 100$
- moderate: $101 - 400$

- severe: >400

Another method to measure coronary calcium include the calcium volume score. The calcium volume score is defined as the total calcium volume in coronary ateries in cubic millimeter, which is more reproducible than the Agatston score, but partial volume effects may impair the accuracy of the volume score.

We applied the same image segmentation method as described in Section 3.1.1.

In order to assign the calcification to the specific coronary artery, regions were defined in the expected territory for each vessel in our knowledge-based algorithm. Thus, the expected region for the left anterior descending artery was defined as the superior and anterior region between left and right ventricles (anterior interventricular groove), the expected region for the left circumflex was defined as the region left and posterior to the left ventricle (left atrioventricular groove), and finally the region expected for the right coronary artery was defined as the region located to the right and posterior of the right ventricle (right atrioventricular groove). The aortic root and ascending aorta were identified and traced in axial images to exclude aortic calcification (Figure 5.1(c)).

5.2 Results

Our automated quantification method was applied to 50 CT datasets. To compare automatic calcium quantification results with expert manual ones, several expert observers manually performed calcium scoring using commercial image annotation tools on the 50 test CT datasets. Pearson's correlation, Bland-Altman comparison and the paired t-test were used to compare the Agatston score and volume score obtained by the algorithm to expert manual scoring results.

Global Agatston score for the 50 test datasets was 922.8 $\pm$ 1309.3 by our automated algorithm and 871.2 $\pm$ 1182.9 from expert manual quantification and the mean percent

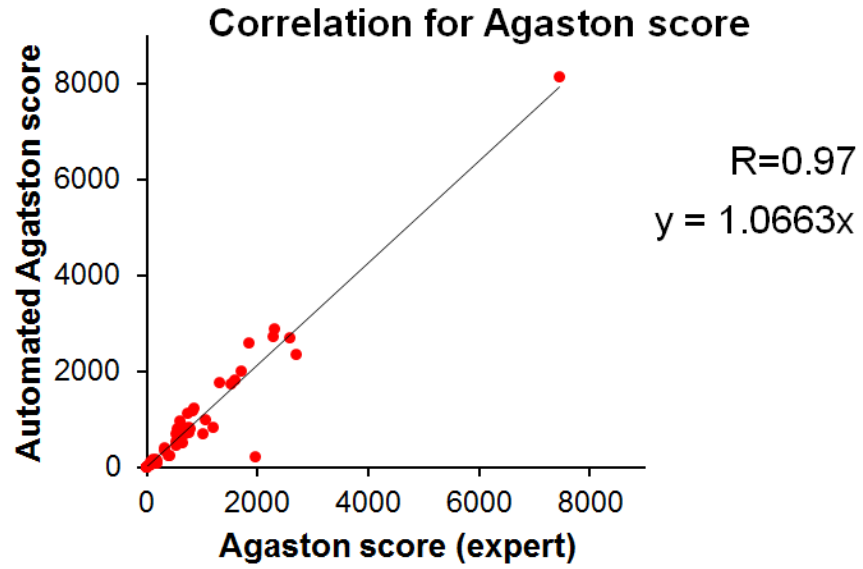

(a)

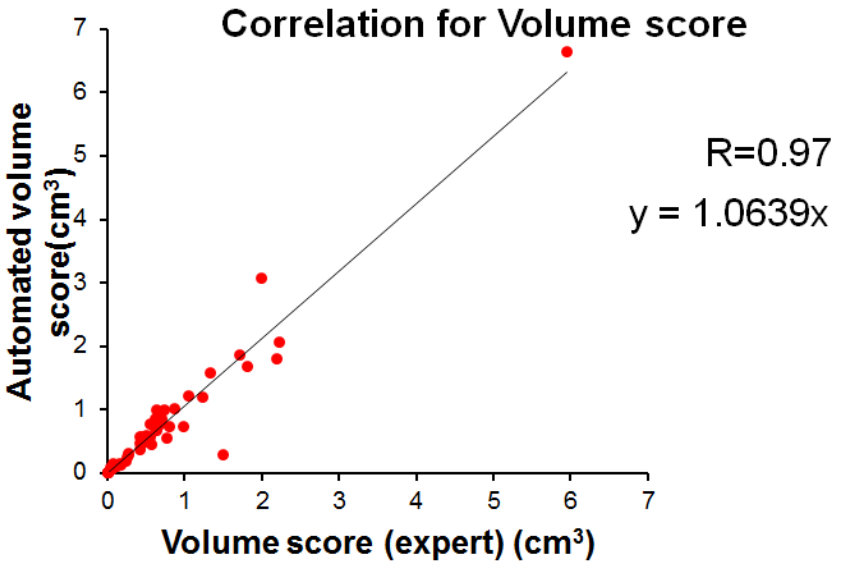

(b)

Figure 5.2: *(a) Correlation between algorithm result and expert Agatston score result. (b) Correlation between algorithm result and expert volume score result.*

difference between them is 22.5 $\pm$ 26.2%, similar to the mean inter-scan variability at 20-37% reported [Hong et al., 2003]. Agatston score showed correlation R = 0.97, p < 0.0001 with the ground truth (Figure 5.2(a)). The Bland-Altman plot (Figure 5.3(a)) shows a positive bias of 51.6 and the 95% limits of agreement ranged from -630.6 to 733.8.

Volume score for the 50 test datasets was 0.7438 $\pm$ 1.056 cm^3 by our automated algorithm and 0.7047 $\pm$ 0.9546 cm^3 from expert manual quantification and the mean percent difference between them is 20.2 $\pm$ 23.5%, similar to the mean inter-scan variability at 14-33% reported in [Hong et al., 2003]. The volume score also showed correlation R = 0.97, p < 0.0001 (Figure 5.2(b)) with the ground truth. The Bland-Altman plot (Figure 5.3(b)) shows a positive bias of 0.0391 cm^3 and the 95% limits of agreement ranged from -0.5171 cm^3 to 0.5953 cm^3.

This performance was achieved in 60 sec on a standard windows workstation.

5.3 Discussion

We have proposed a fully-automated method for global and regional CAC scoring from non-contrast CT by combining multi-atlas and knowledge-based vessel region separation algorithms. Our algorithm differs from previously published studies described below. Saur et al. [2008] and Shahzad et al. [2010] detected calcium in non-contrast CT in coronary arteries whose location was obtained by performing segmentation on contrast-enhanced scans. Isgum et al. [2007] detected coronary calcifications from non-contrast CT. The position of a potential coronary calcification was determined relative to the aortic and cardiac locations. Isgum et al. [2012] also published another classification approach for coronary calcium scoring in low-dose chest CT. Kurkure et al. [2010] detected coronary calcifications with a classification system employing a heart-centered coordinate system which was used to extract spatial features. Brunner et al. [2010] de-

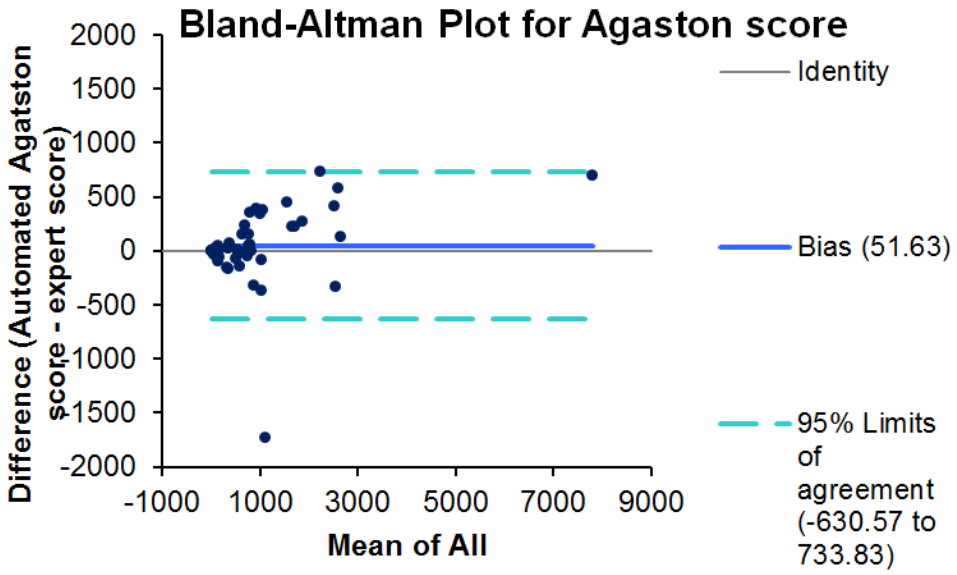

(a)

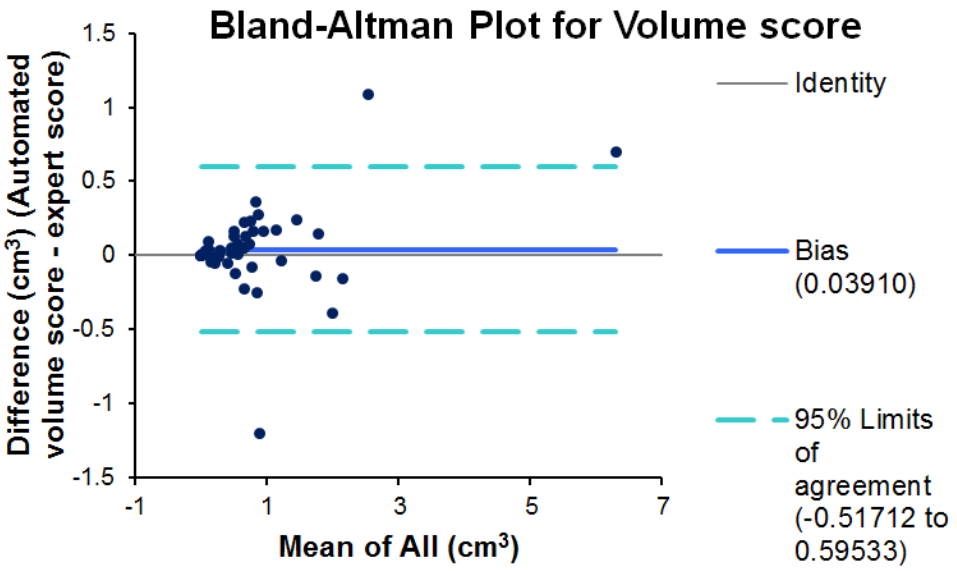

(b)

Figure 5.3: *(a) Bland-Altman plot for Agatston score: mean difference is 51.63, 95% limits of agreement is (-630.6, 733.8). (b) Bland-Altman plot for volume score: mean difference is 0.039 cm^3, 95% limits of agreement is (-0.517 cm^3, 0.595 cm^3).*

tected zones of the coronary arteries using the coordinate system described in [Kurkure et al., 2010]. Regional calcium scores were calculated using an equidistant division of the coronary artery zones. Our work is therefore different from those works due to its capability of quantifying calcium by each coronary artery zone. In comparison to Brunner's work on automated regional calcium scoring [Brunner et al., 2010], we achieved regional quantification of calcium by finding the left ventricle, right ventricle, whole heart, ascending aorta and aortic root on the patient images with multi-atlas registration and active contour refinement, and use the detected location to determine the coronary arteries territories using a patient-specific segmentation algorithm; our approach was shown to be successful in 50 test datasets.

CHAPTER 6

Conclusion

6.1 Summary and Contributions

Automated quantitative analysis of medical images enables physicians to objectively measure the severity of diseases, predict the risk factors of future events, and track disease development or treatment progress through time. This dissertation has demonstrated how image segmentation techniques can be applied to tackle the quantitative medical image analysis problem; in particular, focusing on the challenging problems of quantifying cardiac fat tissues and vessel calcified lesions that do not have a unified distribution pattern. Our contributions in this thesis have been three-fold:

First, our multi-atlas segmentation uses global registration to direct the label propagation from the altas images to the test image. This initialization procedure guides the local fine structure segmentation algorithms such as active contours to start in a position close to the target. Our hybrid approach of atlas registration and active contour segmentation proves to be effective for the accurate delineation of subtle image features such as the pericardium, while it preserves the location and shape of the anatomical structure of interest. This method will allow physicians and researchers to quantify the Epicardial Fat Volume (EFV) in patients quickly and largely without user intervention. We applied our novel EFV quantification algorithm on 50 patients undergoing routine coronary calcium assessment by CT. Measurement time was 60 seconds per-patient. EFV quantified by the algorithm (83.60 ± 32.89 cm^3) and expert readers (81.85 ± 34.28 cm^3) showed

excellent correlation (r = 0.97, $p < 0.0001$), with no significant differences by comparison of individual data points (p = 0.15). Voxel overlap by Dice coefficient between the algorithm and expert readers was 0.92 (range 0.88 - 0.95). The mean surface distance and Hausdorff distance in millimeters between manually drawn contours and the automatically obtained contours was 0.6 $\pm$ 0.9 mm and 3.9 $\pm$ 1.7 mm respectively. The mean difference between the algorithm and experts was 9.7 $\pm$ 7.4%, similar to inter-observer variability between 2 readers (8.0 $\pm$ 5.3%, p = 0.3). These results confirm that our novel automated method based on atlas-initialized active contours accurately and rapidly quantifies EFV from non-contrast CT.

Second, we have shown that to quantify Pericardial Fat Volume (PFV) with a completely radiation-free and needle-free scan, from non-contrast whole-heart coronary MRA images, is feasible via a hybrid approach using multi-atlas-based heart region initialization and 3D graph-based segmentation with selection of pericardial fat components. Multi-atlas segmentation driven by limited number of MRA atlas images with lower image quality than CT cannot guarantee accurate segmentation of the boundary of pericardial fat, while graph-based segmentation generates over-segmented fat components based on local voxel differences. To distinguish the pericardial fat components from the other types of fat components and keep the exact boundary of the fat, we performed a pericardial fat components selection procedure using the information from heart region initialization and image intensity. Our results demonstrate that the pericardial fat volume can be calculated directly from water-fat separated MRA images, which also provides coronary MRA data. To our knowledge, ours is the first report on an automated algorithm for PFV quantification from whole-heart, non-contrast coronary MRA images. We validated the quantification results on six subjects and compared them with manual quantifications by an expert reader. The PFV quantified by our novel algorithm was 62.78 $\pm$ 27.85 cm^3 compared to 58.66 $\pm$ 27.05 cm^3 by the expert, which were not significantly different ($p = 0.47$, mean percent difference 9.6 $\pm$ 9.5%) and showed excellent correlation ($R = 0.89$, $p < 0.01$). The mean Dice coefficient of pericardial

fat voxels was 0.82 ± 0.06 (median 0.85). These results suggest that our approach may potentially be applied in a clinical setting, allowing for accurate MR-based PFV quantification without tedious manual tracing.

Third, our research has made available to doctors fully-automated and accurate global and regional Coronary Artery Calcium (CAC) scoring from non-contrast CT. Our hybrid knowledge-based region separation algorithm can determine coronary artery territories based on the cardiac anatomic structures in each patient scan. To validate our new algorithm, global and regional Agatston scores and volume scores were calculated in 50 patients. Agatston scores and volume scores calculated by the algorithm and the expert showed excellent correlation (Agatston score: $r = 0.97$, $p < 0.0001$, volume score: $r = 0.97$, $p < 0.0001$) with no significant differences by comparison of individual data points (Agatston score: $p = 0.30$, volume score: $p = 0.33$). The total time was <60 sec on a standard computer. Our results show that fast accurate and automated quantification of CAC scores from non-contrast CT is feasible.

6.2 Future work

Reliable image segmentation lies at the foundation of objective quantitative analysis of medical images. Our new approaches for atlas-based segmentation still have space to improve. In creating the atlas, our radiologist manually selected several cases that represent a significant proportion of the population. The atlas image pool is static for all test cases, which leads to inaccurate segmentation on cases that are not similar to any of the atlas images. If the atlas pool is too large, the computational burden for one-to-all registration will not be practical in daily clinical practice. Furthermore, some of the atlas images may also have negative contribution to the accuracy of the segmentation. To improve the situation, additional labeled image data should be collected to construct the atlas image pool. An atlas selection procedure [Isgum et al., 2009] should be per-

formed before image registration and label propagation for every test image to obtain an optimal subset of atlas images that can be well aligned to the test image.

Other image segmentation approaches using large training datasets may have more reliable performance on a wider range of image quality and anatomic structure than atlas-based approaches. Template, probability, artificial neural network (ANN), and support vector machine (SVM) based automated segmentation methods are good alternatives for robust real-world application development when large training dataset are available.

Most current disease risk factors and bio-markers that are routinely quantified from medical images were designed or defined through human experience. Although they prove to be highly correlated with disease severity and future events in research work, those simple definitions may not be optimal for measuring and predicting certain diseases. For example, the way the Agatston Calcium Score is defined (see Chapter 5) is simply a 4-level intensity score multiplied by the lesion size. This definition traditionally simplified the calculation of the risk factor, but it sacrifices the predictive power of the factor. Today, practitioners take these well-known indicators/factors for granted and treat them as a standard. Data driven approaches should be applied to the design of optimal image features for disease prediction, with the objective of defining new factors that may generalize the original hand-crafted factors.

APPENDIX A

Graph-Based Fat Component Segmentation Algorithm and Properties

In this appendix, we describe and analyze the graph-based segmentation algorithm that we generalized from [Felzenszwalb and Huttenlocher, 2004] for fat and non-fat component segmentation in Section 4.1.2.2. We show that the fat components produced by this iterative algorithm are not too coarse nor too fine.

Definition 1. *A segmentation S is* too fine *if there exists one or more pairs of regions $C_1, C_2 \in S$ such that there is no evidence for a boundary between them.*

Definition 2. *A segmentation S is* too coarse *when there exists a refinement of S that is not too fine.*

If fat and non-fat components of a segmentation can be split and yield a segmentation where there is evidence for a boundary between all pairs of neighboring components, then the initial segmentation has too few components. There can be more than one solution that is neither too coarse nor too fine, so such a segmentation is not unique. For the aspect of existence, there is always some segmentation that is both not too coarse and not too fine, which is proved below.

Property 1. *For any (finite) graph $G = (V, E)$ there exists some segmentation S that is neither too coarse nor too fine.*

To explain why this property holds, we can start with a segmentation where all the elements are in a single component. Clearly this segmentation is not too fine, because

there is only one component. If the segmentation is also not too coarse, the property holds. Otherwise, by the definition of what it means to be too coarse there is a proper refinement that is not too fine. Pick one of those refinements and keep repeating this procedure until we obtain a segmentation that is not too coarse. The procedure can only go on for $n-1$ steps because whenever we pick a proper refinement we increase the number of components in the segmentation by at least one, and the finest segmentation we can get is the one where every element is in its own component.

The segmentation algorithm is similar to Kruskal's algorithm for constructing a minimum spanning tree of a graph. It can be implemented to run in $O(m \log m)$ time, where m is the number of edges in the graph.

Algorithm 1 Segmentation algorithm

Require: $G = (V, E)$ with n vertices and m edges
Ensure: A segmentation of V into components $S = (C_1, ..., C_r)$

1: Sort E into $\pi = (o_1, ..., o_m)$, by non-decreasing edge weight.
2: Start with S^0, where each vertex v_i is in its own component.
3: Repeat step 4 for $q = 1, ..., m$.
4: Construct S^q given S^{q-1} as follows. Let v_i and v_j denote the vertices connected by the q-th edge in the ordering, i.e., $o_q = (v_i, v_j)$. If v_i and v_j are in disjoint components of S^{q-1} and $w(o_q)$ is small compared to the internal difference of both those components, then merge the two components otherwise do nothing. More formally, let C_i^{q-1} be the component of S^{q-1} containing v_i and C_j^{q-1} the component containing v_j. If $C_i^{q-1} \neq C_j^{q-1}$ and $w(o_q) \leq MInt(C_i^{q-1}, C_j^{q-1})$ then S^q is obtained from S^{q-1} by merging C_i^{q-1} and C_j^{q-1}. Otherwise $S^q = S^{q-1}$.
5: Return $S = S^m$.

We show that a segmentation S produced by Algorithm 1 obeys the global properties of being neither too fine nor too coarse when using the component comparison predicate D defined in (4.11). That is, although the algorithm makes only greedy decisions it produces a segmentation that satisfies these global properties. Moreover, we show that any of the possible non-decreasing weight edge orderings that could be picked in Step 1 of the algorithm produce the same segmentation.

Lemma 1. *In Step 4 of the algorithm, when considering edge o_q, if two distinct com-*

ponents are considered and not merged then one of these two components will be in the final segmentation. Let C_i^{q-1} and C_j^{q-1} denote the two components connected by edge $o_q = (v_i, v_j)$ when this edge is considered by the algorithm. Then either $C_i = C_i^{q-1}$ or $C_j = C_j^{q-1}$, where C_i is the component containing v_i and C_j is the component containing v_j in the final segmentation S.

Proof. There are two cases that would result in a merge not happening. Say that it is due to $w(o_q) > Int(C_i^{q-1}) + \tau(C_i^{q-1})$. Since edges are considered in non-decreasing weight order, $w(o_k) \geq w(o_q)$, for all $k \geq q+1$. Thus no additional merges will happen to this component, i.e., $C_i = C_i^{q-1}$. The case for $w(o_q) > Int(C_j^{q-1}) + \tau(C_j^{q-1})$ is analogous. □

Note that Lemma 1 implies that the edge causing the merge of two components is exactly the minimum weight edge between the components. Thus the edges causing merges are exactly the edges that would be selected by Kruskal's algorithm for constructing the Minimum Spanning Tree (MST) of each component.

Theorem 1. *The segmentation S produced by Algorithm 1 is not too fine according to Definition 1, using the region comparison predicate D defined in (4.11).*

Proof. By definition, in order for S to be too fine there is some pair of components for which D does not hold. There must be at least one edge between such a pair of components that was considered in Step 4 and did not cause a merge. Let $o_q = (v_i, v_j)$ be the first such edge in the ordering. In this case the algorithm decided not to merge C_i^{q-1} and C_j^{q-1} which implies $w(o_q) > MInt(C_i^{q-1}, C_j^{q-1})$. By Lemma 1 we know that either $C_i = C_i^{q-1}$ or $C_j = C_j^{q-1}$. Either way we see that $w(o_q) > MInt(C_i, C_j)$ implying D holds for C_i and C_j, which is a contradiction. □

Theorem 2. *The segmentation S produced by Algorithm 1 is not too coarse according to Definition 2, using the region comparison predicate D defined in (4.11).*

Proof. In order for S to be too coarse there must be some proper refinement, T, that is not too fine. Consider the minimum weight edge e that is internal to a component $C \in S$ but connects distinct components $A, B \in T$. Note that by the definition of refinement $A \subset C$ and $B \subset C$.

Since T is not too fine, either $w(e) > Int(A) + \tau(A)$ or $w(e) > Int(B) + \tau(B)$. Without loss of generality, say the former is true. By construction any edge connecting A to another sub-component of C has weight at least as large as $w(e)$, which is in turn larger than the maximum weight edge in $MST(A, E)$ because $w(e) > Int(A)$. Thus the algorithm, which considers edges in non-decreasing weight order, must consider all the edges in $MST(A, E)$ before considering any edge from A to other parts of C. So the algorithm must have formed A before forming C, and in forming C it must have merged A with some other sub-component of C. The weight of the edge that caused this merge must be least as large as $w(e)$. However, the algorithm would not have merged A in this case because $w(e) > Int(A) + \tau(A)$, which is a contradiction. □

Theorem 3. *The segmentation S produced by Algorithm 1 does not depend on which non-decreasing weight order of the edges is used.*

Proof. Any ordering can be changed into another one by only swapping adjacent elements. Thus it is sufficient to show that swapping the order of two adjacent edges of the same weight in the non-decreasing weight ordering does not change the result produced by Algorithm 1.

Let e_1 and e_2 be two edges of the same weight that are adjacent in some non- decreasing weight ordering. Clearly if when the algorithm considers the first of these two edges they connect disjoint pairs of components or exactly the same pair of components, then the order in which the two are considered does not matter. The only case we need to check is when e_1 is between two components A and B and e_2 is between one of these components, say B, and some other component C.

Now we show that e_1 causes a merge when considered after e_2 exactly when it would cause a merge if considered before e_2. First, suppose that e_1 causes a merge when considered before e_2. This implies $w(e_1)??MInt(A, B)$. If e_2 were instead considered before e_1, either e_2 would not cause a merge and trivially e_1 would still cause a merge, or e_2 would cause a merge in which case the new component $B \cup C$ would have $Int(B \cup C) = w(e_2) = w(e_1)$. So we know $w(e_1) \leq MInt(A, B \cup C)$ which implies e_1 will still cause a merge. On the other hand, suppose that e_1 does not cause a merge when considered before e_2. This implies $w(e1) > MInt(A, B)$. Then either $w(e_1) > Int(A) + \tau(A)$, in which case this would still be true if e_2 were considered first (because e_2 does not touch A), or $w(e_1) > Int(B) + \tau(B)$. In this second case, if e_2 were considered first it could not cause a merge since $w(e_2) = w(e_1)$ and so $w(e_2) > MInt(B, C)$. Thus when considering e_1 after e_2 we still have $w(e_1) > MInt(A, B)$ and e_1 does not cause a merge. □

BIBLIOGRAPHY

Akselrod-Ballin, A., Galun, M., Gomori, J. M., Filippi, M., Valsasina, P., Basri, R., and Brandt, A. (2009). Automatic segmentation and classification of multiple sclerosis in multichannel MRI. *Biomedical Engineering, IEEE Transactions on*, 56(10):2461–2469.

Al Chekakie, M. O., Welles, C. C., Metoyer, R., Ibrahim, A., Shapira, A. R., Cytron, J., Santucci, P., Wilber, D. J., and Akar, J. G. (2010). Pericardial fat is independently associated with human atrial fibrillation. *Journal of the American College of Cardiology*, 56(10):784–788.

Alexopoulos, N., McLean, D. S., Janik, M., Arepalli, C. D., Stillman, A. E., and Raggi, P. (2010). Epicardial adipose tissue and coronary artery plaque characteristics. *Atherosclerosis*, 210(1):150–154.

Aljabar, P., Heckemann, R. A., Hammers, A., Hajnal, J. V., and Rueckert, D. (2009). Multi-atlas based segmentation of brain images: Atlas selection and its effect on accuracy. *Neuroimage*, 46(3):726–738.

Andronache, A., von Siebenthal, M., Székely, G., and Cattin, P. (2008). Non-rigid registration of multi-modal images using both mutual information and cross-correlation. *Medical image analysis*, 12(1):3–15.

Arad, Y., Spadaro, L. A., Goodman, K., Newstein, D., and Guerci, A. D. (2000). Prediction of coronary events with electron beam computed tomography. *Journal of the American College of Cardiology*, 36(4):1253–1260.

Artaechevarria, X., Munoz-Barrutia, A., and Ortiz-de Solórzano, C. (2009). Combination strategies in multi-atlas image segmentation: Application to brain MR data. *Medical Imaging, IEEE Transactions on*, 28(8):1266–1277.

Ashburner, J., Friston, K. J., et al. (1999). Nonlinear spatial normalization using basis functions. *Human brain mapping*, 7(4):254–266.

Awate, S. P., Tasdizen, T., Foster, N., and Whitaker, R. T. (2006). Adaptive markov modeling for mutual-information-based, unsupervised MRI brain-tissue classification. *Medical Image Analysis*, 10(5):726–739.

Bajcsy, R., Lieberson, R., and Reivich, M. (1983). A computerized system for the elastic matching of deformed radiographic images to idealized atlas images. *Journal of computer assisted tomography*, 7(4):618–625.

Barger, A. V., Block, W. F., Toropov, Y., Grist, T. M., and Mistretta, C. A. (2002). Time-resolved contrast-enhanced imaging with isotropic resolution and broad coverage using an undersampled 3D projection trajectory. *Magnetic resonance in medicine*, 48(2):297–305.

Bazin, P.-L. and Pham, D. L. (2008). Homeomorphic brain image segmentation with topological and statistical atlases. *Medical Image Analysis*, 12(5):616–625.

Bhatia, K. K., Hajnal, J. V., Puri, B. K., Edwards, A. D., and Rueckert, D. (2004). Consistent groupwise non-rigid registration for atlas construction. In *Biomedical Imaging: Nano to Macro, 2004. IEEE International Symposium on*, pages 908–911. IEEE.

Boykov, Y. and Jolly, M.-P. (2000). Interactive organ segmentation using graph cuts. In *Medical Image Computing and Computer-Assisted Intervention–MICCAI 2000*, pages 276–286. Springer.

Boykov, Y. Y. and Jolly, M.-P. (2001). Interactive graph cuts for optimal boundary & region segmentation of objects in nd images. In *Computer Vision, 2001. ICCV 2001. Proceedings. Eighth IEEE International Conference on*, volume 1, pages 105–112. IEEE.

Bricq, S., Collet, C., and Armspach, J. (2008a). Ms lesion segmentation based on hidden markov chains. *Grand Challenge Work.: Mult. Scler. Lesion Segm. Challenge*, pages 1–9.

Bricq, S., Collet, C., and Armspach, J.-P. (2008b). Unifying framework for multimodal brain MRI segmentation based on hidden markov chains. *Medical image analysis*, 12(6):639–652.

Brunner, G., Chittajallu, D. R., Kurkure, U., and Kakadiaris, I. A. (2010). Toward the automatic detection of coronary artery calcification in non-contrast computed tomography data. *The international journal of cardiovascular imaging*, 26(7):829–838.

Budoff, M. J., Achenbach, S., Blumenthal, R. S., Carr, J. J., Goldin, J. G., Greenland, P., Guerci, A. D., Lima, J. A., Rader, D. J., Rubin, G. D., et al. (2006). Assessment of coronary artery disease by cardiac computed tomography a scientific statement from the american heart association committee on cardiovascular imaging and intervention, council on cardiovascular radiology and intervention, and committee on cardiac imaging, council on clinical cardiology. *Circulation*, 114(16):1761–1791.

Callister, T. Q., Cooil, B., Raya, S. P., Lippolis, N. J., Russo, D. J., and Raggi, P. (1998). Coronary artery disease: Improved reproducibility of calcium scoring with an electron-beam CT volumetric method. *Radiology*, 208(3):807–814.

Caselles, V., Kimmel, R., and Sapiro, G. (1997). Geodesic active contours. *International journal of computer vision*, 22(1):61–79.

Chan, T. and Vese, L. (1999). An active contour model without edges. In *Scale-Space Theories in Computer Vision*, pages 141–151. Springer.

Cheng, V. Y., Dey, D., Tamarappoo, B., Nakazato, R., Gransar, H., Miranda-Peats, R., Ramesh, A., Wong, N. D., Shaw, L. J., Slomka, P. J., et al. (2010). Pericardial fat

burden on ecg-gated noncontrast CT in asymptomatic patients who subsequently experience adverse cardiovascular events. *JACC: Cardiovascular Imaging*, 3(4):352–360.

Ciofolo, C. and Barillot, C. (2009). Atlas-based segmentation of 3D cerebral structures with competitive level sets and fuzzy control. *Medical Image Analysis*, 13(3):456–470.

Cipolla, R. and Blake, A. (1990). The dynamic analysis of apparent contours. In *Computer Vision, 1990. Proceedings, Third International Conference on*, pages 616–623. IEEE.

Cocosco, C. A., Zijdenbos, A. P., and Evans, A. C. (2003). A fully automatic and robust brain MRI tissue classification method. *Medical image analysis*, 7(4):513–527.

Cohen, L. D. (1991). On active contour models and balloons. *CVGIP: Image understanding*, 53(2):211–218.

Commowick, O. and Malandain, G. (2006). Evaluation of atlas construction strategies in the context of radiotherapy planning. In *Proceedings of the SA2PM Workshop (From Statistical Atlases to Personalized Models), Copenhagen*.

Coppini, G., Favilla, R., Marraccini, P., Moroni, D., and Pieri, G. (2010). Quantification of epicardial fat by cardiac CT imaging. *The Open Medical Informatics Journal*, 4:126.

Curwen, R. and Blake, A. (1993). Dynamic contours: Real-time active splines. In *Active Vision*, pages 39–57. MIT Press.

de Boer, R., Vrooman, H. A., van der Lijn, F., Vernooij, M. W., Ikram, M. A., van der Lugt, A., Breteler, M. M., and Niessen, W. J. (2009). White matter lesion extension to automatic brain tissue segmentation on MRI. *Neuroimage*, 45(4):1151–1161.

Delille, J., Hernigou, A., Sene, V., Chatellier, G., Boudeville, J., Challande, P., and Plainfosse, M. (1999). Maximal thickness of the normal human pericardium assessed by electron-beam computed tomography. *European radiology*, 9(6):1183–1189.

Dey, D., Nakazato, R., Slomka, P. J., and Berman, D. S. (2012). CT quantification of epicardial fat: Implications for cardiovascular risk assessment. *Current Cardiovascular Imaging Reports*, 5(5):352–359.

Dey, D., Ramesh, A., Slomka, P. J., Nakazato, R., Cheng, V. Y., Germano, G., and Berman, D. S. (2010a). Automated algorithm for atlas-based segmentation of the heart and pericardium from non-contrast CT. In *SPIE Medical Imaging*, pages 762337–762337. International Society for Optics and Photonics.

Dey, D., Schepis, T., Marwan, M., Slomka, P. J., Berman, D. S., and Achenbach, S. (2010b). Automated three-dimensional quantification of noncalcified coronary plaque from coronary CT angiography: Comparison with intravascular us 1. *Radiology*, 257(2):516–522.

Dey, D., Suzuki, Y., Suzuki, S., Ohba, M., Slomka, P. J., Polk, D., Shaw, L. J., and Berman, D. S. (2008). Automated quantitation of pericardiac fat from non-contrast CT. *Investigative radiology*, 43(2):145–153.

Dey, D., Wong, N. D., Tamarappoo, B., Nakazato, R., Gransar, H., Cheng, V. Y., Ramesh, A., Kakadiaris, I., Germano, G., Slomka, P. J., et al. (2010c). Computer-aided non-contrast CT-based quantification of pericardial and thoracic fat and their associations with coronary calcium and metabolic syndrome. *Atherosclerosis*, 209(1):136–141.

Ding, J., Kritchevsky, S. B., Harris, T. B., Burke, G. L., Detrano, R. C., Szklo, M., and Carr, J. J. (2008). The association of pericardial fat with calcified coronary plaque. *Obesity*, 16(8):1914–1919.

Ding, X., Pang, J., Ren, Z., Diaz-Zamudio, M., Berman, D. S., Li, D., Terzopoulos, D., Slomka, P. J., and Dey, D. (2015a). Automated pericardial fat quantification from coronary magnetic resonance angiography. In *Medical Image Understanding and Analysis*, pages 80–85. MIUA.

Ding, X., Slomka, P. J., Diaz-Zamudio, M., Germano, G., Berman, D. S., Terzopoulos, D., and Dey, D. (2015b). Automated coronary artery calcium scoring from non-contrast CT using a patient-specific algorithm. In *SPIE Medical Imaging*, pages 94132U–94132U. International Society for Optics and Photonics.

Ding, X., Terzopoulos, D., Diaz-Zamudio, M., Berman, D. S., Slomka, P. J., and Dey, D. (2014). Automated epicardial fat volume quantification from non-contrast CT. In *SPIE Medical Imaging*, pages 90340I–90340I. International Society for Optics and Photonics.

Ding, X., Terzopoulos, D., Diaz-Zamudio, M., Berman, D. S., Slomka, P. J., and Dey, D. (2015c). Automated pericardium delineation and epicardial fat volume quantification from noncontrast CT. *Medical Physics*, 42(9):5015–5026.

Felzenszwalb, P. F. and Huttenlocher, D. P. (2004). Efficient graph-based image segmentation. *International Journal of Computer Vision*, 59(2):167–181.

Figueiredo, B., Barbosa, J. G., Bettencourt, N., and Tavares, J. M. R. (2009). Semi-automatic quantification of the epicardial fat in CT images. In *VipIMAGE 2009-II ECCOMAS Thematic Conference on Computational Vision and Medical Image Processing*.

Fischl, B., Salat, D. H., Busa, E., Albert, M., Dieterich, M., Haselgrove, C., Van Der Kouwe, A., Killiany, R., Kennedy, D., Klaveness, S., et al. (2002). Whole brain segmentation: Automated labeling of neuroanatomical structures in the human brain. *Neuron*, 33(3):341–355.

Fox, C. S., Massaro, J. M., Hoffmann, U., Pou, K. M., Maurovich-Horvat, P., Liu, C.-Y., Vasan, R. S., Murabito, J. M., Meigs, J. B., Cupples, L. A., et al. (2007). Abdominal visceral and subcutaneous adipose tissue compartments association with metabolic risk factors in the framingham heart study. *Circulation*, 116(1):39–48.

Gee, J. C., Reivich, M., and Bajcsy, R. (1993). Elastically deforming 3D atlas to match anatomical brain images. *Journal of computer assisted tomography*, 17(2):225–236.

Glover, G. and Schneider, E. (1991). Three-point dixon technique for true water/fat decomposition with b0 inhomogeneity correction. *Magnetic resonance in medicine*, 18(2):371–383.

Gorter, P. M., de Vos, A. M., van der Graaf, Y., Stella, P. R., Doevendans, P. A., Meijs, M. F., Prokop, M., and Visseren, F. L. (2008). Relation of epicardial and pericoronary fat to coronary atherosclerosis and coronary artery calcium in patients undergoing coronary angiography. *The American journal of cardiology*, 102(4):380–385.

Grau, V., Mewes, A., Alcaniz, M., Kikinis, R., and Warfield, S. K. (2004). Improved watershed transform for medical image segmentation using prior information. *Medical Imaging, IEEE Transactions on*, 23(4):447–458.

Greif, M., Becker, A., von Ziegler, F., Lebherz, C., Lehrke, M., Broedl, U. C., Tittus, J., Parhofer, K., Becker, C., Reiser, M., et al. (2009). Pericardial adipose tissue determined by dual source CT is a risk factor for coronary atherosclerosis. *Arteriosclerosis, thrombosis, and vascular biology*, 29(5):781–786.

Guimond, A., Meunier, J., and Thirion, J.-P. (2000). Average brain models: A convergence study. *Computer vision and image understanding*, 77(2):192–210.

Han, X. and Fischl, B. (2007). Atlas renormalization for improved brain MR image segmentation across scanner platforms. *Medical Imaging, IEEE Transactions on*, 26(4):479–486.

Hargreaves, B. A., Vasanawala, S. S., Nayak, K. S., Hu, B. S., and Nishimura, D. G. (2003). Fat-suppressed steady-state free precession imaging using phase detection. *Magnetic Resonance in Medicine*, 50(1):210–213.

Heckemann, R. A., Hajnal, J. V., Aljabar, P., Rueckert, D., and Hammers, A. (2006). Automatic anatomical brain MRI segmentation combining label propagation and decision fusion. *NeuroImage*, 33(1):115–126.

Hellier, P. and Barillot, C. (2004). A hierarchical parametric algorithm for deformable multimodal image registration. *Computer Methods and Programs in Biomedicine*, 75(2):107–115.

Hill, D. L., Batchelor, P. G., Holden, M., and Hawkes, D. J. (2001). Medical image registration. *Physics in medicine and biology*, 46(3):R1.

Hirata, Y., Tabata, M., Kurobe, H., Motoki, T., Akaike, M., Nishio, C., Higashida, M., Mikasa, H., Nakaya, Y., Takanashi, S., et al. (2011). Coronary atherosclerosis is associated with macrophage polarization in epicardial adipose tissue. *Journal of the American College of Cardiology*, 58(3):248–255.

Hong, C., Bae, K. T., and Pilgram, T. K. (2003). Coronary artery calcium: Accuracy and reproducibility of measurements with multi–detector row CT-assessment of effects of different thresholds and quantification methods 1. *Radiology*, 227(3):795–801.

Horn, B. K. and Schunck, B. G. (1981). Determining optical flow. In *1981 Technical symposium east*, pages 319–331. International Society for Optics and Photonics.

Huttenlocher, D. P., Klanderman, G., Rucklidge, W. J., et al. (1993). Comparing images using the hausdorff distance. *Pattern Analysis and Machine Intelligence, IEEE Transactions on*, 15(9):850–863.

Isgum, I., Prokop, M., Niemeijer, M., Viergever, M. A., and van Ginneken, B. (2012). Automatic coronary calcium scoring in low-dose chest computed tomography. *Medical Imaging, IEEE Transactions on*, 31(12):2322–2334.

Isgum, I., Rutten, A., Prokop, M., and van Ginneken, B. (2007). Detection of coronary calcifications from computed tomography scans for automated risk assessment of coronary artery disease. *Medical physics*, 34(4):1450–1461.

Isgum, I., Staring, M., Rutten, A., Prokop, M., Viergever, M. A., and van Ginneken, B. (2009). Multi-atlas-based segmentation with local decision fusion-application to cardiac and aortic segmentation in CT scans. *Medical Imaging, IEEE Transactions on*, 28(7):1000–1010.

Jacobs, J. E. (2010). Computed tomographic evaluation of the normal cardiac anatomy. *Radiologic Clinics of North America*, 48(4):701–710.

Janik, M., Hartlage, G., Alexopoulos, N., Mirzoyev, Z., McLean, D. S., Arepalli, C. D., Stillman, A. E., and Raggi, P. (2010). Epicardial adipose tissue volume and coronary artery calcium to predict myocardial ischemia on positron emission tomography-computed tomography studies. *Journal of nuclear cardiology*, 17(5):841–847.

Jermyn, I. H. and Ishikawa, H. (2001). Globally optimal regions and boundaries as minimum ratio weight cycles. *IEEE Transactions on Pattern Analysis and Machine Intelligence*, 23(10):1075–1088.

Joshi, S., Davis, B., Jomier, M., and Gerig, G. (2004). Unbiased diffeomorphic atlas construction for computational anatomy. *NeuroImage*, 23:S151–S160.

Kamber, M., Shinghal, R., Collins, D. L., Francis, G. S., and Evans, A. C. (1995). Model-based 3-d segmentation of multiple sclerosis lesions in magnetic resonance brain images. *Medical Imaging, IEEE Transactions on*, 14(3):442–453.

Kass, M., Witkin, A., and Terzopoulos, D. (1988). Snakes: Active contour models. *International journal of computer vision*, 1(4):321–331.

Kichenassamy, S., Kumar, A., Olver, P., Tannenbaum, A., and Yezzi, A. (1995). Gradient flows and geometric active contour models. In *Computer Vision, 1995. Proceedings., Fifth International Conference on*, pages 810–815. IEEE.

Kirişli, H., Schaap, M., Klein, S., Papadopoulou, S., Bonardi, M., Chen, C., Weustink, A., Mollet, N., Vonken, E., van der Geest, R., et al. (2010). Evaluation of a multi-atlas based method for segmentation of cardiac CTA data: A large-scale, multicenter, and multivendor study. *Medical physics*, 37:6279.

Klein, A., Mensh, B., Ghosh, S., Tourville, J., and Hirsch, J. (2005). Mindboggle: Automated brain labeling with multiple atlases. *BMC medical imaging*, 5(1):7.

Konishi, M., Sugiyama, S., Sugamura, K., Nozaki, T., Ohba, K., Matsubara, J., Matsuzawa, Y., Sumida, H., Nagayoshi, Y., Nakaura, T., et al. (2010). Association of pericardial fat accumulation rather than abdominal obesity with coronary atherosclerotic plaque formation in patients with suspected coronary artery disease. *Atherosclerosis*, 209(2):573–578.

Kroon, D.-J., Oort, v. E., and Slump, C. (2008). Multiple sclerosis detection in multi-spectral magnetic resonance images with principal components analysis.

Kurkure, U., Chittajallu, D. R., Brunner, G., Le, Y. H., and Kakadiaris, I. A. (2010). A supervised classification-based method for coronary calcium detection in non-contrast CT. *The international journal of cardiovascular imaging*, 26(7):817–828.

Kvist, H., Chowdhury, B., Grangård, U., Tylen, U., and Sjöström, L. (1988). Total and visceral adipose-tissue volumes derived from measurements with computed tomography in adult men and women: Predictive equations. *The American journal of clinical nutrition*, 48(6):1351–1361.

Lester, H. and Arridge, S. R. (1999). A survey of hierarchical non-linear medical image registration. *Pattern recognition*, 32(1):129–149.

Lipson, P., Yuille, A. L., O'Keeffe, D., Cavanaugh, J., Taaffe, J., and Rosenthal, D. (1990). Deformable templates for feature extraction from medical images. In *Computer Vision-ECCV 90*, pages 413–417. Springer.

Lorenzen, P., Davis, B. C., and Joshi, S. (2005). Unbiased atlas formation via large deformations metric mapping. In *Medical Image Computing and Computer-Assisted Intervention–MICCAI 2005*, pages 411–418. Springer.

Lötjönen, J. M., Wolz, R., Koikkalainen, J. R., Thurfjell, L., Waldemar, G., Soininen, H., Rueckert, D., Initiative, A. D. N., et al. (2010). Fast and robust multi-atlas segmentation of brain magnetic resonance images. *Neuroimage*, 49(3):2352–2365.

Mahabadi, A. A., Berg, M. H., Lehmann, N., Kälsch, H., Bauer, M., Kara, K., Dragano, N., Moebus, S., Jöckel, K.-H., Erbel, R., et al. (2013). Association of epicardial fat with cardiovascular risk factors and incident myocardial infarction in the general populationthe heinz nixdorf recall study. *Journal of the American College of Cardiology*, 61(13):1388–1395.

Mahabadi, A. A., Massaro, J. M., Rosito, G. A., Levy, D., Murabito, J. M., Wolf, P. A., O'Donnell, C. J., Fox, C. S., and Hoffmann, U. (2009). Association of pericardial fat, intrathoracic fat, and visceral abdominal fat with cardiovascular disease burden: The framingham heart study. *European heart journal*, 30(7):850–856.

Maintz, J. A. and Viergever, M. A. (1998). A survey of medical image registration. *Medical image analysis*, 2(1):1–36.

Malladi, R., Sethian, J., Vemuri, B. C., et al. (1995). Shape modeling with front propagation: A level set approach. *Pattern Analysis and Machine Intelligence, IEEE Transactions on*, 17(2):158–175.

Marroquín, J. L., Vemuri, B. C., Botello, S., Calderón, F., and Fernandez-Bouzas, A. (2002). An accurate and efficient bayesian method for automatic segmentation of brain MRI. *Medical Imaging, IEEE Transactions on*, 21(8):934–945.

McInerney, T. and Terzopoulos, D. (1995). Topologically adaptable snakes. In *Computer Vision, 1995. Proceedings., Fifth International Conference on*, pages 840–845. IEEE.

Morin, R. L., Gerber, T. C., and McCollough, C. H. (2003). Radiation dose in computed tomography of the heart. *Circulation*, 107(6):917–922.

Nakazato, R., Shmilovich, H., Tamarappoo, B. K., Cheng, V. Y., Slomka, P. J., Berman, D. S., and Dey, D. (2011). Interscan reproducibility of computer-aided epicardial and thoracic fat measurement from noncontrast cardiac CT. *Journal of cardiovascular computed tomography*, 5(3):172–179.

Noblet, V., Heinrich, C., Heitz, F., and Armspach, J.-P. (2005). 3-d deformable image registration: A topology preservation scheme based on hierarchical deformation models and interval analysis optimization. *Image Processing, IEEE Transactions on*, 14(5):553–566.

Pang, J., Sharif, B., Arsanjani, R., Bi, X., Fan, Z., Yang, Q., Li, K., Berman, D. S., and Li, D. (2015). Accelerated whole-heart coronary MRA using motion-corrected sensitivity encoding with three-dimensional projection reconstruction. *Magnetic Resonance in Medicine*, 73(1):284–291.

Paragios, N. and Deriche, R. (1999). Geodesic active regions for supervised texture segmentation. In *Computer Vision, 1999. The Proceedings of the Seventh IEEE International Conference on*, volume 2, pages 926–932. IEEE.

Park, H., Bland, P., Hero, A., and Meyer, C. (2005). Least biased target selection in

probabilistic atlas construction. *Medical Image Computing and Computer-Assisted Intervention–MICCAI 2005*, pages 419–426.

Pentland, A. P. (1990). Automatic extraction of deformable part models. *International Journal of Computer Vision*, 4(2):107–126.

Pluim, J. P., Maintz, J. A., Viergever, M., et al. (2003). Mutual-information-based registration of medical images: A survey. *Medical Imaging, IEEE Transactions on*, 22(8):986–1004.

Polonsky, T. S., McClelland, R. L., Jorgensen, N. W., Bild, D. E., Burke, G. L., Guerci, A. D., and Greenland, P. (2010). Coronary artery calcium score and risk classification for coronary heart disease prediction. *JAMA: The Journal of the American Medical Association*, 303(16):1610–1616.

Postelnicu, G., Zöllei, L., and Fischl, B. (2009). Combined volumetric and surface registration. *Medical Imaging, IEEE Transactions on*, 28(4):508–522.

Prastawa, M., Bullitt, E., Ho, S., and Gerig, G. (2004). A brain tumor segmentation framework based on outlier detection. *Medical image analysis*, 8(3):275–283.

Prastawa, M. and Gerig, G. (2008). Automatic ms lesion segmentation by outlier detection and information theoretic region partitioning. *Grand Challenge Work.: Mult. Scler. Lesion Segm. Challenge*, pages 1–8.

Rajani, R., Shmilovich, H., Nakazato, R., Nakanishi, R., Otaki, Y., Cheng, V. Y., Hayes, S. W., Thomson, L. E., Friedman, J. D., Slomka, P. J., et al. (2013). Relationship of epicardial fat volume to coronary plaque, severe coronary stenosis, and high-risk coronary plaque features assessed by coronary CT angiography. *Journal of cardiovascular computed tomography*, 7(2):125–132.

Reeder, S. B., Pineda, A. R., Wen, Z., Shimakawa, A., Yu, H., Brittain, J. H., Gold,

G. E., Beaulieu, C. H., and Pelc, N. J. (2005). Iterative decomposition of water and fat with echo asymmetry and least-squares estimation (ideal): Application with fast spin-echo imaging. *Magnetic resonance in medicine*, 54(3):636–644.

Rueckert, D., Sonoda, L. I., Hayes, C., Hill, D. L., Leach, M. O., and Hawkes, D. J. (1999). Nonrigid registration using free-form deformations: Application to breast MR images. *Medical Imaging, IEEE Transactions on*, 18(8):712–721.

Russ, J. C. (2010). *The image processing handbook*. CRC press.

Sarin, S., Wenger, C., Marwaha, A., Qureshi, A., Go, B. D., Woomert, C. A., Clark, K., Nassef, L. A., and Shirani, J. (2008). Clinical significance of epicardial fat measured using cardiac multislice computed tomography. *The American journal of cardiology*, 102(6):767–771.

Saur, S. C., Alkadhi, H., Desbiolles, L., Székely, G., and Cattin, P. C. (2008). Automatic detection of calcified coronary plaques in computed tomography data sets. In *Medical Image Computing and Computer-Assisted Intervention–MICCAI 2008*, pages 170–177. Springer.

Shahzad, R., Bos, D., Metz, C., Rossi, A., Kirişli, H., van der Lugt, A., Klein, S., Witteman, J., de Feyter, P., Niessen, W., et al. (2013). Automatic quantification of epicardial fat volume on non-enhanced cardiac CT scans using a multi-atlas segmentation approach. *Medical physics*, 40(9):091910.

Shahzad, R., Schaap, M., van Walsum, T., Klien, S., Weustink, A. C., van Vliet, L. J., and Niessen, W. J. (2010). A patient-specific coronary density estimate. In *Biomedical Imaging: From Nano to Macro, 2010 IEEE International Symposium on*, pages 9–12. IEEE.

Shi, J. and Malik, J. (2000). Normalized cuts and image segmentation. *IEEE Transactions on Pattern Analysis and Machine Intelligence*, 22(8):888–905.

Shiee, N., Bazin, P., and Pham, D. (2008a). Multiple sclerosis lesion segmentation using statistical and topological atlases. *Grand Challenge Work.: Mult. Scler. Lesion Segm. Challenge*, pages 1–10.

Shiee, N., Bazin, P.-L., Cuzzocreo, J. L., Reich, D. S., Calabresi, P. A., and Pham, D. L. (2008b). Topologically constrained segmentation of brain images with multiple sclerosis lesions. In *Proc. MICCAI Workshop on Medical Image Analysis on Multiple Sclerosis (MIAMS)*, pages 71–81.

Shiee, N., Bazin, P.-L., Ozturk, A., Reich, D. S., Calabresi, P. A., and Pham, D. L. (2010). A topology-preserving approach to the segmentation of brain images with multiple sclerosis lesions. *NeuroImage*, 49(2):1524–1535.

Sjostrom, L., Kvist, H., Cederblad, A., and Tylen, U. (1986). Determination of total adipose tissue and body fat in women by computed tomography, 40k, and tritium. *American Journal of Physiology-Endocrinology And Metabolism*, 250(6):E736–E745.

Souplet, J.-C., Lebrun, C., Ayache, N., Malandain, G., et al. (2008). An automatic segmentation of t2-flair multiple sclerosis lesions. In *The MIDAS Journal-MS Lesion Segmentation (MICCAI 2008 Workshop)*.

Staib, L. H. and Duncan, J. S. (1989). Parametrically deformable contour models. In *Computer Vision and Pattern Recognition, 1989. Proceedings CVPR'89., IEEE Computer Society Conference on*, pages 98–103. IEEE.

Taguchi, R., Takasu, J., Itani, Y., Yamamoto, R., Yokoyama, K., Watanabe, S., and Masuda, Y. (2001). Pericardial fat accumulation in men as a risk factor for coronary artery disease. *Atherosclerosis*, 157(1):203–209.

Tamarappoo, B., Dey, D., Shmilovich, H., Nakazato, R., Gransar, H., Cheng, V. Y., Friedman, J. D., Hayes, S. W., Thomson, L. E., Slomka, P. J., et al. (2010). Increased

pericardial fat volume measured from noncontrast CT predicts myocardial ischemia by SPECT. *JACC: Cardiovascular Imaging*, 3(11):1104–1112.

Terzopoulos, D., Witkin, A., and Kass, M. (1988). Symmetry-seeking models and 3D object reconstruction. *International Journal of Computer Vision*, 1(3):211–221.

Thévenaz, P. and Unser, M. (2000). Optimization of mutual information for multiresolution image registration. *Image Processing, IEEE Transactions on*, 9(12):2083–2099.

Thilo, C., Gebregziabher, M., Mayer, F. B., Zwerner, P. L., Costello, P., and Schoepf, U. J. (2010). Correlation of regional distribution and morphological pattern of calcification at CT coronary artery calcium scoring with non-calcified plaque formation and stenosis. *European radiology*, 20(4):855–861.

Thirion, J.-P. (1998). Image matching as a diffusion process: An analogy with maxwell's demons. *Medical image analysis*, 2(3):243–260.

Tomas, X. and Warfield, S. (2009). Fully-automatic generation of training points for automatic multiple sclerosis segmentation. *Work. Med. Image Anal. Mult. Scler*, pages 49–59.

Van der Lijn, F., den Heijer, T., Breteler, M. M., and Niessen, W. J. (2008). Hippocampus segmentation in MR images using atlas registration, voxel classification, and graph cuts. *Neuroimage*, 43(4):708–720.

Van Leemput, K., Maes, F., Vandermeulen, D., Colchester, A., and Suetens, P. (2001). Automated segmentation of multiple sclerosis lesions by model outlier detection. *Medical Imaging, IEEE Transactions on*, 20(8):677–688.

Van Leemput, K., Maes, F., Vandermeulen, D., and Suetens, P. (1999). Automated

model-based tissue classification of MR images of the brain. *Medical Imaging, IEEE Transactions on*, 18(10):897–908.

Vemuri, B., Ye, J., Chen, Y., and Leonard, C. (2000). A level-set based approach to image registration. In *Mathematical Methods in Biomedical Image Analysis, 2000. Proceedings. IEEE Workshop on*, pages 86–93. IEEE.

Vemuri, B. C., Huang, S., Sahni, S., Leonard, C. M., Mohr, C., Gilmore, R., and Fitzsimmons, J. (1998). An efficient motion estimator with application to medical image registration. *Medical Image Analysis*, 2(1):79–98.

Vercauteren, T., Pennec, X., Perchant, A., and Ayache, N. (2009). Diffeomorphic demons: Efficient non-parametric image registration. *NeuroImage*, 45(1):S61–S72.

Vrooman, H. A., Cocosco, C. A., van der Lijn, F., Stokking, R., Ikram, M. A., Vernooij, M. W., Breteler, M. M., and Niessen, W. J. (2007). Multi-spectral brain tissue segmentation using automatically trained k-nearest-neighbor classification. *Neuroimage*, 37(1):71–81.

Walsh, D. O., Gmitro, A. F., and Marcellin, M. W. (2000). Adaptive reconstruction of phased array MR imagery. *Magnetic Resonance in Medicine*, 43(5):682–690.

Weiss, Y. (1999). Segmentation using eigenvectors: A unifying view. In *Proc. International Conference on Computer Vision*, volume 2, pages 975–982. IEEE.

Wheeler, G. L., Shi, R., Beck, S. R., Langefeld, C. D., Lenchik, L., Wagenknecht, L. E., Freedman, B. I., Rich, S. S., Bowden, D. W., Chen, M. Y., et al. (2005). Pericardial and visceral adipose tissues measured volumetrically with computed tomography are highly associated in type 2 diabetic families. *Investigative radiology*, 40(2):97–101.

Wong, C. X., Abed, H. S., Molaee, P., Nelson, A. J., Brooks, A. G., Sharma, G., Leong, D. P., Lau, D. H., Middeldorp, M. E., Roberts-Thomson, K. C., et al. (2011). Peri-

cardial fat is associated with atrial fibrillation severity and ablation outcome. *Journal of the American College of Cardiology*, 57(17):1745–1751.

Wong, S. T. and Roos, M. S. (1994). A strategy for sampling on a sphere applied to 3D selective rf pulse design. *Magnetic Resonance in Medicine*, 32(6):778–784.

Wu, M., Rosano, C., Lopez-Garcia, P., Carter, C. S., and Aizenstein, H. J. (2007). Optimum template selection for atlas-based segmentation. *Neuroimage*, 34(4):1612–1618.

Wu, Z. and Leahy, R. (1993). An optimal graph theoretic approach to data clustering: Theory and its application to image segmentation. *IEEE Transactions on Pattern Analysis and Machine Intelligence*, 15(11):1101–1113.

Xu, C. and Prince, J. L. (1998a). Generalized gradient vector flow external forces for active contours. *Signal processing*, 71(2):131–139.

Xu, C. and Prince, J. L. (1998b). Snakes, shapes, and gradient vector flow. *Image Processing, IEEE Transactions on*, 7(3):359–369.

Yalamanchili, R., Dey, D., Kukure, U., Nakazato, R., Berman, D. S., and Kakadiaris, I. A. (2010). Knowledge-based quantification of pericardial fat in non-contrast CT data. In *SPIE Medical Imaging*, pages 76231X–76231X. International Society for Optics and Photonics.

Yezzi Jr, A., Tsai, A., and Willsky, A. (1999). A statistical approach to snakes for bimodal and trimodal imagery. In *Computer Vision, 1999. The Proceedings of the Seventh IEEE International Conference on*, volume 2, pages 898–903. IEEE.

Yoshizumi, T., Nakamura, T., Yamane, M., Waliul Islam, A. H. M., Menju, M., Yamasaki, K., Arai, T., Kotani, K., Funahashi, T., Yamashita, S., et al. (1999). Abdom-

inal fat: Standardized technique for measurement at CT 1. *Radiology*, 211(1):283–286.

Yuille, A. L., Hallinan, P. W., and Cohen, D. S. (1992). Feature extraction from faces using deformable templates. *International journal of computer vision*, 8(2):99–111.

Zhang, L., You, J., Zhang, D., Bhattacharya, P., et al. (2008). Dark line detection with line width extraction. In *Image Processing, 2008. ICIP 2008. 15th IEEE International Conference on*, pages 621–624. IEEE.

Zhu, S. C. and Yuille, A. (1996). Region competition: Unifying snakes, region growing, and bayes/mdl for multiband image segmentation. *Pattern Analysis and Machine Intelligence, IEEE Transactions on*, 18(9):884–900.

Zijdenbos, A. P., Forghani, R., and Evans, A. C. (2002). Automatic" pipeline" analysis of 3-d MRI data for clinical trials: Application to multiple sclerosis. *Medical Imaging, IEEE Transactions on*, 21(10):1280–1291.

Zöllei, L., Learned-Miller, E., Grimson, E., and Wells, W. (2005). Efficient population registration of 3D data. In *Computer Vision for Biomedical Image Applications*, pages 291–301. Springer.